QATAR UNIVERSITY

COLLEGE OF ARTS AND SCIENCES

STUDY OF THE ION INTERCLATION MECHANISM IN MXENE MEMBRANE FOR THE WATER TREATMENT APPLICATIONS

BY
MOHAMED IBRAHIM ELSAYED ALI HUSSEIN HELAL

A Thesis Submitted to

the College of Arts and Sciences

in Partial Fulfillment of the Requirements for the Degree of

Masters of Science in Material Science and Technology

June 2020

COMMITTEE PAGE

The members of the Committee approve the Thesis of
MOHAMED IBRAHIM ELSAYED ALI HUSSEIN HELAL defended on
11/05/2020.

Dr. Ahmed Abdelfattah Elzatahry
Thesis/Dissertation Supervisor

Dr. Khaled Mahmoud
Committee Member

Dr. Essam Heggy
Committee Member

Dr. Talal Al Tahtamouni
Committee Member

Approved:

Ibrahim AlKaabi, Dean, College of Arts and Sciences

ABSTRACT

HELAL MOHAMED IEAH., Masters : June : 2020, Material Science and Technology

Title: Study of The Ion Intercalation Mechanism in MXene Membrane for The Water Treatment Apllications.

Supervisor of Thesis: Ahmed A. Elzatahry.

Co-Supervisor of Thesis: Khaled Mahmoud.

MXene membrane consists of free-standing layers of a 2D material, namely MXene, which is attracting growing interest due to its conductivity and well-defined interlayer distance and slit-like channels, making it attractive in applications like energy storage and water treatment applications. Unfortunately, these membranes can swell and shrink when in contact with water or under high temperatures. MXene (Ti_3C_2) is a two-dimensional early transition metal carbide-derived by the etching of MAX (Ti_3AlC_2) phases in fluoride-containing solutions, and it can be intercalated with cations due to its surface termination that makes MXene sheets negatively charged.

The conventional characterization was used to examine the successful intercalation of cations between MXene membrane layers utilizing SEM, TEM, XPS, and elemental mapping by EDS. The contact angle revealed that higher hydration radius cations decrease the hydrophilicity of the MXene membranes when intercalated.

This thesis is comprised of four chapters. Chapter one consists of the introduction and literature review, which provides an overview of the current conventional technology in water treatment applications and how the two-dimensional nanomaterial can improve it. The high water flow of 2D membrane stems from the well-defined nanometer channels that exhibit low friction for the water flow making high water flux membranes. This chapter also addresses the synthesis, fabrication, and structure of MXene membranes. Furthermore, the chapter discusses the ionic intercalation in aqueous for these membranes and compares the ionic sieving mechanism between GO and MXene membranes as well as discusses the stability of

MXene membranes under different environmental conditions. The second chapter introduces the systems in detail and outlines the materials used in this study. Chapter three presents the results of the investigation by showing the synthesis and fabrication of the membranes and the successful intercalation of cations between MXene layers. Furthermore, the effect of different intercalated cations under various temperatures and relative humidity values are investigated using in-situ ESEM and XRD capabilities. A conclusion of the study is provided in the final chapter.

Here, using *in-situ* X-ray diffraction (XRD) analysis, the effect of intercalated cations such as Na-Ti_3C_2, Ca-Ti_3C_2, and Al-Ti_3C_2 between MXene membranes on its crystal structure (namely d-space) under different temperatures are investigated. The study found that the higher the hydration enthalpies of the intercalated cations, the less stable the MXene membrane becomes under increased high temperatures. The same observation was true in the *in-situ* environmental scanning electron microscope (ESEM) study, where the cross-section of these cations suffers a significant decrease compared with lower hydration enthalpy cations. Moreover, an *in-situ* (ESEM) was utilized to observe the effect of different hydration enthalpy cations on membrane thickness under changes in relative humidity. Higher hydration enthalpy intercalated cation MXene membranes had fewer changes in their cross-section thickness compared with lower hydration enthalpy cations.

This thesis provides a detailed study of the ion intercalation mechanism in MXene membrane for applications related to water treatment.

DEDICATION

I declare that the work presented in this thesis is an original work, and to the best of my knowledge there has been no work that is done similar to what is shown in this thesis.

ACKNOWLEDGMENTS

I want to acknowledge the support I got from my family and friends for being patient and supportive during my master's program duration. I cannot thank them enough. Special thanks go for my parents who have always been there for me.

I would like to thank my supervisor Dr. Ahmed Elzatahry for his continuous support and his guidance through my master thesis.

I would like to express my acknowledgments, gratitude, and give special thanks to my Co-supervisor, Dr. Khaled Mahmoud for his support and guidance through this work and his guidance and support through my faced obstacles. Also, I would like to thank Dr. Ivan Gladich and Dr. Yongfeng Tong for their inputs and support in the simulation and XPS experiments in this work. Moreover, I would like to thank the committee members Dr. Talal Al-tahtamouni and Dr. Essam Heggy for their support.

I would like to thank all my professors (Dr. Khaled Yousuf, Dr. Abubakr Abdullah, and the staff in CAM who have supported me) at material science and technology program and center of advanced materials that provided me with the knowledge and needed skills for my thesis work.

I would like to thank CNAQ for providing help in manufacturing the stub used in this thesis, and QEERI-water center that allowed the project to be part of its objectives. The authors would like to thank core labs for giving access to the equipment to do the experiments.

SYNONYMS

XRD: X-Ray Diffraction

DSC: Differential Scanning Calorimetry.

ESEM: Environmental Scanning Electron Microscopy

EDS: Energy Dispersive Spectroscopy

RT: Room Temperature

TGA: Thermogravimetric Analysis

TEM: Transmission Electron Microscopy

SSAs: High specific Surface Area

VAC: Vacuum Assisted filtration

2D materials: Two Dimensional Materials

HF: Hydrofluoric Acid

PVA: Polyvinyl Alcohol

EB: Electron Beam

SEM: Scanning Electron Microscope

GO: Graphen Oxide

HCl: Hydrohloric Acid

XPS: X-ray photoelectron spectroscopy

TABLE OF CONTENTS

LIST OF TABLES

List of Figures

Chapter 1 : Introduction and literature review

1.1 Separation process of two-dimensional membranes for water treatment application:

Water is becoming an increasingly scarce resource as we progress into the twenty-first century, and producing clean water from polluted sources[1] poses serious challenges, especially considering the deteriorated situation caused by industrialization, climate change, and other human activities [2]. As a result, wastewater treatment has been widely accepted as a sustainable approach to current water demands [3]. Desalination of brackish and seawater is considered the main source for producing clean water, particularly in arid regions where the process can be done by using either thermal or membranes technologies [4].

Adsorption, coagulation, disinfection, media filtration, and membrane filtration are other technologies utilized for water and wastewater treatment[5,6]. Membranes desalination and water treatment are the most favorable technologies worldwide due to their ease of use and lower energy costs as both are clear advantages for the membrane filtration process. Membrane filtration works as filtration through different processes, such as reverse osmosis (RO), microfiltration (MF), ultrafiltration (UF), nanofiltration (NF), and forward osmosis (FO) [7–12], depending on the desired pore size of the membrane[13] or, in other words, the cut-off size of the unwanted particles[14].

Some of these membranes exhibit high salt rejection and water flux. The materials of these membranes may have a significant impact on the properties. For example, polymeric membranes are one of the most favorable materials used in desalination and

wastewater treatment due to their low cost and outstanding long-term use. However, various studies have focused on solving the challenges that come with this material. These challenges include finding the proper balance between permeability and selectivity as well as scaling and fouling, such as introducing nanomaterials to the polymeric membranes using different protocols. Two remarkable state-of-the-art solutions are thin-film nanocomposites (TFNs) and mixed matrix membranes (MMMs).

Although abstruse, nanotechnology is currently used in several commercial applications including water treatment, where it enhances properties of conventional materials and introduces new functionalities. Innovative membrane designs were achieved *via* the advancement of nanotechnology by introducing nanomaterials [5]. These outstanding properties of nanomaterials allowed innovative ways to enhance the performance of the traditional membranes, such as improving hydrophilicity, bactericidal, flux, antifouling, and rejection properties. A plethora of nanomaterials have been used for this purpose including carbon nanotubes, metal oxides, fluorenes, metal organic frameworks, and two-dimensional (2D) nanomaterials, particularly graphene oxide (GO).

2D nanomaterials have dimensions in two axes, while one axis in the nanoscale has immensely improved several applications when used. These applications include, but are not limited to, storage devices [15,16], electronic devices, and water purification membranes[17]. These 2D materials possess higher specific surface areas (SSAs) unlike the bulk materials[18]. An example of these materials can include graphene, graphene oxide (GO), and the newly discovered 2D metal carbides and carbonitrides (MXenes).

The films and membranes composed of 2D nanomaterials can inherint different ions between layers depending on how they are synthesized. This property allows them to

store energy between their layers when used as electrodes in battery applications, for example. Moreover, the ion capturing by 2D membranes makes them attractive for water purification systems where they can be used to capture undesirable ions from natural or wastewater. The intercalation of ions between the 2D membranes can cause a change in the volume of the material or structural specific properties[15,17,19,20].

The versatility of 2D membranes in terms of how ion rejection and water flux could be controlled by adjusting properties like interlayer distance, flake size, and the overall thickness of the membrane, makes them very unique in the membrane filtration technology[21,22]. A known example of such membranes is the graphene oxide (GO) membrane as it has been used in advanced separation membranes providing clean water with cost efficiency[21,23,24]. The high water flow of GO membrane stems from the well-defined nanometer channels that exhibit low friction for water flow resulting in high water flux membranes. Joshi et. al.[25] found that GO membranes are vacuum-tight in a non-wet state, unlike when GO membranes are immersed in water as they sieve solute molecules that have hydrated radii larger than 4.5Å. This behavior is related to the opening up of the network of Nano capillaries of the membrane when hydrated accepting only species that could fit and pass-through[25] (Figure 1-1).

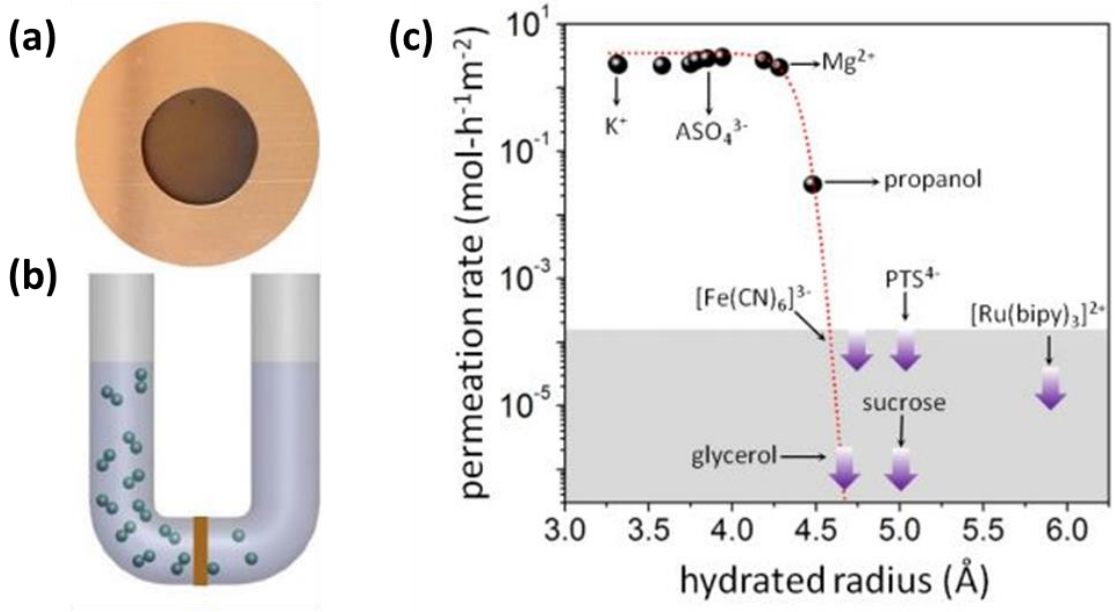

Figure 1-1: (a) GO membrane with 1 cm diameter covering a Cu foil. (b) The schematic of the experimental setup where the solution is passing through GO membrane (yellow) from left to right. (c) shows the permeation rate, where ions with hydration radii of 4.5Å are passing through with higher permeation rate than those with larger hydration radii ref[25].

Pengzhan Sun et. al.[22] explained a similar selective ion-penetration mechanism of GO membrane for sodium, heavy metal, and copper salts where sodium salts permeate quicker than heavy metal salts. Interestingly, organic contaminants and copper salts did not manage to infiltrate GO membranes. A simple drop-casting method was used to prepare the free-standing GO membrane (Figure 1-2.c) from a colloidal GO solution (Figure 1-2.b) where GO membrane showed a smooth surface (Figure 1-2.d). A

homemade plastic sink separated by a plastic plate as in the schematic in Figure1-2.a was used to investigate the effect of the selective ion-penetration properties for different metallic salt solutions. As seen in Figure 1-2.e, the filtration process of heavy metal salts were much slower than sodium salts due to their strong interactions with the GO membranes and the nano capillaries formed within lamellar structure.

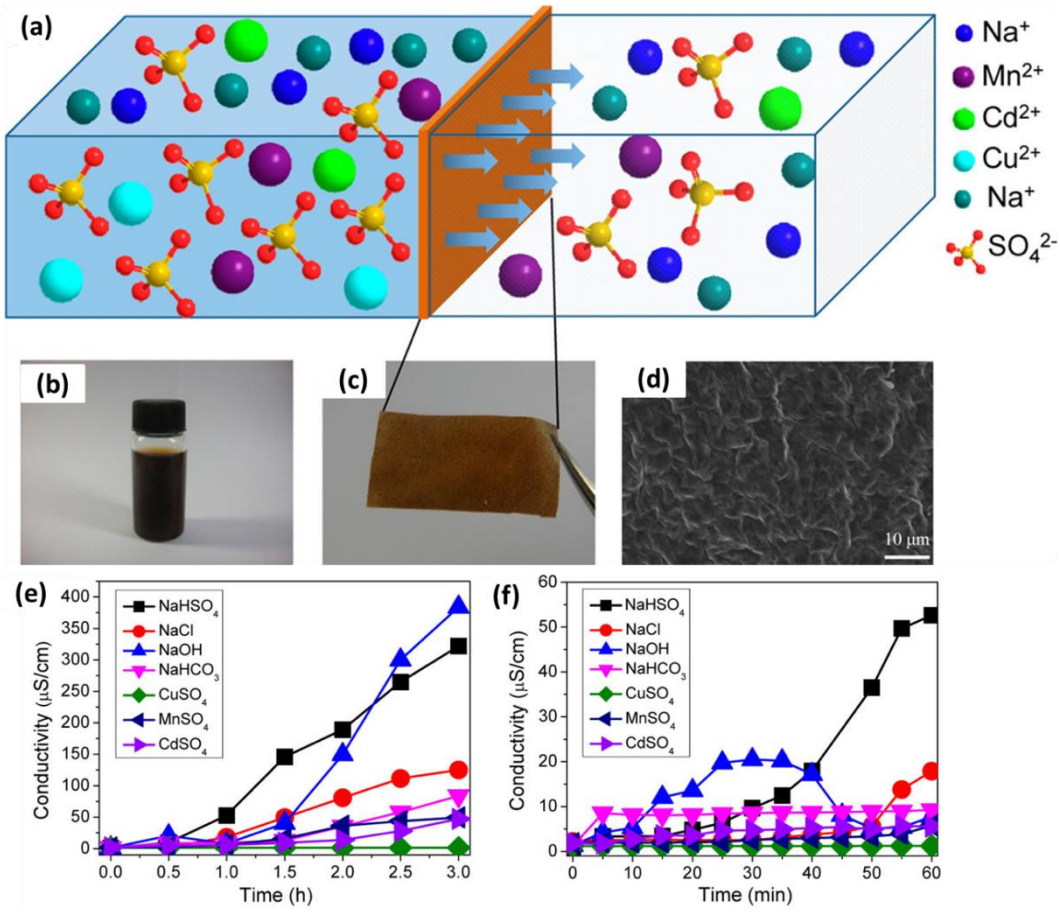

Figure 1-2: (a) Schematic diagram of a homemade plastic sink separated by a plastic plate and the penetration processes of several ions infiltrating GO membrane. (b) GO the colloidal suspension (2 mg/mL) of GO used in preparing the GO membrane. (c)

Photograph of the prepared freestanding GO membrane by drop-casting 2 mg/mL of GO suspension. (d) SEM images of the surface of the GO membrane. (e) the graph shows the effect of penetration processes of different salt solutions over the conductivity with time through GO membranes. (f) enlarged graph from (e) for the first hour ref[22].

Basic salts like $NaHCO_3$ exhibited slower permeation rates due to their reaction with the functional groups of GO membranes and the production of gases. Remarkably, the conductivity of copper salts remained unchanged for the three-hour period, which suggests that copper was blocked entirely by the GO film. Furthermore, in the initial stages of this process (Figure 1-2.f), initial conductivity are the same for all salts except for $NaHSO_4$ aqueous solution and a small peak for NaOH solution as a result of this salt interaction with the functional group of both sides of GO sheets[22].

1.2 Structure and synthesis of MXene:

Two-dimensional material like carbide, carbonitrides, and nitrides (MXenes) are the newest members of the 2D nanomaterials family able to be synthesized from the MAX phase, described as $M_{n+1}AX_n$ where M is an early transition metal, A is an A-group element (Usually Si or Al), X is carbon and/or nitrogen (figure 1-3)[15,26].

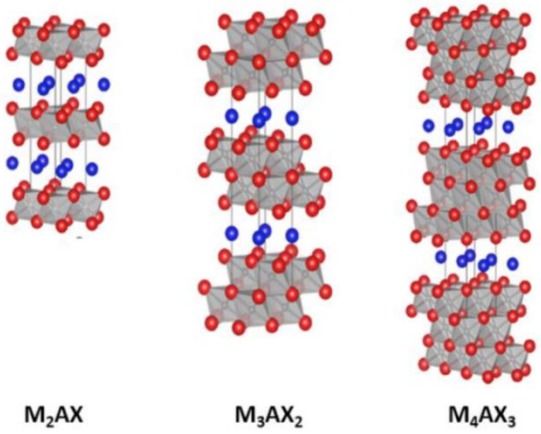

Figure 1-3: This figure illustrates different M_nAX_{n-1} phase structures where n can be 1, 2, and 3. ref[27].

MXene is produced by the removal of A element from the corresponding MAX phase using HF or in-situ HF, where it can selectively remove the A-layer and produce a multi-layered (ML) MXene structure that has several two-dimensional sheets interlinked by hydrogen and/or van der Waals bonding[15]. The MXene formula is $M_{n+1}X_nT_x$ (n = 1, 2, 3) (Figure 1-4), where M is an early transition metal like Sc, Ti, Zr, Hf, V, Nb, Ta, Cr, Mo, and others, X is nitrogen and/or carbon and T_x as the surface terminations, such as OH, O or F ions. This structure makes MXene an attractive material for several applications including water treatment when it is used in membranes.

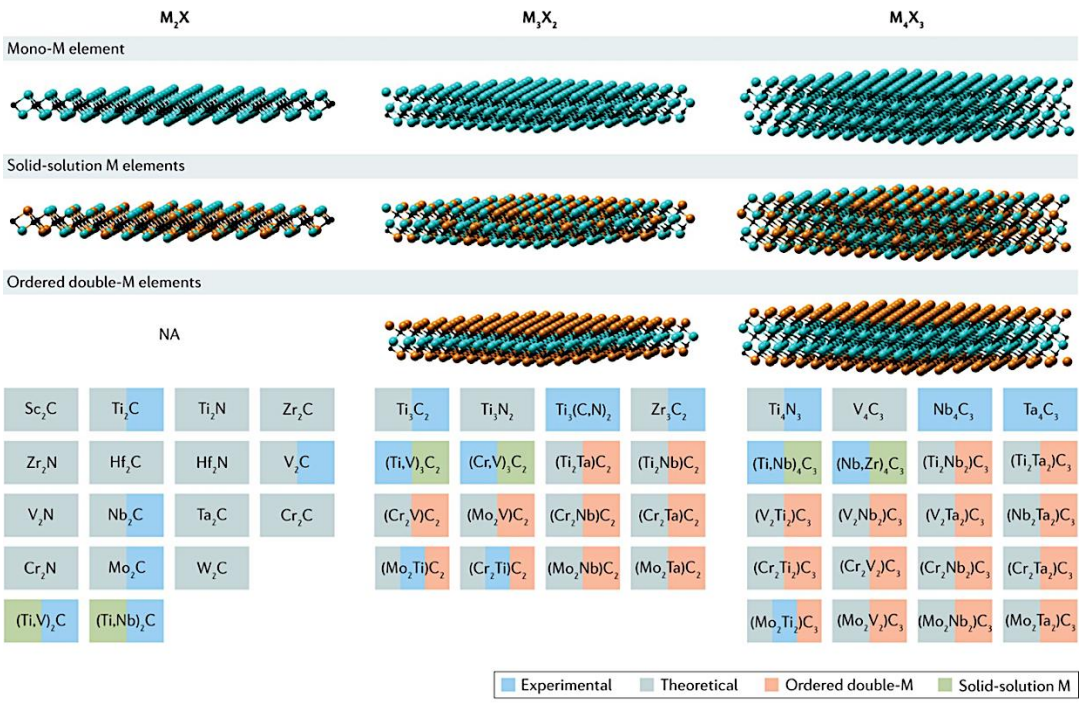

Figure 1-4: MXene schematic structure where MXene can be M_2X, M_3X_2, and M_4X_3 in several forms from Mono-M element, solid-solution M elements, and ordered double-M elements ref [28].

The surface termination of MXene contains oxygen (-O-), hydroxyl (-OH), and fluorine (-F) depending on the etching protocol etchant [26]. Surface termination render MXene sheets negatively charged as measured by zeta potential with values between −30 to −80 mV[29]. Moreover, functionalization of MXene surface can influence its ability to adsorb specific species[30,31]. The ionic intercalation activity of the MXene has been used for the storage capacity application, which means the unique property of ion intercalation in MXene can be utilized as an enhanced ion transport capability. The MXene anode

showed an enhanced capacity and capacity retention due to the high valence intercalated aluminum ions.

The most studied MXene to date is $Ti_3C_2T_x$ produced from the Ti_3AlC_2 MAX phase. Few selected routes have been widely used for the MXene synthesis[26,32]. The most known routes are to selectively etch the A-element atomic layers from the MAX phase by HF (5 to 50 wt.%). In such cases, the solution is washed thoroughly after immersing MAX phase in HF solution for a specific period of time (depending on the concentration of HF used) under constant stirring at room temperature by repeated centrifugation and decantation to remove residual reaction products like salts and acids from the solution and achieve a pH of approximately 6. This process eventually produces a ML-MXene supernatant, which can be produced as a powder by several processes including vacuum assisted filtration or by drying in a vacuum (Figure 1-5).

Another route to produce ML-MXene is *in-situ* HF that results from the chemical reaction of hydrochloric acid (HCL) combined with another fluoride salt like (LiF)[15,33]. This route can produce a different quality and size of MXene flakes dependent on the concentration of HCl and fluoride salt. Alhabeb et. al.[26] found that increasing the molar ration from 5 to 7.5 or more and the concentration of HCl from 6 to 9 M increased the quality and size of MXene. These findings facilitated the study of defects as well as the quantification of such defects. The previous method was called minimally intensive layer delamination (MILD) as it produces single and larger flakes with very few defects. The MILD method was used in this study; more details are mentioned in the synthesis section of MXene flakes.

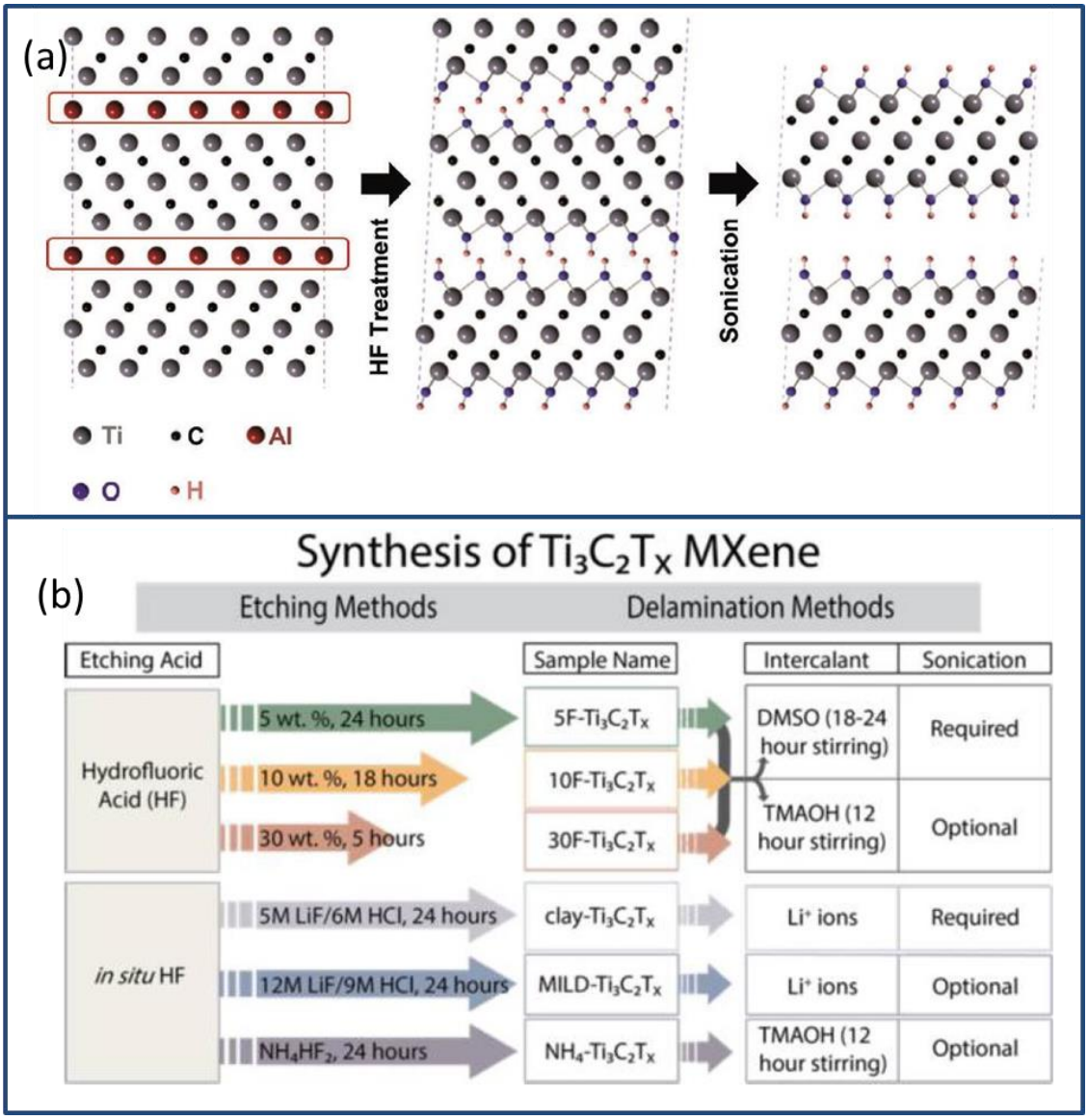

Figure 1-5:(a) schematic of the transformation process from MAX to delaminated MXene (DL-MXene), starting from the removal of Al layers by HF etching producing ML-MXene then sonication to exfoliate the layers by means of intercalation and sonication process, ref[33]. (b) schematics of different methods of DL-Ti3C2Tx preparation methods by either direct or in-situ HF routes, ref[26].

In both etching cases, the weak van der Waals forces holding together the multi-layered MXene (ML-MXene) can be expanded or even broken by the intercalation of water, cations, tetrabutylammonium hydroxide (TBAOH), dimethyl sulfoxide (DMSO), and others between the interlayer spacing of ML-MXene resulting in the expansion of its layers (Figure 1-5.a). In the case of in-situ HF, the intercalated cation from the process allows the acquisition of DL-MXene by a simple bath sonication or probe sonication; however, handling HF is considered to be hazardous, so extra care is required when synthesizing MXene using direct HF [26,28,33,34]. On the other hand, it is very challenging to synthesize $Ti_{n+1}N_nT_x$ MXene from the $Ti_{n+1}AlN_n$ phase by etching Al atomic layer element at room temperature due to its high energy requirements[35]. Figure 1-5.b illustrates the schematic synthesis routes using direct or in-situ HF with different pathways of delamination for ML-MXene at room temperature. The reaction time and concentration of HF in the direct HF process can affect the etching process of Al layers[36–38].

The observed staking arrangement for MXene flakes is different for the two methods. An example of this can be seen in the similar morphology of the produced MXene from MILD process to the Ti_3AlC_2 (MAX) phase (Figure 1-6.a,c). On the other hand, the loosely packed-accordion-like structure for the produced ML-MXene when using the direct HF method (Figure 1-6.b) is very different between MAX and MXene in (Figure 1-6.a,c). Delamination of the produced ML-MXene can be achieved by LiF/HCl process[26] or via intercalation of organic molecules like alkylammonium cations, or DMSO[39,40] followed by sonication or shaking.

(Figure 1-6.d) illustrates a typical X-ray diffraction (XRD) profile of both Ti_3AlC_2 phase and $Ti_3C_2T_x$ MXene. Two characteristic peaks can be observed; one at 2θ of ~39° corresponding to peak (104) that signifies the atomic layers of Al, and the other peak of (002) at ~9.5° representing the interlayer distance etching the Ti_3AlC_2 phase resulting in the suppression of the (104) peak due to the removal of the Al layers, while the (002) peak is shifted to a lower Bragg angle. This shift is caused by the removal of Al layers and replacing them with surface termination, resulting in the increase of the interlayer spacing, which may increase further with the incorporation of cations and water molecules[41,42].

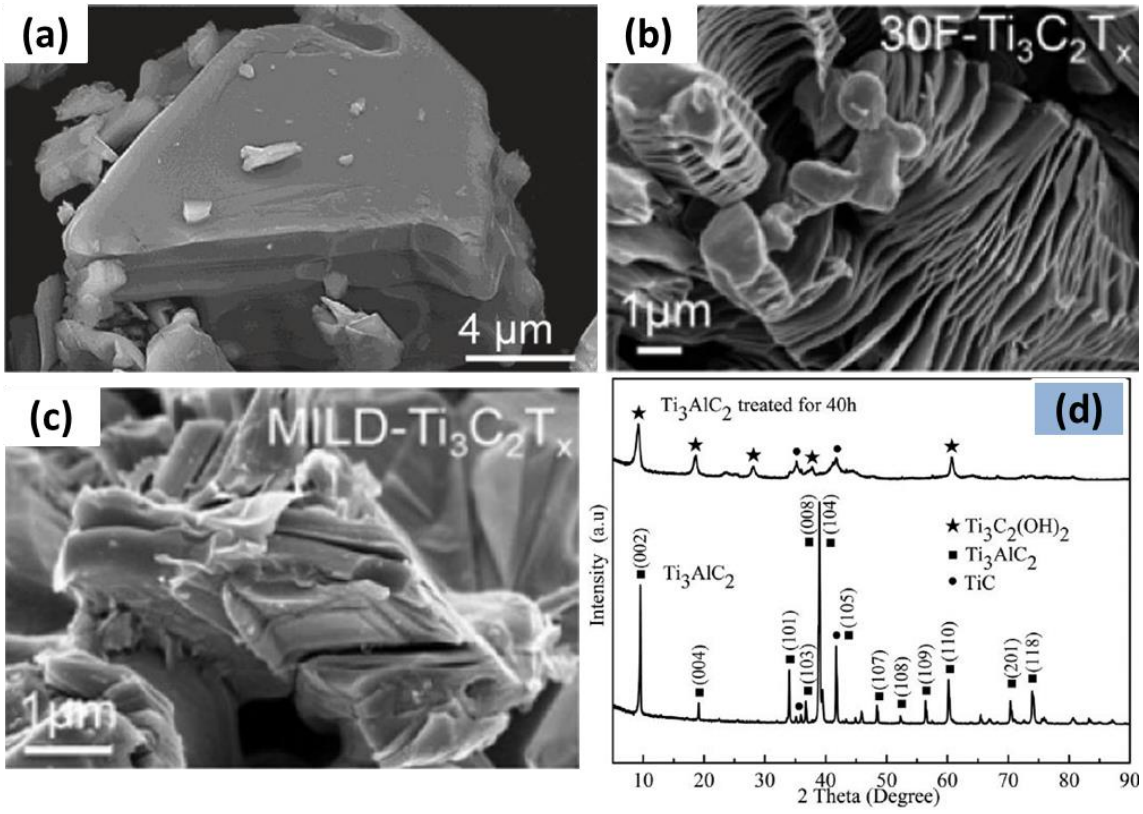

Figure 1-6: This figure shows the morphological and structural characterization of MAX

and MXene phases. (a) the morphological structure of MAX material is shown with Scanning Electron Microscope (SEM) image, ref[43]. (b) SEM image of ML-MXene after etching with 30 wt.% HF, ref[26]. And (c) Minimally intensive layer delamination (MILD) ML-MXene produced by in-situ HF etching method by the reaction of LiF/HCL, ref[26]. (e) Crystal structure of MAX and MXene, which is produced by etching with LiF/HCl solution revealed by XRD patterns, ref[42].

The fabrication process of $Ti_3C_2T_x$ MXene membranes can be done using several methods like spin coating[44–46], spray coating[47,48], rolling [49,50], and vacuum-assisted filtration (VAF) process[51,52] (Figure 1-7). For example, VAF process utilizes polyvinylidene difluoride (PVDF) substrate with a 0.45 µm micro sized membrane using suspended DL-MXene solution to obtain a smooth surface MXene membrane for applications like electrochemical capacitor electrodes and battery application[28]. This process allows the MXene sheets to restack themselves in such a well-defined interlayer distance and slit-like channels facilitating the charge and size-selective ion sieving process[53].

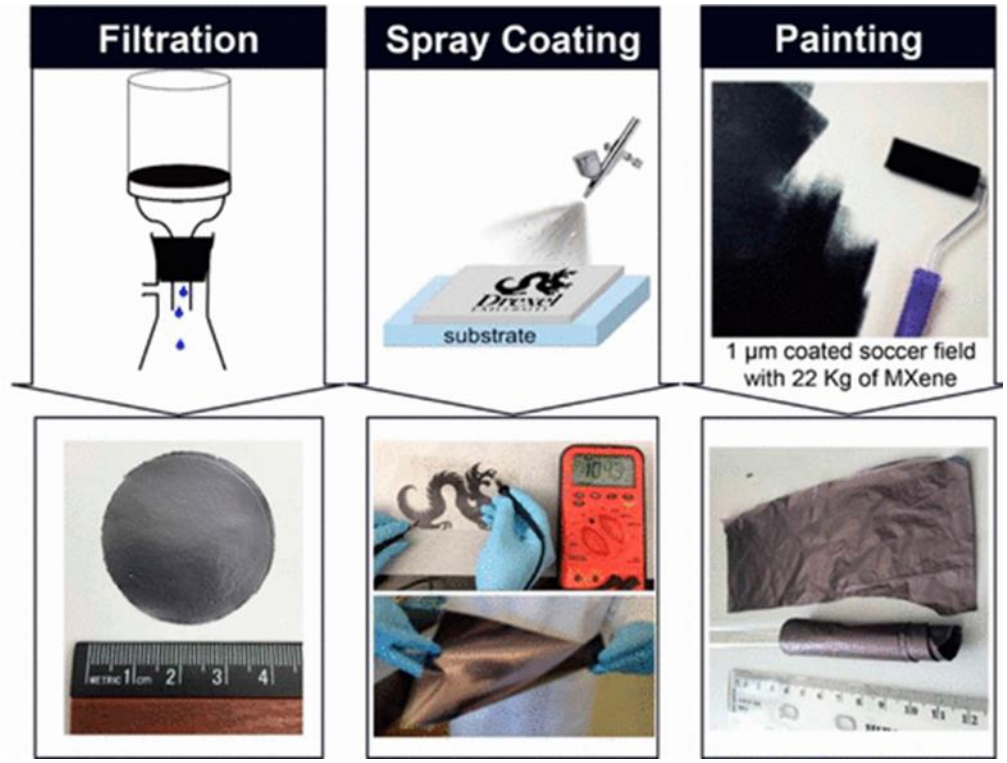

Figure 1-7: Various fabrication methods of $Ti_3C_2T_x$ (MXene) on a flexible substrates ref[26].

Due to the unique properties of MXene and the available methods of fabrication (Figure 1-7), it was worth investigating the properties and application of MXene as a membrane. Ren et. al. [53] produced the first MXene membranes via VAF from colloidal $Ti_3C_2T_X$ solution on a hydrophilic polymer substrate to form a binder free and flexible MXene membrane. This method allowed the formation of a well-defined interlayer distance and channels acting as separation membranes for charge and size-selective ion sieving with nice water flux and excellent separation of ions dependent on the charge and hydration size of the ions[53]. Li Ding et. al.[41] found that MXene membrane on anodic aluminum

oxide substrate (AAO) showed superb water permeance with a favorable rejection rate for molecules 2.5 nm or larger[41]. The unique structure and well-defined interspace of MXene membranes allow their use in applications like gas separation where it follows a size exclusion mechanism. The method by which the MXene membrane is synthesized can affect its stability where HF route introduces a very intense effect compared to *in-situ* HF route, which is dependent on many factors like the intercalation of cations between the MXene sheets.

1.3 MXene ionic intercalation in aqueous media with emphasis on intercalation in MXene membranes:

Ionic intercalation of MXene can help to stabilize the material by the electrostatic force resulted between the positive intercalated ions and the negatively charged MXene[15,54]. For example, Osti NC et. al[54] observed that intercalated potassium cations can stabilize MXene membranes under a hydrated and dynamic environment. Moreover, it helps in de-mobilizing hydrated water molecules between the MXene sheets and produces a homogenous layered structure, unlike pristine MXene. This process can be explained by XRD peaks, where the K^+ intercalated MXene with a sharp peak at 24.63 Å and pristine MXene with a broaden peak at 19.88 Å (Figure 1-8), which demonstrates the d-spacing increase in MXene layers when intercalated with potassium ions and higher crystallinity[54]. In addition, Li ions, which are part of the in-situ HF synthesis process, can improve the crystallinity as well as decrease the ooo1 peak position in the X-ray diffractometry[15]. Typically, the intercalation of MXene with cations is due to the negatively charged MXene sheets. This was confirmed by EDS where cations can be detected in MXene sheets when immersed in different salts. Additionally, the higher the PH of the solution, the more effect on the d-spacing[55].

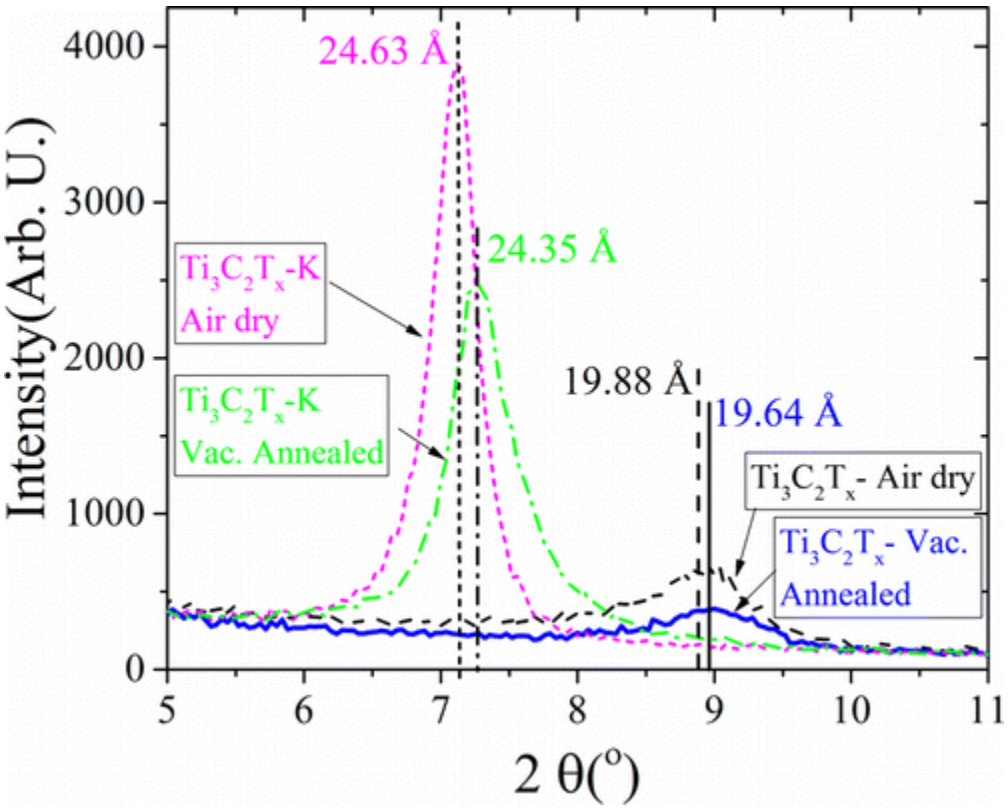

Figure 1-8: XRD pattern for MXene and potassium intercalated MXene for before and after vacuum annealing as shown in the figure[54].

when intercalating with cationic polymers[52,56]. For example, the negatively charged MXene layers allow the cationic polyvinyl alcohol (PVA) to wrap itself around the MXene sheets. This wrapping results in polymer composite with interesting properties. These properties include flexibility and high conductivity that can reach up to 2.2 × 104 S/m. Such properties allow the composites to be used in several applications including energy storage and water filtration[52]. Another interesting composite example is the MXene\PANI composite where it produces a unique wavelength absorption property with

a maximum reflection coefficient of −56.30 dB at 13.80 GHz with a specific thickness that can be attributed to the dielectric property of MXene[56].

Intercalated cations can have different hydrophilicity. When increasing the charge to size ratio of the hydrophilic cations (i.e., Li^+, Mg^{2+}, and Al^{3+}), the amount of water molecules inserted between the interspace of the MXene increases unlike the hydrophobic cations (i.e., Cs^+ and Tetraethylammonium (TEA^+)), which disrupt the existing interspace water molecules between the MXene sheets[57]. Hart JL et. al.[58] found that removing the intercalated cations can increase the MXene conductivity. Moreover, removing the functional groups can further increase the conductivity of MXene, which was observed in an in-situ heating TEM experiment when MXene was heated up to 775 C[58]. The pre-intercalated MXene with Al^{3+} allows full lithiation of Li^+ ions in battery storage application due to the increased interlayer space of MXene films[59].

As previously mentioned, MXene is a conductive material. Lin Z et. al.[60] used this property when applying an external voltage to intercalated MXene with bis-(trifluoromethylsulfonyl)-imide ($TFSI^-$) and 1-ethyl-3-methylimidazolium (EMI^+) ions decreasing the interlayer spacing between the MXene layers with positive voltages. This process may be related to the removal of EMI^+ ions, known as steric effect, or the electrostatic attraction derived from the intercalation of $TFSI^-$ ions. Whereas, the d-spacing increases with negative polarization of the MXene due to the intercalation of the cations[60].

Fouling and low flux are two of the major difficulties facing membrane-based separation processes. Moreover, biofouling has been shown to hinder the performance of nanoporous membranes including durability, flux, and rejection rates. Pandey et. al.[61]

partially modified the surface $Ti_3C_2T_x$ sheets with different mass loadings of silver nanoparticles (AgNPs; 0–21 wt %) improving the antifouling and water permeation of MXene membrane. The 21% loading of AgNPs/MXene membrane (Figure 1-9.a) displayed an improved water flux of (~ 420L m^{-2} bar^{-1} h^{-1}) and rejection of rhodium B (RhB) (79.93%) and methyl green (MG) (92.32%) (Figure 1-9.b,c). The increased water permeation of the specific membrane is due to the created slit interspace by the intercalation of silver nanoparticles between MXene sheets (Figure 1-9.a) and average pore size of 2.1 nm. Furthermore, the same membrane showed antifouling properties where the growth inhibition of the E. coli was 99%.

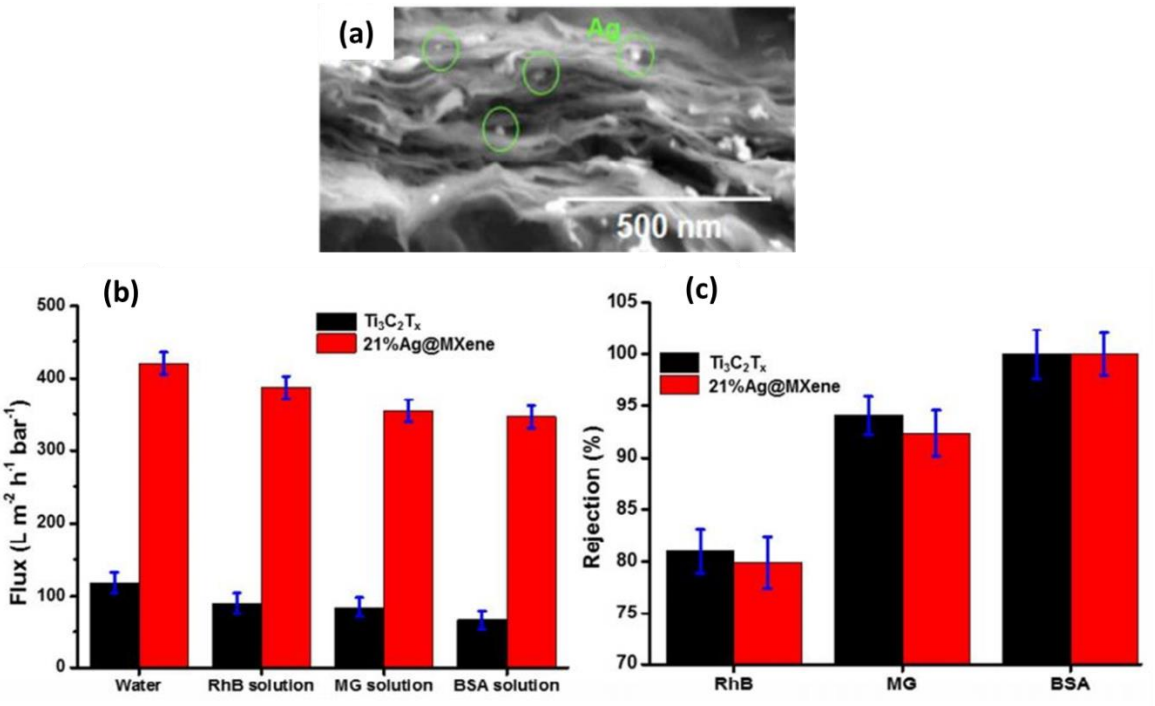

Figure 1-9: SEM cross-section image of the 21% Ag@MXene membrane showing

AgNP, (b) flux and (c) rejection comparison of the MXene and 21% Ag@MXene membranes performance for the separation of MG, RhB and bovine serum albumin (BSA) molecules at 25 °C Ref[61].

1.4 A Comparison of ion sieving mechanism between MXene and GO membranes:

Graphene Oxide (GO) has a carbon lattice that consists of aliphatic six-membered rings and aromatic entities with some unoxidized benzene rings with sizes dependent on the extent of oxidation and distributed randomly. Its basal plane primarily contains epoxy oxygen and hydroxyl groups unlike edges that have hydroxyl and carboxyl groups (Figure 1-10). The almost flat carbon grid may have a slightly distorted tetrahedral configuration as a result of the hydroxyl groups attached to some carbons giving a wrinkling shape for the layers[62]. Due to the similarity of the 2D structure of GO and MXene membranes, it is interesting to use this membrane as a reference in this work.

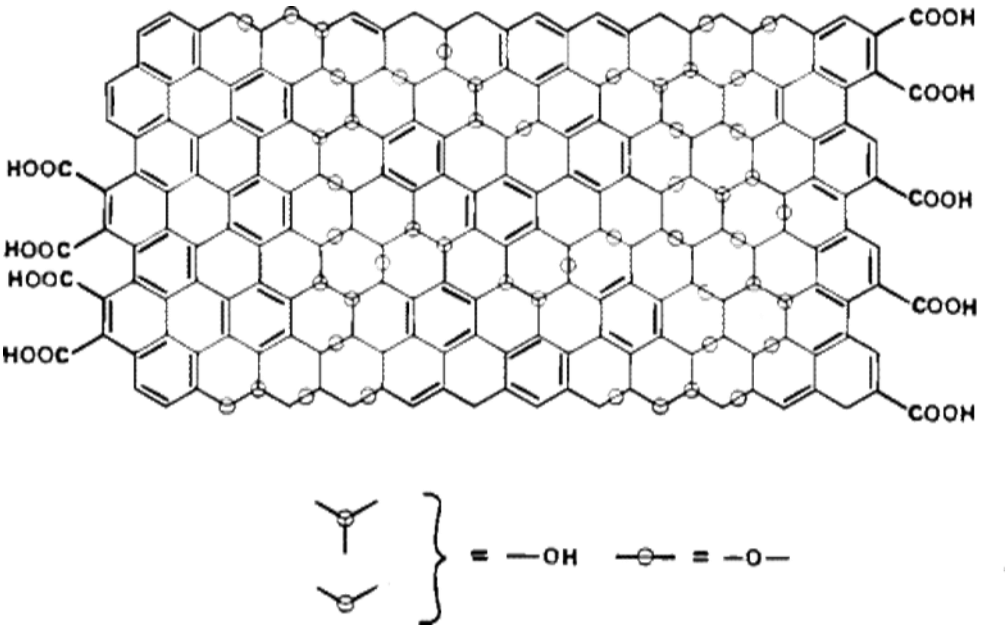

Figure 1-10: The modeled structure of GO

MXene has a better selectivity towards cations than GO, where higher charged ions can be trapped between the MXene interlayer spaces. This phenomenon is due to the negative charge of the MXene sheets, which reacts with the positively charged ions allowing for charge and size rather than the adsorption mechanism[53]. MXene's unique property of ion selectivity can be tuned by applying external voltage[53]. The produced membrane of the previously mentioned study had a water flux of ~37.4 L $.bar^{-1}$ $.h^{-1}$ $.m^{-2}$ with remarkable ion separation that depends on the charge of the ions and their hydration radius. Multivalent cations (Mg^{2+} and Al^{3+}) had a slow diffusion rate through $Ti_3C_2T_x$ membranes compared to monovalent cations (Li^+, K^+, Na^+) that were order of magnitude faster permeability during concentration gradient-driven diffusion. Furthermore, cations with larger hydration radii smaller than the interlayer spacing of MXene (~6 Å) showed a permeation rate of one order of magnitude slower when compared to smaller ones[53] (Figure 1-11).

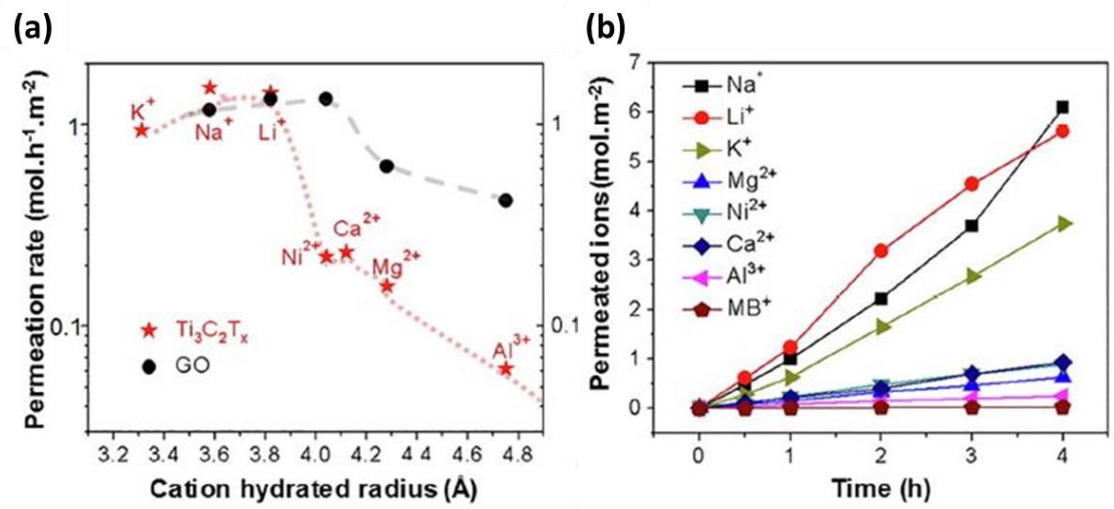

Figure 1-11: The graphs shows (a) a comparison between MXene and GO membranes with respect to permeation rate of different cations having different hydration radii, and (b) The amount of different cations permeated through MXene membranes, ref[53].

In GO membrane, the cation-π interaction plays a major role in the cation intercalation; however, in some cases, the temperature can overcome this mechanism, such as in the occasion of Mg^{2+} cations. The overall effect of cations intercalation can be under the size exclusion mechanism[21]. Ding et. al.[63] observed that small size molecules like H_2 and He have a faster permeation than those of larger size like N_2 gases in terms of passing through MXene membranes. This phenomenon is due to the confinement in MXene Nano sheets that act as a gas separation related to the gas diameter instead of the molecular weight, which follows size exclusion mechanism[63].

1.5 Stability and the effect of environment on MXene membranes:

Understanding the stability of MXene requires a great deal of knowledge concerning the nature of intercalated cations, water, and the interlayer space interactions. Various studies have paid particular attention to cation intercalation highlighting the basal swelling of MXene, their spontaneous intercalation[55], and their impressive electrochemical performance[15,55]. Moreover, for many MXene delamination techniques, cation intercalation is deployed to acquire an aqueous, colloidal greenish suspension that can be used to synthesize different membranes and filters with some unique properties depending on the intercalated cations[53,64].

Li^+ intercalated $Ti_3C_2T_x$, which is produced by in-situ HF deploying (HCl/LiF) solution, has a two water layer (WL) in its basal spacing, which is equivalent to approximately 16Å when the MXene is fully hydrated, while another study showed 15.5Å for intercalated two layers of water (figure 1-12) [65]. In contrast, it was shown that 1 WL basal spacing is more stable and exists in most humidity ranges. Other studies have confirmed the same in aqueous solution, where the Li^+ intercalated MXene does not swell fully to 16Å but stops at 12.5Å[55,65,66]. These results prove the heterogeneity and coexistence of different water hydrations in MXene interstratified crystals, which will be seen later in this study.

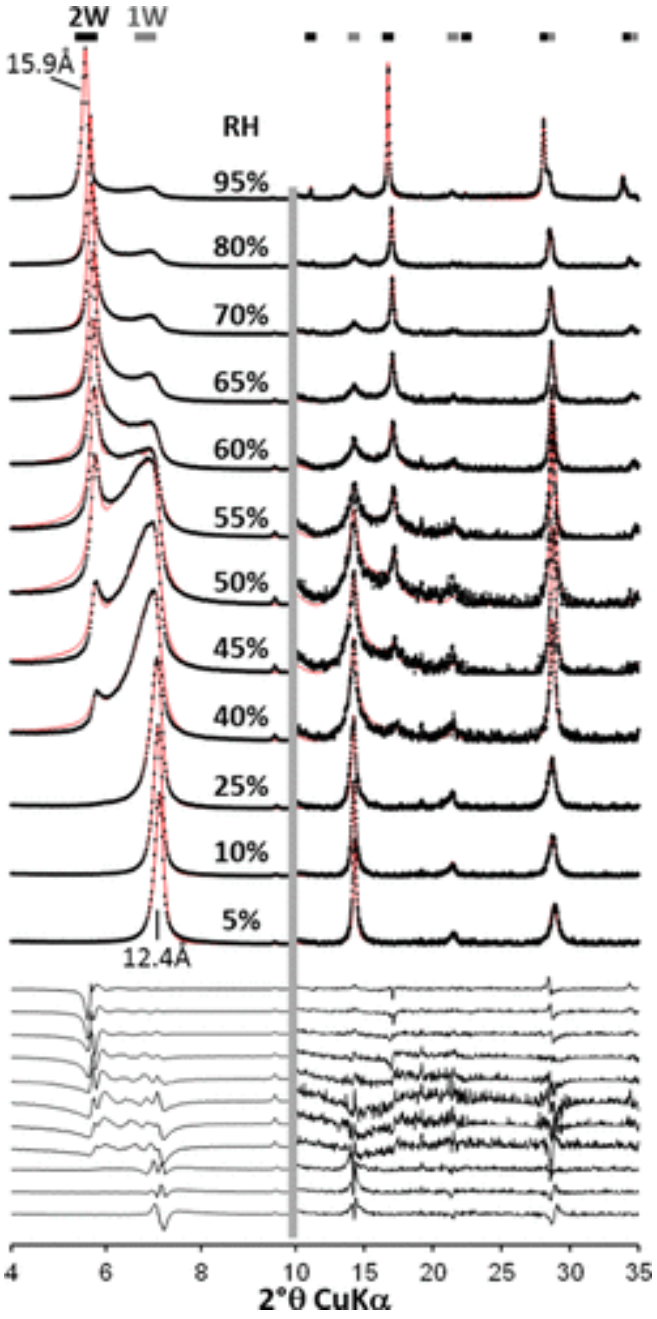

Figure 1-12 : *in-situ* XRD pattern Comparison of 00l reflections for Li-saturated $Ti_3C_2T_x$ MXene as a function of relative humidity (RH) between calculated (red lines) and experimental (black crosses) intensities Ref[65].

Ghidiu et. al. [67] managed to successfully exchange the Li^+ with potassium, sodium, rubidium, magnesium, and calcium cations in MXene as shown by their XPS and EDS results. It was found that the exchanged cations swell and contract the MXene material in response to changes in humidity with variant effect depending on the hydration of each cation. Moreover, the 002 peak change in the XRD experiment of this study in response to the water hydration was discontinuous in the direction normal to the basal plane as shown in (Figure 1-13). The authors claim this effect explains the expansion of MXene when exposed to different relative humidity. The previous study was substantiated by using in-situ relative humidity XRD. Cooper Voigt et. al.[68] found that larger anions from the etching process can improve the intercalation of cations in the interlayer spacing of MXene layers. The size of anion attached to the positively charged ML-MXene edges can prop open the MXene sheets. This phenomenon was seen when etching the MAX to MXene using salts like HBr, HI, H_2SO_4, or H_3PO_4 acids in combination with HCL and different post-treatment procedures [68].

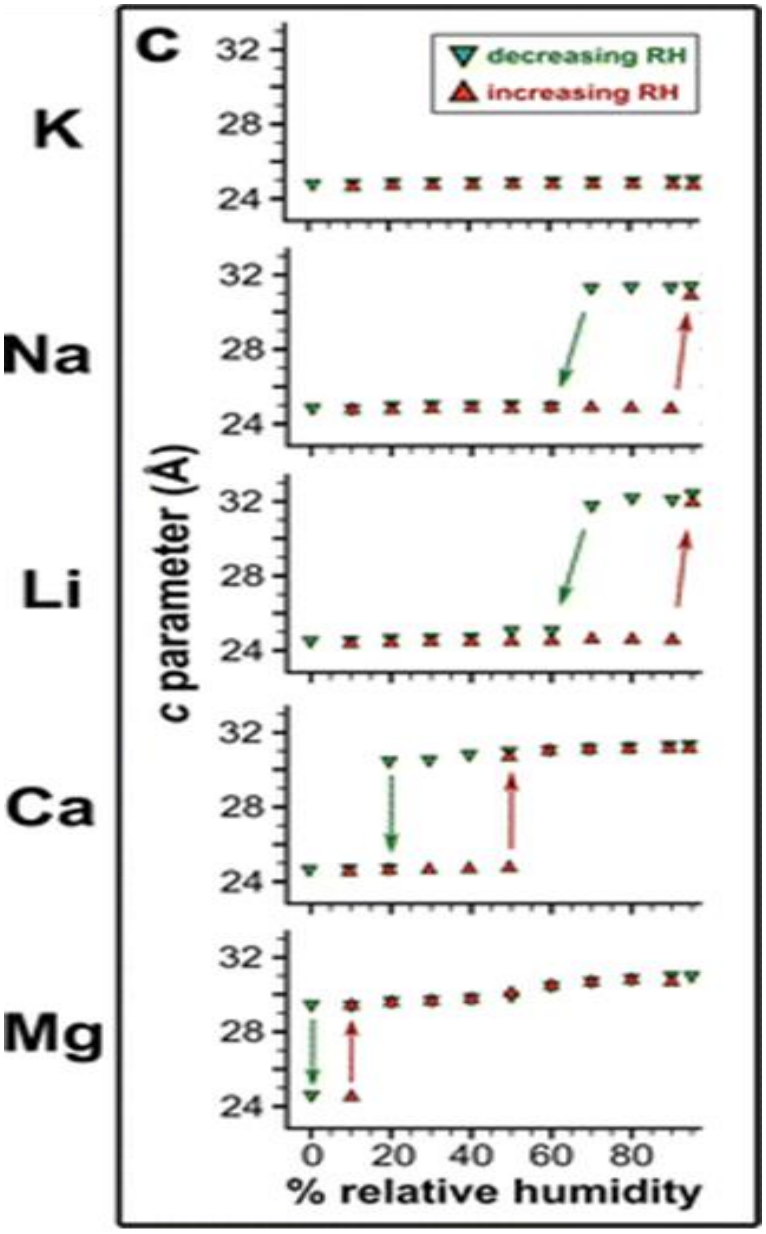

Figure 1-13: The c parameter (2 × d002) extracted from the XRD peaks as a function of RH (relative humidity). Green down triangles represent the path from 95% to 0% RH and red up triangles the path from 0% to 95% RH following the down path. Data are organized by intercalated cation in order of increasing hydration enthalpy[19].

Mykola et. al.[69] studied three types of VAF fabricated Ti_3C_2 membranes that were etched with 5%, 10%, and 30 % of HF and delaminated using tetramethylammonium hydroxide (TMAOH) as an intercalant. The TA-MS (Thermal Analysis- Mass Spectroscopy) of the three fabricated membranes showed the same patterns (Figure 1-14.a), which means the post-treatment of these membranes makes their surface terminations relatively similar. Figure 1-14.b shows the mass spec. for MXene membrane treated with 10% HF. Due to the TMA^+ occupancy on the surface termination of the MXene membrane, there is no water peak detected in the mass spectra. Instead, a multistage release of the intercalant was observed. The first peak starts at 84 °C for TMA^+ between the MXene layers, but not bounded directly to the MXene surface, where the TMA^+ decomposes to $NH_2/NH_3/NH_4^+$ that results in 2.1 wt % loss. The decomposition and thermal desorption of the adsorbed TMA^+ on the surface of MXene begins at 300 °C. The final stage of decomposition of TMA^+, which likely resides at defect sites, starts at 460 °C as the intercalant is with a higher coordination. The release of CO and CO_2 at 840 °C is the start of the transformation of the MXene membrane to cubic TiC.

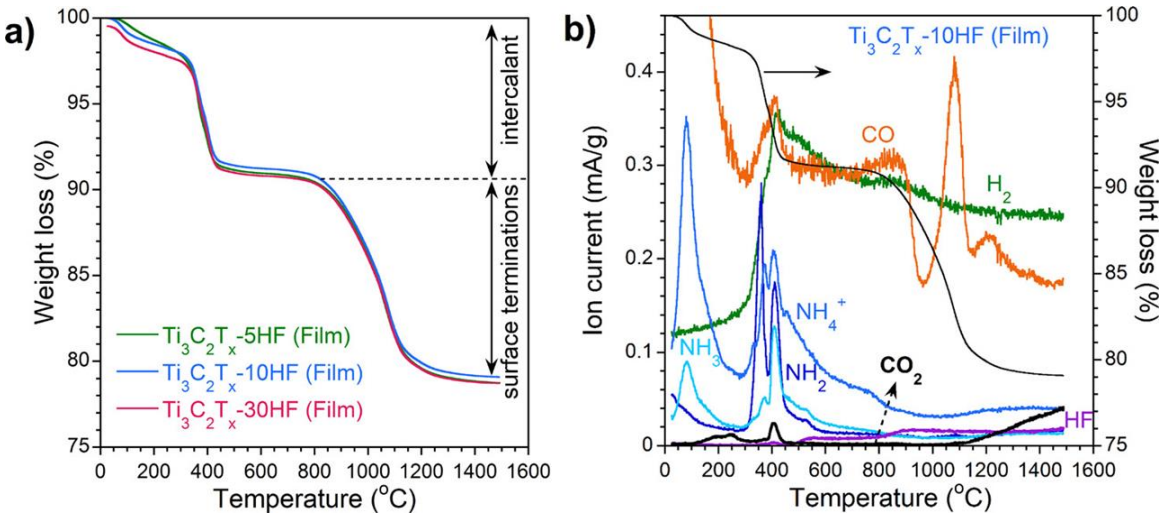

Figure 1-14: TGA curves for free-standing $Ti_3C_2T_x$ membranes intercalated with tetramethylammonium hydroxide (TMAOH): (a) is the curve for all the membranes $Ti_3C_2T_x$-5HF (5 wt % etched with HF), $Ti_3C_2T_x$-10HF (10 wt % etched with HF), and $Ti_3C_2T_x$-30HF (30 wt % etched with HF) and (b) the mass spectra of $Ti_3C_2T_x$-10HF membrane ref [69].

At the time of writing of this thesis, there has been no study showing effect of intercalated cations in MXene membranes under high temperature conditions.

This work focuses on the effect of cations on the stability and stacking of MXene membrane sheets under high temperatures and different relative humidity. By intercalating MXene with different cations while fixing the anion counterpart, we discovered that different cations from various ionic states indeed play a vital role in the structural changes of $Ti_3C_2T_x$ membranes under high temperatures. Na, Ca, and Al cations were used as our main cations. However, we find an interesting effect from the

in-situ HF produced MXene when Li cation intercalate between MXene membranes. In the remainder of this discussion, we make our case using in-situ XRD where temperature of the sample was increased systematically by a DSC attachment to the XRD to increase temperatures, and we proved further the XRD results with in-situ ESEM observation by the use of special heat stage attached to our SEM. Moreover, the relative humidity had a swelling effect on the different MXene membranes, which will be discussed in detail later on.

Chapter 2 Experimental

2.1 Materials:

- Aluminum Titanium Carbide Powder (Ti3AlC2 which is MAX phase) (Y-Carbon- Ltd, Ukraine)
- Hydrochloric Acid (SCP, chemically pure)
- LiF Sigma Aldridge
- Ethanol Absolute (Sisco Research laboratories, Mumbai, India)
- Magnet beads for stirring.
- De-ionized water from Elga systems
- Potassium chloride (SCP, chemically pure)
- Calcium chloride (SCP, chemically pure)
- Aluminum Chloride (SCP, chemically pure)

2.2 Equipment:

2.2.1 XRD-DSC (smart lab, S-max 3000):

X-Ray Diffraction (XRD) from Rigaku with model name Smartlab (figure 2-1) was used in the XRD analysis of this study. XRD system consists of a sealed X-ray tube,

goniometer, scintillator counter for XRD measurement, heat flux DSC unit along with sample position, and DSC control unit.

XRD is a versatile nondestructive technique that is used to identify crystalline properties, such as crystalline structure, lattice constant, dislocation density, and more. Several types of XRD configuration exists including Bragg Brentano measurement, the most commonly used for bulk materials, and grazing incidence XRD for thin film samples among others. XRD systems can be equipped with several attachments allowing an in-situ characterization by changing specific conditions or environment while observing the crystal structure changes of the studied material. Here, XRD with a DSC attachment is used. The X-ray tube in this particular system is similar to that of conventional XRD where X-ray is generated by heating the filament with a specific voltage and current producing electrons that are accelerated towards a positive anode material. These electrons hit the anode at high speed resulting in Cu-Kα1 characteristic X-ray with λ=1.5405 A ° that is directed towards the sample under examination. The X-rays react with the sample resulting in characteristic X-rays when Bragg's law (equation 1) is satisfied with specific intensity. These produced X-rays are collected with a special detector that read and convert this signal to spectra that can be read on the computer monitor. The goniometer system in this model uses the parallel-beam geometry instead of Bragg-Brentano, focusing where it can correct the significant peak position shift produced by the thermal expansion of the material at high temperatures.

$$2d_{hkl}\sin\theta=n\lambda \qquad \text{Equation 1}$$

DSC unit: (Figure 1-2) shows a schematic diagram of the DSC unit. Two sample holders made from aluminum material are set next to each other, where one of these holders are used as a reference for the measurement of DSC signal, and the other holder is where the sample is placed. The two holders are placed inside a thermally conductive material (i.e. silver) prior to being positioned inside a thermally insulating material, which is usually ceramic. These two containers have two opened windows to allow the X-ray from the source and the sample to pass through them. These openings are covered with a thin aluminum foil to prevent heat conversion and loss. The specimen is kept stationary during the measurement, and it can be heated from room temperature to 300-degree Celsius.

Figure 2-1: Rigaku X-ray diffraction combined with DSC unit (model: smart lab) (HBKU-QEERI-Core labs).

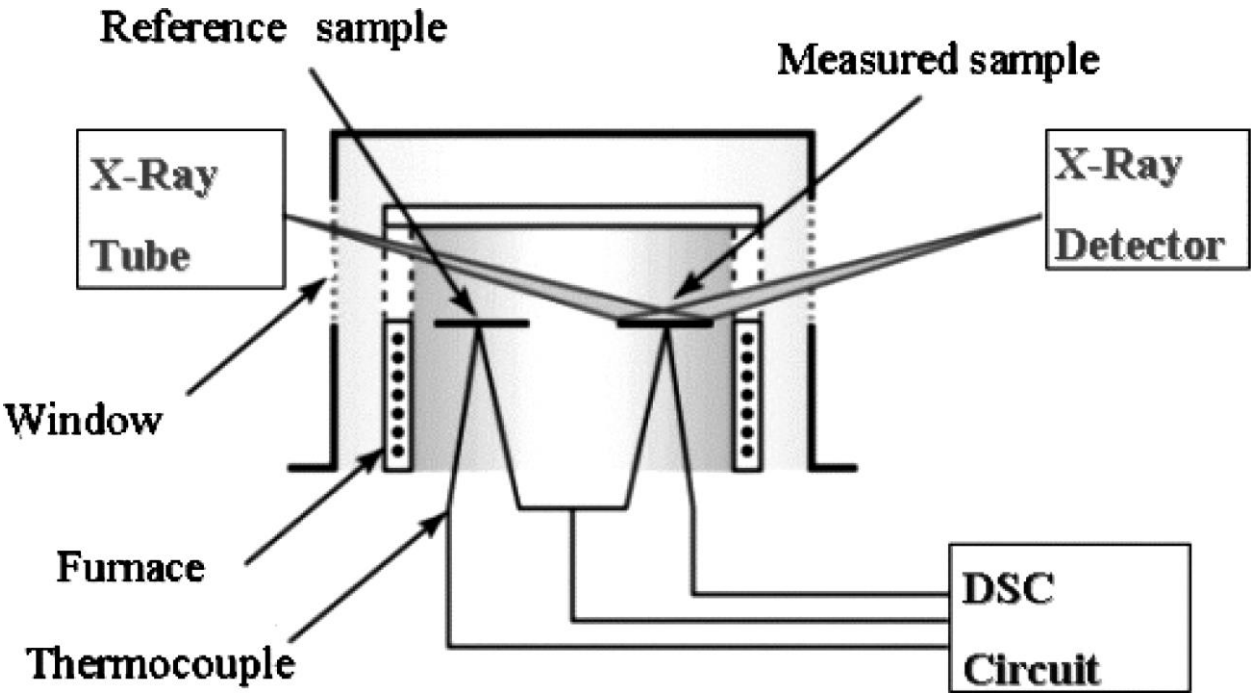

Figure 2-2: DSC unit diagram inside the XRD system. X-ray goes through a delicate window to hit the sample then the signal goes out towards another delicate window, while measuring the DSC signal ref.[70].

2.2.2 Environmental Scanning Electron Microscope (SEM); Quanta 650 FEG:

Scanning Electron Microscope is a widely used system due to the high image contrast, resolution, and depth of focus[71]. The narrowly focused electron beam is used to construct the SEM image. In general, the electron column constructed from an electron gun at the top, which generates electron beam, directs the beam toward the sample through a set of lenses that further focus the beam. A final set of lenses are used to scan the focused beam over the sample (figure 2-3). An interaction volume is generated when the electron beam

hits the sample resulting in several signals as illustrated in (Figure 2-4); however, the secondary electron (SE) and characteristic X-rays will be the ones used in this work.

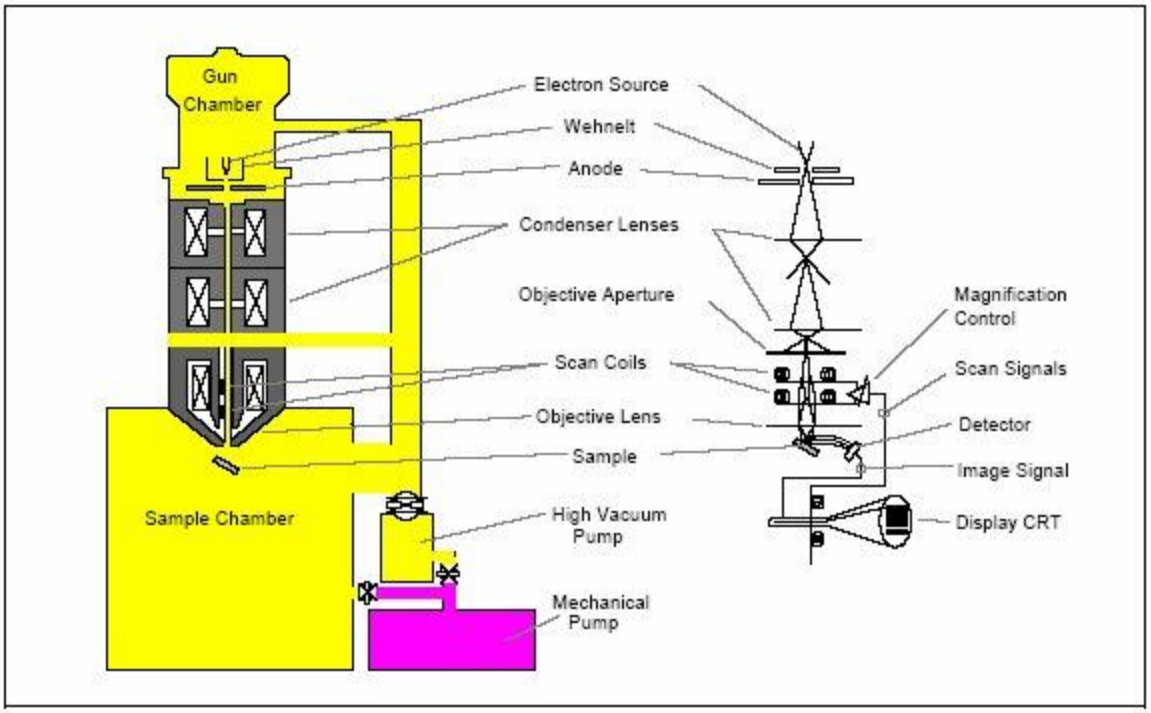

Figure 2-3: schematic of Conventional Scanning Electron Microscope (courtesy Philips Electron Optics. ref[72]).

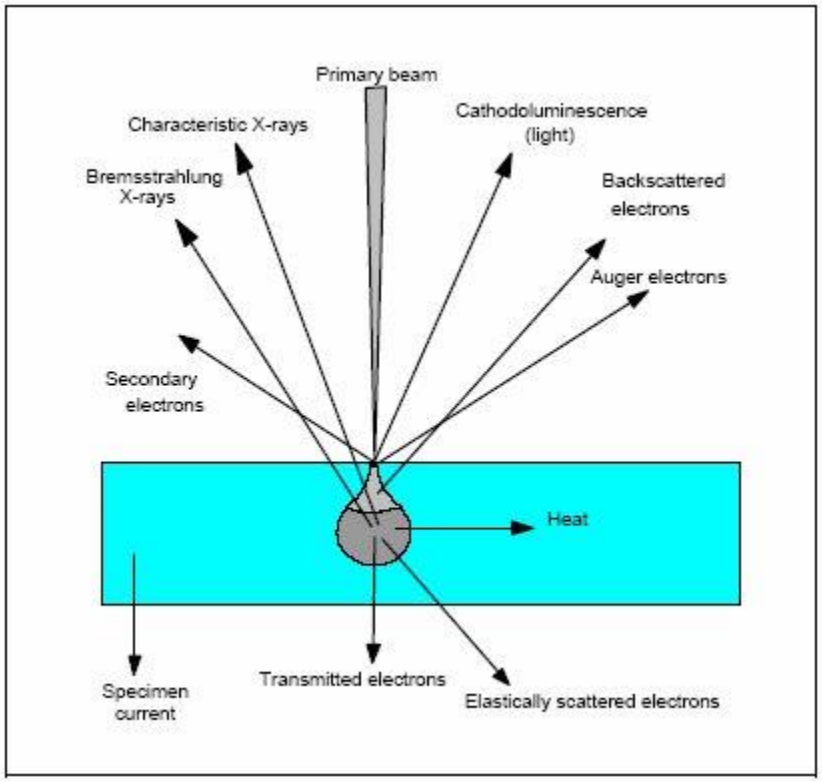

Figure 2-4: signals produced as a result of beam interaction with the sample (courtesy Philips Electron Optics. ref[72]).

Environmental-Scanning Electron Microscope (E-SEM) is instrumental in revealing the morphological changes under different pressure values. This new feature is enabled by multiple pressure limiting apertures and its unique environmental secondary electron detector, which was published out of Danilatos [73] investigation to image sheep wools. Conventional SEM works under high vacuum that exists in the electron gun and throughout the column and chamber area as air molecules scatter electrons producing a beam skirting effect and, consequently, affecting the resolution of SEM images. Contrary to the E-SEM mode, chamber area can sustain higher pressure than that of the column

due to the multiple limiting apertures located between the chamber and the column that limit the flow of chamber gases back to the column. These apertures reduce the beam scattering effect to the beam path between the apertures (column end) and the sample (Figure 2-5).

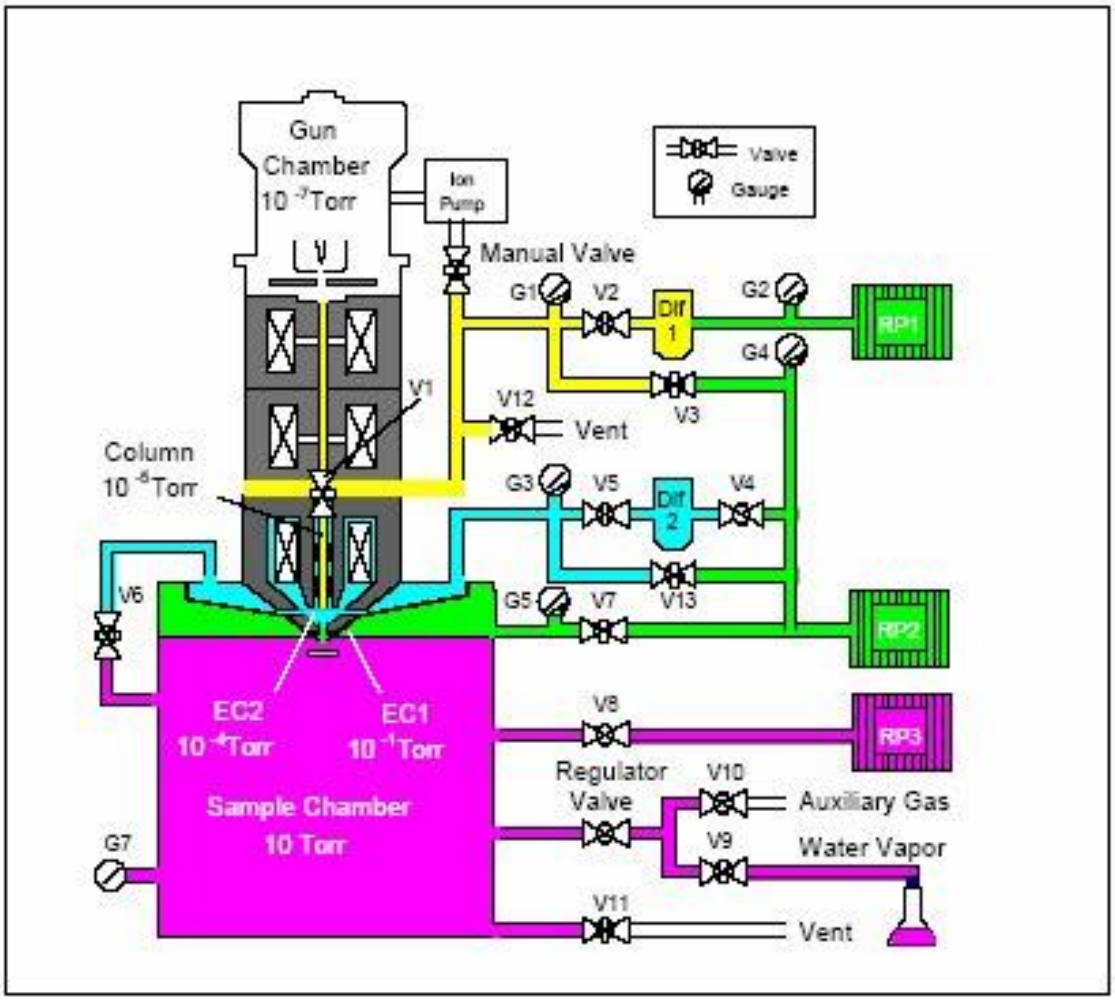

Figure 2-5: general ESEM schematics. The two transitional environmental chambers (EC1 and EC2) pressure are increased due to the pressure limiting apertures (courtesy Philips Electron Optics.ref[72]).

E-SEM mode allows chamber pressure control through an automatic metering valve. Water vapor is traditionally used to vary the chamber pressure. However, other gases can be used bearing in mind their flammability, toxicity, and chemical reactivity (water vapor was used in this study).

One of the main concerns related to imaging in E-SEM mode is beam scattering due to the molecules inside the chamber. This scattering happens in the shape of a skirt, which is called beam skirting effect, where some of the electrons have a probability of hitting some of the molecules in the high-pressure chamber and diverting from its main path towards the sample. However, the beam skirt radius (in microns) is more significant than that of the beam (nanometer scale), making it insignificant. The beam skirting effect can be decreased significantly by increasing the spot size/beam current and the chamber pressure. The E-SEM system is equipped with a wet STEM stage that allows it to go as low as -30 degrees by utilizing Peltier principle. Furthermore, the specimen cooling combined with controlled pressure *via* introduction of water vapors will provide control over the relative humidity (RH) in the chamber, which allows the water condensation at 100% RH (Figure 2-6).

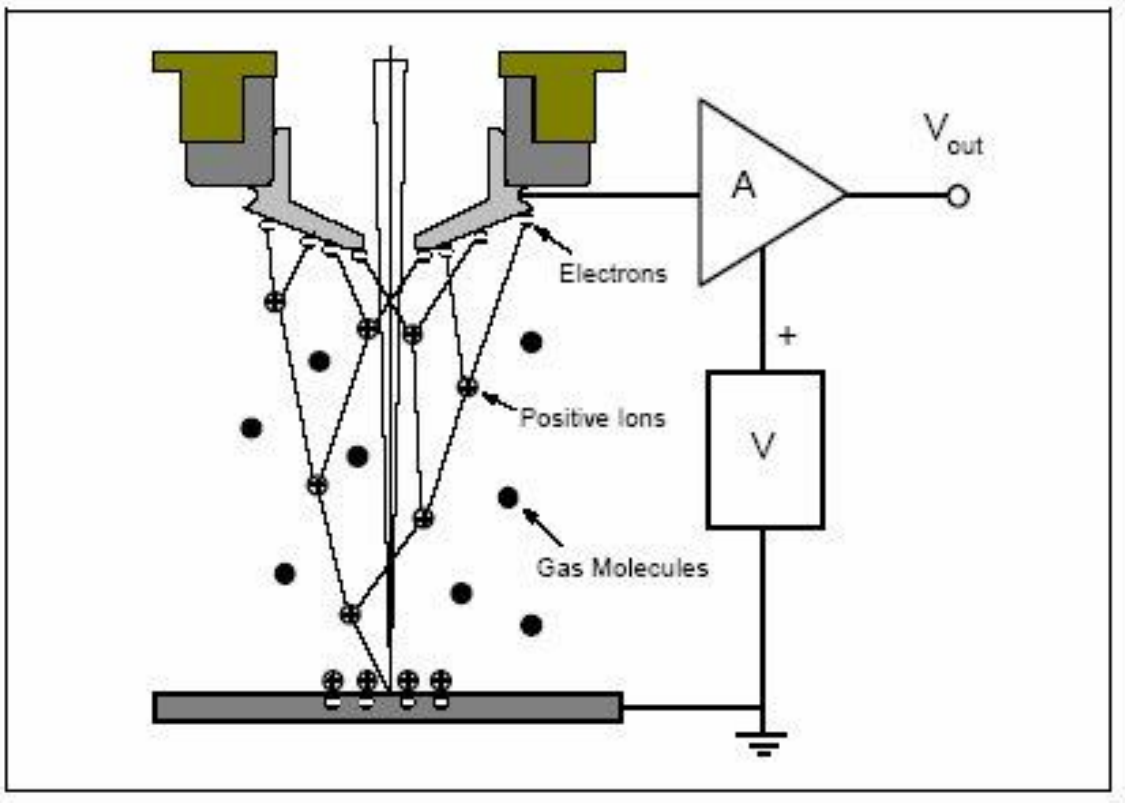

Figure 2-6: Simple schematics of the interactions between the electrons and gas inside the ESEM chamber (courtesy Philips Electron Optics. ref[72]).

The system, however, did not have a stub that allows imaging of a bulky sample like MXene cross section membrane to be imaged. A bespoke stub was engineered by using mat lab software (Figure 2-7), and an all-purpose aluminum material was chosen for the construction of the stub. In order to take the temperature gradient into consideration, a specialized alignment was done, which was part of the E-SEM system alignment. This alignment allows the system to calculate the exact temperature at a specific pressure (from the water phase diagram) where a water molecule starts to form on the surface of

the bespoke stub. The engineered stub allows the observation of a cross sectional sample and curvature of the sample to facilitate the SE signal in order to reach the ESEM's SE detector, called Gaseous Secondary.

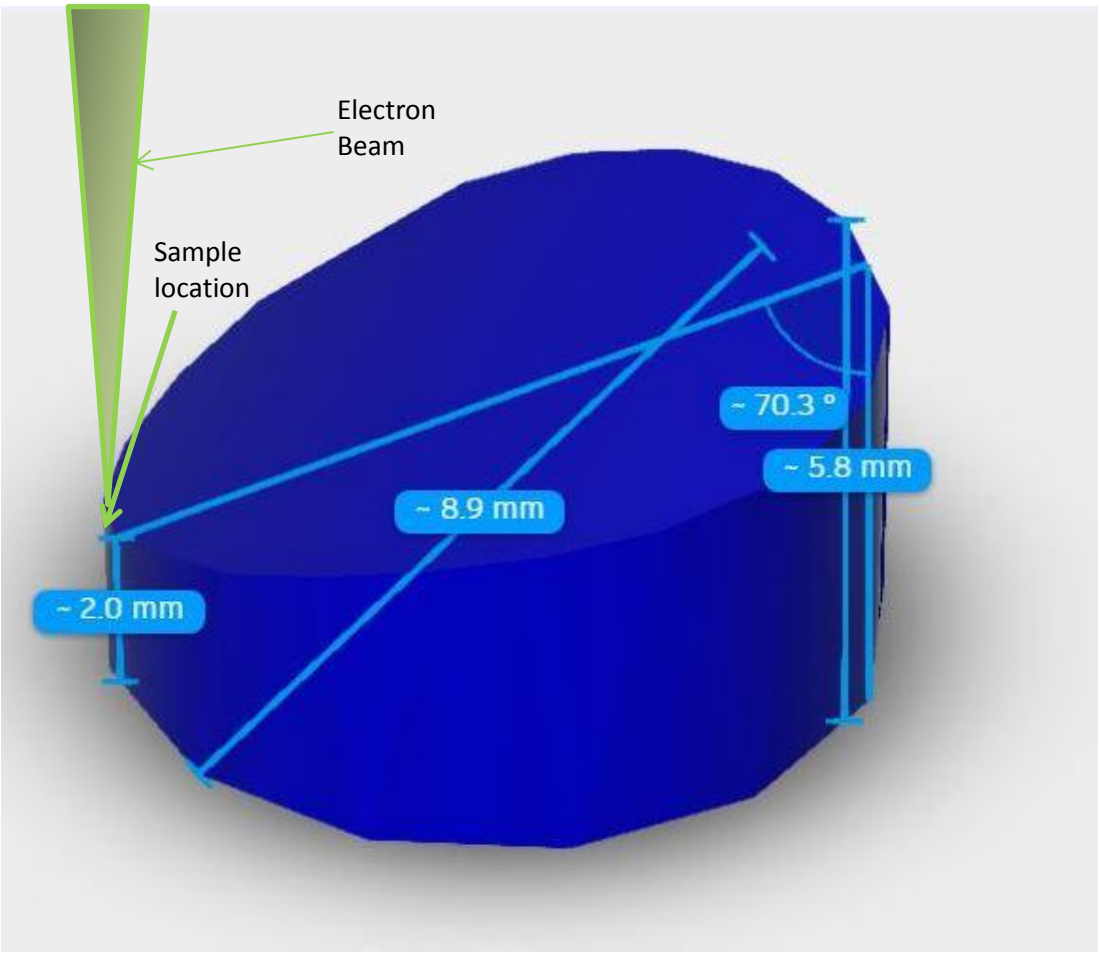

Figure 2-7: schematic of bespoke E-SEM stub to be fit in the wet STEM stage for cross sectional images of the MXene membrane.

The seated GSED detector at the end of the column works when the electron beam hits the sample surface producing SE. Consequently, the SE reacts with water molecules producing an avalanche of newly created electrons leaving positively charged ions and resulting in SE signal amplification. The newly produced electrons are attracted to the GSED positive charged end, while the positive ions are attracted to the charged surface of the sample reducing the charge effect that would have been seen in a conventional SEM for insulating samples.

Another accessory, the heating stage, can be mounted in the ESEM system where temperature-controlled experiments can be performed from room temperature to 1000°C. Quanta 650 FEG (FEI Company, Czech Republic made) was used in this study (Figure 2-8).

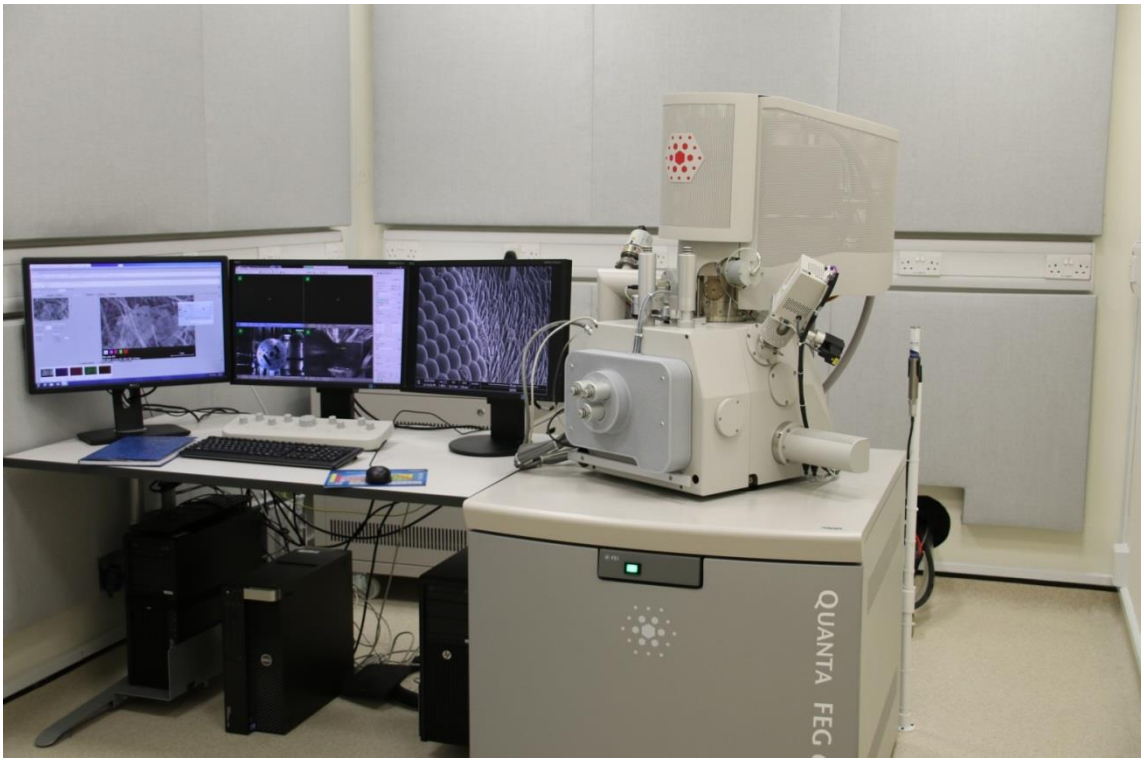

Figure 2-8: Quanta 650 FEG from FEI company, Czech Republic with Cold and hot stage for in-situ experiments (HBKU-QEERI-Core labs).

2.2.3 Energy Dispersive Spectrometer (EDS):

EDS is a qualitative analysis technique that was developed for elemental analysis of different samples, and it can be attached on the SEM system. This method of analysis relies on the production of X-rays from the electron beam (EB) interaction with the sample, namely Brehamstraung or background radiation and characteristic X-rays. Though, only the latter is of interest as it results from the inner core interactions that of unique value that determine the element. Generally, when a main high-energy electron

knocks off an inner electron from an atom, resulting in an excited atom, the atom lowers its energy by an outer shell electron to fill the vacancy in the inner shell, producing an X-ray (Figure 2-9)[74].

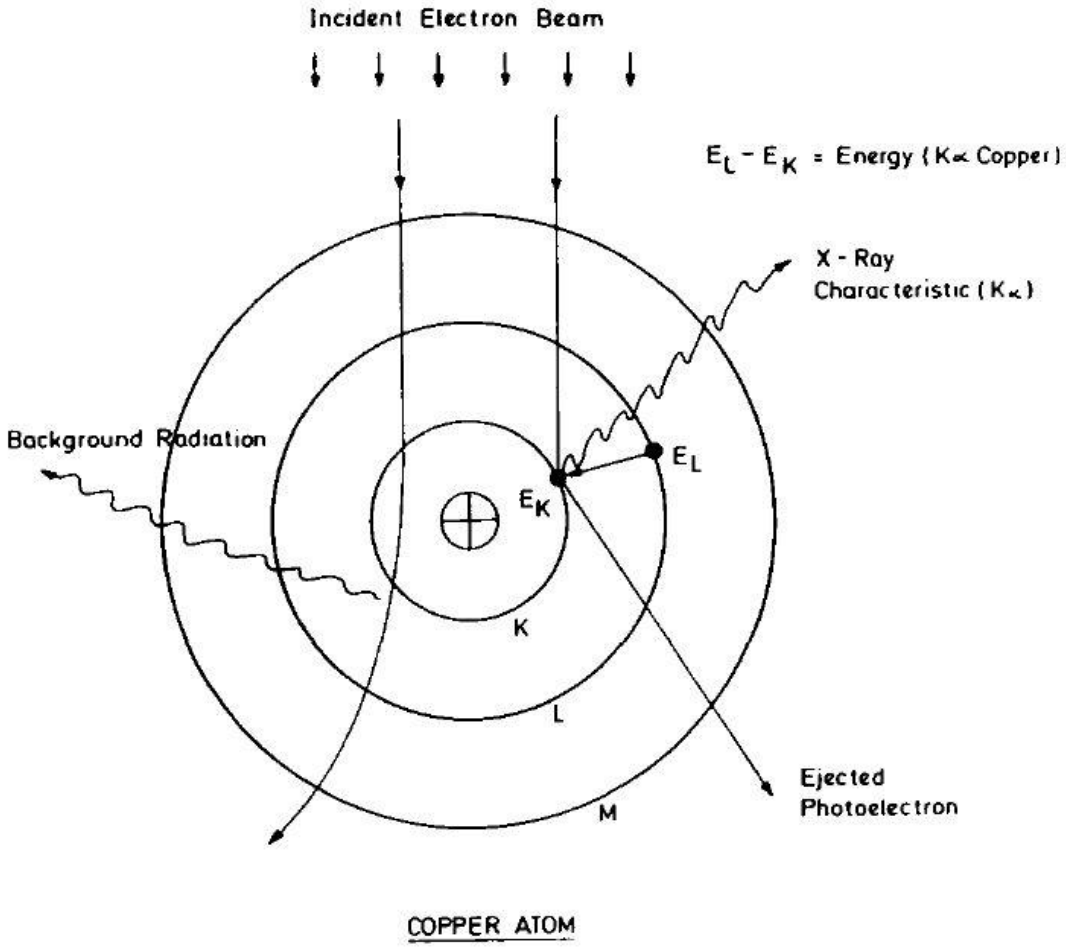

Figure 2-9: schematic of X-ray production from a copper atom as an example. (D P Lewis 1992) ref[74].

EDS can also provide a semi-quantitative analysis of the elements, and it can map the surface of the sample to determine the location of all the different elements in the sample. EDS is a complimentary system that is usually an attachment to the SEM.[74]

Elemental mapping can also be obtained from EDS to illuminate X-ray information qualitatively for a single element as a concentration map, which can be used in conjunction with an electron image. The brighter areas mean higher concentrations of mapped elements, which can be assigned a color from the user interface of the device[74]. The EDS used in this study was from Bruker with model number of XFlash6160.

2.2.4 Contact angle (drop shape analyzer from Kruss Company):

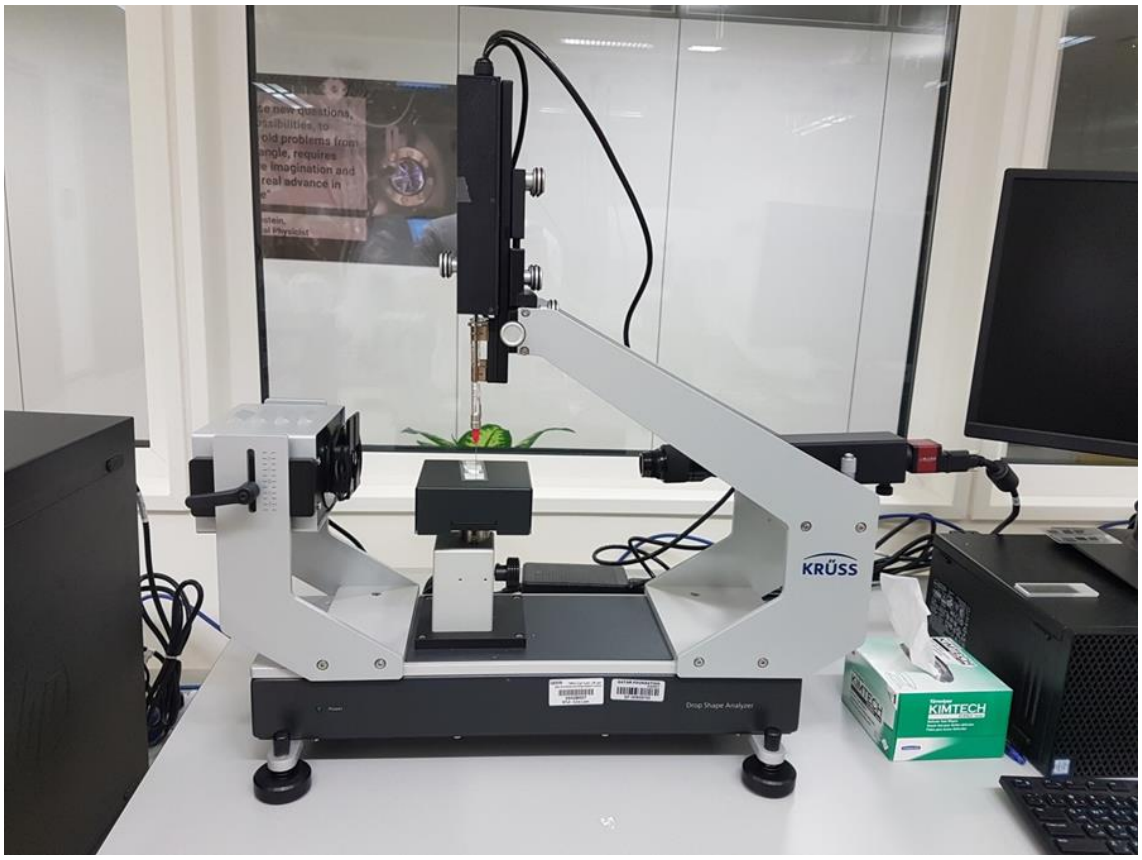

Figure 2-10: Kruss contact angle system. The sessile droplet method was used to calculate the contact angle for the samples in this study (HBKU-QEERI-Core labs).

The contact angle (Figure 2-10) is the angle produced when there is a liquid-vapor interface meeting liquid under specific pressure, conventionally 1 atm. Although there are different methodologies used to produce contact angle, the static sessile drop method was used in this study. This method uses an optical subsystem to capture the angle between pure liquid (water in this case) and its contact with the sample surface. This angle is a

representative for the wettability of the material under investigation. A measured contact angle of 90 degrees or less is usually representative of a hydrophilic material. On the other hand, a measured contact angle of more than 90 degrees is usually for hydrophobic materials. When a contact angle of 0 degrees is achieved, it means the material is super hydrophilic.

2.2.5 Transmission Electron Microscopy (TEM: Talos C):

Transmission Electron Microscope (TEM) is a highly sophisticated technique that uses a beam of electrons that transmit through an ultrathin sample section of less than 100 nm thickness, unlike beam rasttering in the SEM. The transmitted electrons that have interacted with the sample form an image that can be captured by a specialized detector or on a fluorescent screen. The TEM that was introduced by Max Knoll and Ernst Ruska in 1931 uses similar column structure as a light microscope, although lenses were replaced with electromagnetic lenses to control the produced electron beam from an electron gun. TEM, however, has a significantly higher resolution than a light microscope due to the smaller wavelength of the electrons, also called de Broglie wavelength of electrons.

In this study, Talos C from FEI was used at 200 KV (Figure 2-11) to image the samples. The samples were sonicated in isopropanol for ease of dispersion on a TEM grid and left to dry before imaging.

Figure 2-11: Talos C Transmission Electron Microscope (FEI website ref[75]).

2.2.6 X-ray Photoelectron Spectroscopy (XPS):

This nondestructive (when no etching is involved) analysis technique gives elemental analysis with quantification from the surface of the studied sample along with chemical states of these elements, especially when combined with Ultra-violet Photoelectron Spectroscopy (UPS). The surface technique mentioned here means the depth of analysis or the signal is coming from approximately 5 nm depth depending on the photoelectron energy. However, etching technique allows propping of the sample to get signals from deeper areas utilizing an Argon ion source; this process is known as depth profiling.

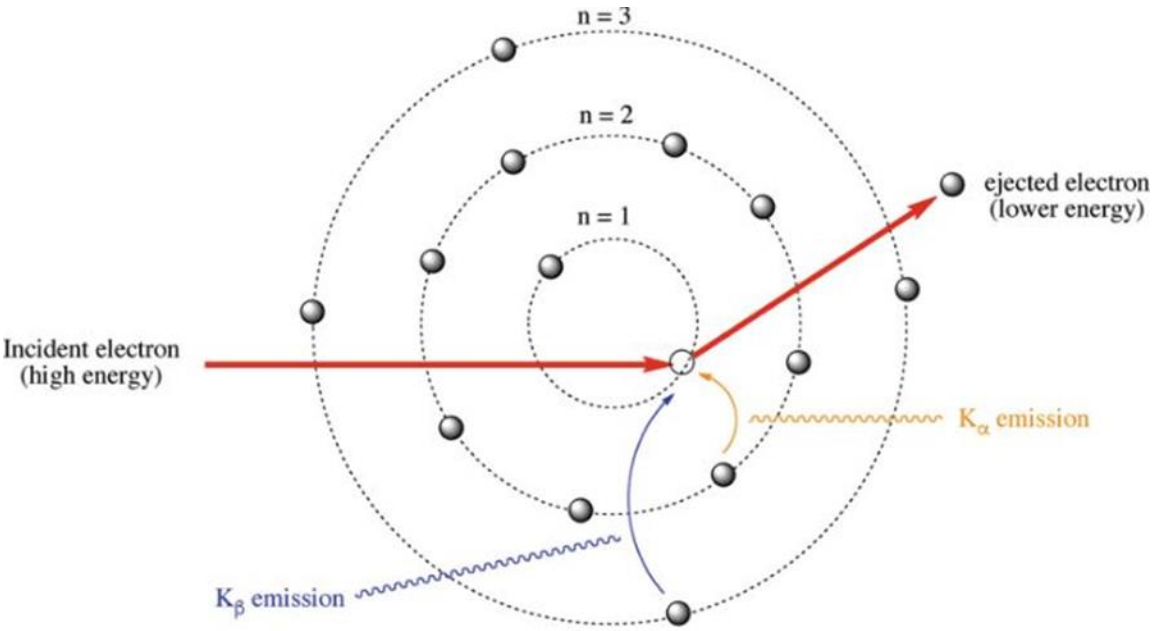

Figure 2-12: schematic of photoelectron process where there is a high energy source knocking off an electron from an inner shell of an atom, where the electron get ejected from the atom[76].

This technique relies on the photoelectron effect, which was discovered by Einstein who won the Nobel Prize for his discovery in 1921. Figure 2-12 illustrates the photoelectron effect where the high energy incoming X-ray photon hits an inner shell electron with high enough energy to move to the fermi level (Figure 2-13). This energy difference from its initial state is known as binding energy. Afterwards, if the electron has even higher energy, then the electron can move from fermi level to vacuum, overcoming an energy known as work function. Any energy left will be converted to kinetic energy[76].

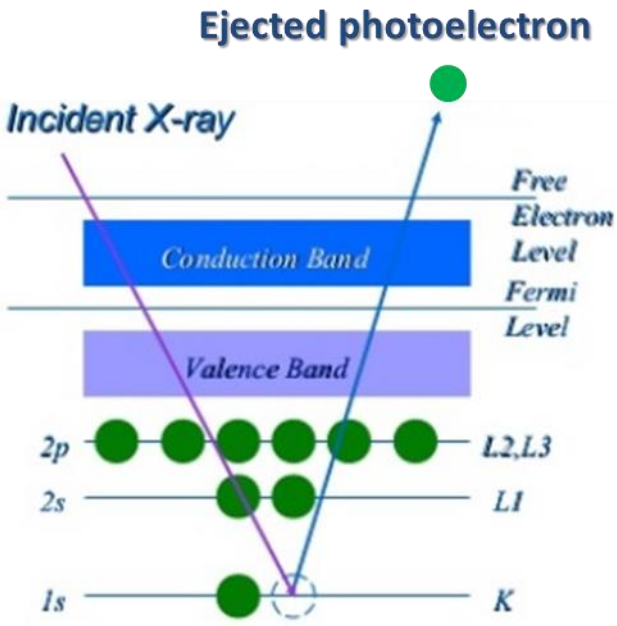

Figure 2-13: simple illustration of electrons energy levels during the photoelectric process (Leibniz Institute for Solid State and Materials Research Dresden) (modified image). ref[77].

2.3 Methods:

2.3.1 MXene synthesis and fabrication of MXene membranes:

The overall schematic of the fabrication of free standing $Ti_3C_2T_x$ membrane is shown in (Figure 2-14).

2.3.1.1 Etching of Al-element from MnAXn-1 phase:

The chemical removal of the atomic aluminum layers from the M_nAX_{n-1} (Al from Ti_3AlC_2) phase was performed according to the following procedure. Generally, the solution was prepared by adding 800 mg LiF to 10 mL of 9 M HCL and stirred continuously for 5 minutes. Then, 500 mg of Ti_3AlC_2 powder was added over the course of 10 mins to avoid the resultant exothermic temperature from the reaction. Finally, the solution was stirred for 24 hours under a magnetic stirrer[15].

2.3.1.2 Washing and freeze drying:

The resulted mixture was washed using centrifuge (3500 rpm for 35 min per each cycle) for a total of 5 cycles with deionized water. Moreover, each time the supernatant was decanted to get rid of the salts, de-ionized water was added, and the solution was mixed using the vortex in order to free the trapped salts in the MXene slurry. The pH of the solution reached between 5-6 at the end of the washing steps. Afterwards, 25 ml of de-ionized water was added to the MXene slurry and mixed vigorously using the vortex. To characterize the ML-MXene using XRD; The solution was frozen and inserted inside the freeze drier to get a powder of ML-$Ti_3C_2T_x$.

2.3.1.3 Delamination process:

4 mg of the produced ML-$Ti_3C_2T_x$ powder was added to 25 ml of de-ionized water. The mixture was then added in a water bath sonication and sonicated for an hour. This process allows the ML-MXene to be delaminated by breaking the weak Van der Waal forces between the Al and the ML-Ti_3C_2 producing DL- $Ti_3C_2T_x$.

2.3.1.4 Fabrication of free-standing MXene membrane:

In this step, the sonicated MXene was deposited onto a PVD membrane. This was done by the vacuum-assisted filtration system (VAF). The membrane was left to dry in the oven at 40°C for 1 hour for the ease of peeling off the MXene membrane.

Graphene Oxide (GO) membrane was synthesized *via* VAF process using a commercial GO suspension.

2.3.2 Fabrication of intercalated MXene membranes:

The salts were prepared by making a 1 M of NaCl, KCl_2, and $AlCl_3$ in a 20ul of de-ionized water. Then, the mixture was shaken vigorously to get a transparent solution. Three free-standing membranes were soaked in each salt for 24 hours to allow the intercalation of salts in between the MXene layers.

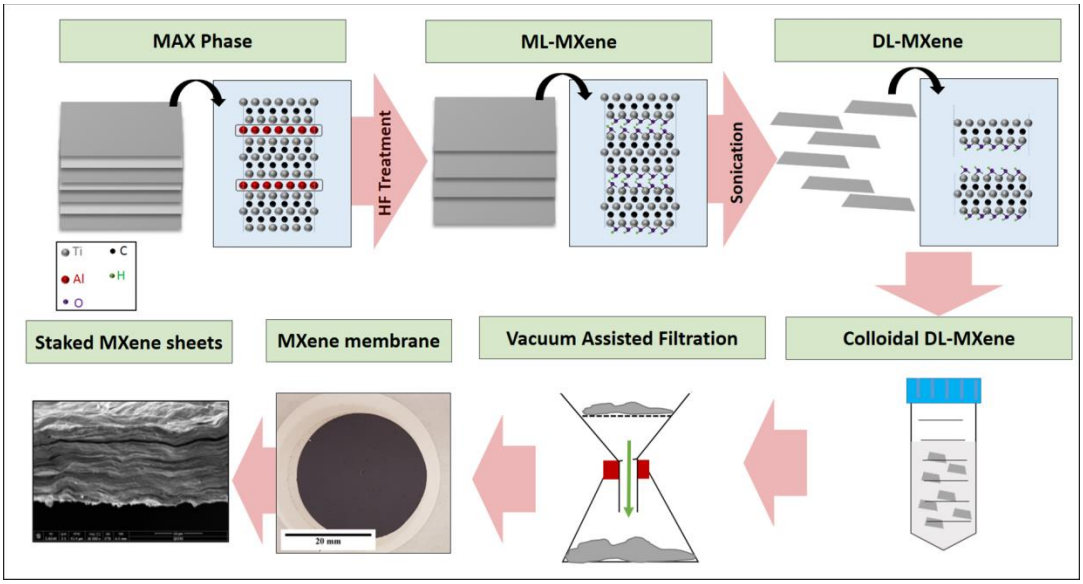

Figure 2-14: the schematic diagram of the synthesis of $Ti_3C_2T_x$ membranes.

2.4 Characterization:

2.4.1 X-ray Diffraction with Dielectric Thermal Analysis (XRD-DSC):

XRD experimental used were 40KV and 20 mA with an intensity range from 3 to 60 of 2Ɵ with 0.02-degree step and 3deg/minute speed for each temperature used. The temperature started from room temperature and then 50°C with an increment of 50 until reaching 300°C, 2-3 deg. C/min ramp rate and 1 hr. of holding time to allow some time for the sample to stabilize. The DSC was used only for temperature, and the DSC reading was disregarded as there is no phase transformation happens to the material used in this work at the previously stated tempratures[70].

2.4.2 SEM characterization and in-situ ESEM:

In this study, the measurement conditions were fixed using a fixed focus and line measurement conditions as our reference. For the relative humidity experiment, two-cycles of RH were used between 30% until 100% RH with 10%RH step size with a one-minute hold time. On the other hand, heating was performed starting from 50°C to 300°C with 50° step size and a one-minute hold time between each step.

2.4.4 Contact angle:

Drop shape analyzer mode was used to test the contact angle for all the membranes in this study. The system uses a syringe to drop a water droplet on the surface of the membrane; then, a camera is used to take a picture of the droplet and measure the contact angle.

Chapter 3 : Results and discussion

3.1 Synthesis and characterization of MXene:

The synthesis of $Ti_3C_2T_x$ (MXene) from Ti_3AlC_2 (MAX) phase was achieved by the chemical etching of the Al element using a mixture of HCL/LiF [78]. After 24 hours under constant stirring and a temperature of 40°C, we obtained what is conventionally known as ML MXene (ML-MXene) with some byproducts from the reaction in the form of salts that needed to be removed. Centrifugation was used for the removal of these byproducts performing 5 cycles with 3500 rpm until we reached 4-5 pH. Afterwards, the produced sample was bath sonicated for 1 hour before being freeze dried to get the delaminated MXene.

SEM image (Figure 3-1.a) showed a conventional structure for DL- $Ti_3C_2T_x$ sheets of a wrinkle and flat sheet like structure. On the other hand, TEM image (Figure 3-1.b) of DL-$Ti_3C_2T_x$ sheets also revealed a flat structure with single and sometimes few-layered MXene flakes with very few defects. The result from the MILD in-situ HF synthesis yields less defective MXene, unlike the HF route[26].

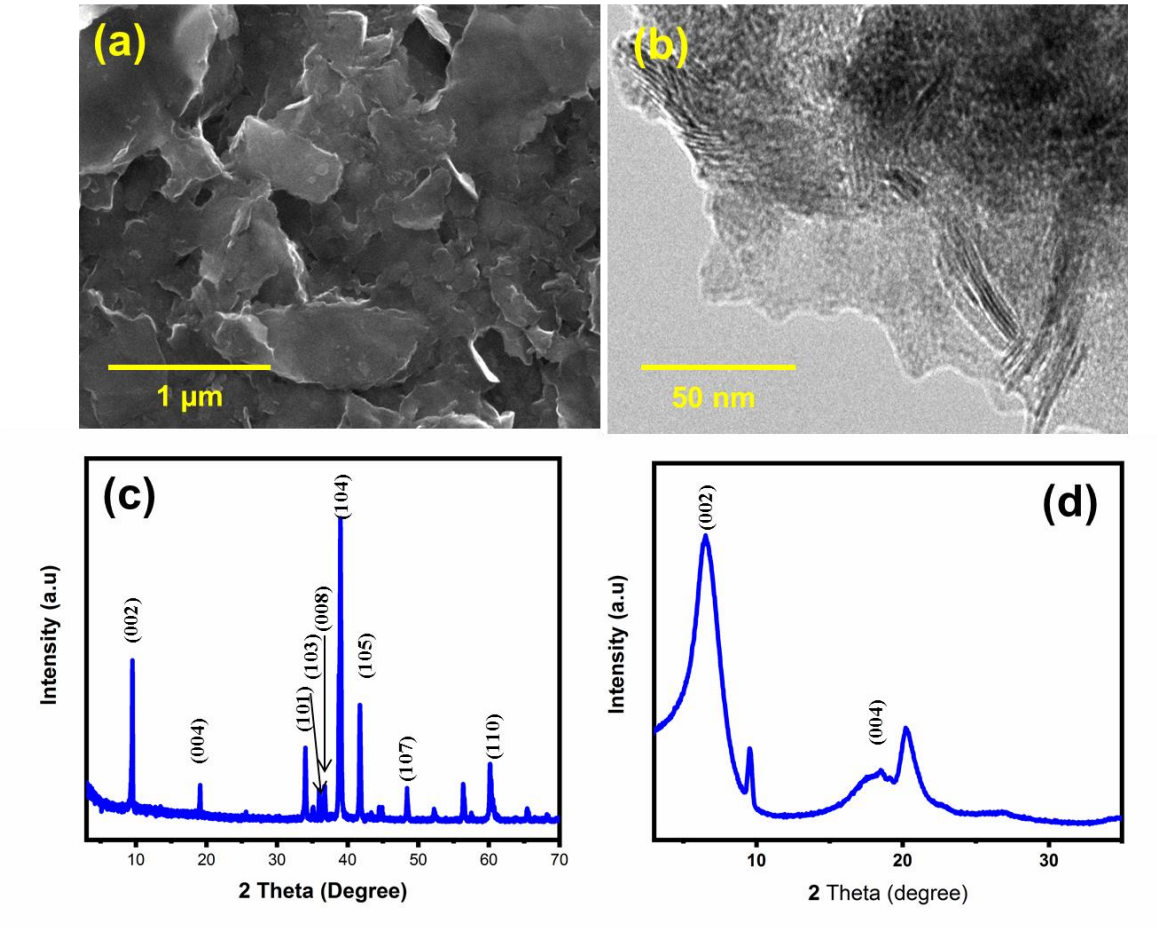

Figure 3-1: (a) SEM image shows the morphology of DL- $Ti_3C_2T_x$, as for (b) TEM image of DL- $Ti_3C_2T_x$. on the second panel, XRD patter for both (c) Ti_3AlC_2 (MAX phase as powder), and (d) DL- $Ti_3C_2T_x$ (MXene phase as powder).

XRD pattern in (figure 3-1 .c) shows the Ti_3AlC_2 phase with different peaks that represents a typical MAX phase peaks of hexagonal structure. Those peaks are calculated with Bragg's law from the two theta values, which are (002), (004), (101), (103), (008), (104), (105), (107), and (110). After the synthesis of the MAX phase, the (002) peak has shifted to the right in the compared to Ti_3AlC_2 with a broadening effect confirming the DL- $Ti_3C_2T_x$ structure (figure 3-1 .d). There is a small peak on the right of (002) peak which is a trace amount of the MAX phase. All the intense peaks of the Ti_3AlC_2 phase has disappeared leaving a 2D hexagonal peaks only which belong to the DL- $Ti_3C_2T_x$.

The MXene XRD pattern shows a typical hexagonal structure for peaks higher than 10° of 2θ [79]. Two consecutive peaks showed as one peak at a 2θ value of less than 10°, which suggest a Li^+ cations intercalation along with water molecules[80].

Furthermore, the XRD patterns of DL- $Ti_3C_2T_x$ peaks show the disappearance of the most intense peak of aluminum at 2θ = ~39°, which confirms the successful etching and removal of aluminum layers from the parent MAX phase. Moreover, it can be seen that peak (002) has shifted to a lower angle of 2θ = ~7° with broadening behavior, which is a typical signature of the successful formation of DL- $Ti_3C_2T_x$. In addition, other characteristic peaks were observed like (004), which has been shifted to the left side of the XRD graph[81].

There were some difficulties at the beginning of the synthesis of MXene; SEM with EDS mapping was performed to investigate the results of the synthesized DL-MXene at the start of this work. The results showed some fluoride structures along with Alumina particles as can be seen in (Figure 3-5). These particles are undesirable as they will affect the purity of the resulted MXene. These impurities possibly result from the washing process[26], which, consequently, affects the membrane fabrication process as the free stacked structure of MXene membrane was not achieved. Eliminating the undesired materials required using a higher speed by the centrifugation system. As such, 3500 rpm was used for 3 cycles before increasing to 10,000 rpm for another 2 cycles. When the pH was measured, an improvement from 4 pH to 6 pH was observed. These improvements allowed for the successful production of a nicely layered MXene membrane structure.

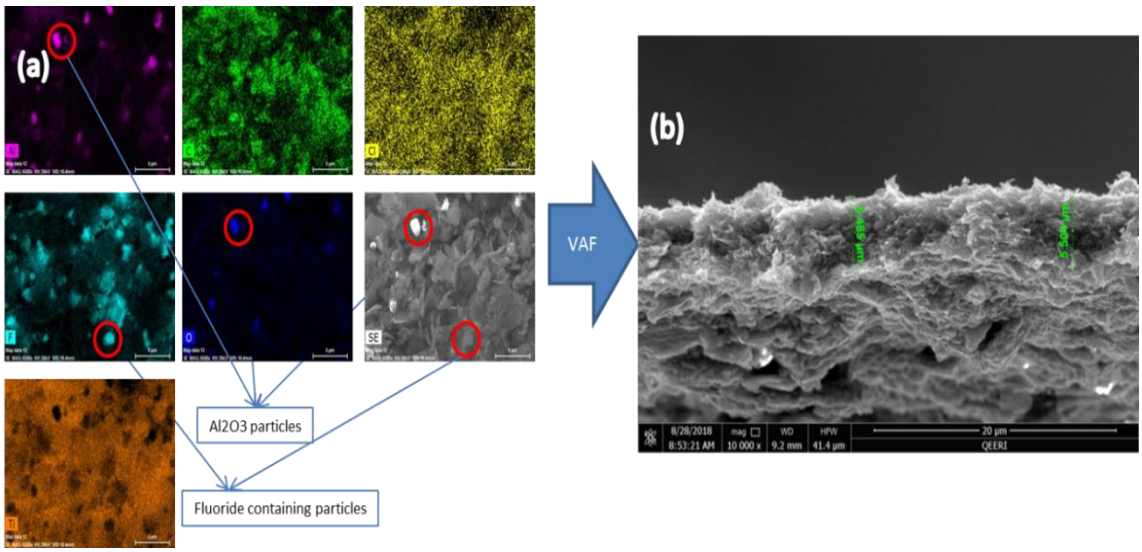

Figure 3-2: To the left of the arrow (a) are the EDS map showing the location of Al_2O_3 particles and Fluoride containing particles. To the right of the arrow (b) is an SEM image of cross section for the delaminated MXene where there is no apparent layered structure.

3.2 MXene membrane synthesis, fabrication and characterization:

MXene membrane was fabricated from MXene solution using VAF setup on a polymeric substrate then peeled off for further investigation.

Upon examining the cross-section of the prepared $Ti_3C_2T_x$ membrane, tightly restacked MXene sheets were observed forming nicely packed layers (Figure 3-3.a) with a flexible property. The XRD pattern of this membrane showed two peaks next to each other at (002) that correspond to water intercalation and lithium cation intercalation, which will be discussed more thoroughly in the *in-situ* XRD work in later sections.

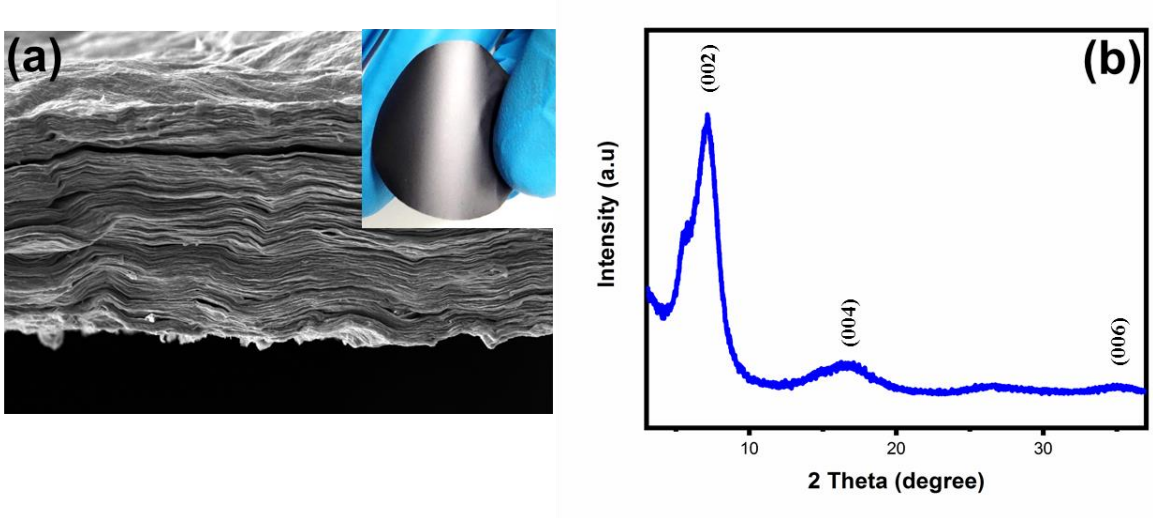

Figure 3-3: (a) SEM Cross-sectional image of DL- $Ti_3C_2T_x$ membrane (inset: an optical image of the flexible MXene membrane), and the correspondent (b) XRD pattern.

3.3 Ion intercalation process and the fabrication of MXene intercalated membranes:

Here, salt of one molar has been added to the pre-prepared MXene solution. These salts (NaCl, $CaCl_2$, and $AlCl_3$) were chosen with Cl as the common anion for investigating the effect of the cations only.

TEM analysis was performed to examine the sheet structure for all of the delaminated intercalated MXene (Figure 3-4). The effect of hydration enthalpy for each cation can be seen in the images. The sodium intercalated case reveals that the sheets are relaxed with no rolling effect unlike in the Ca-MXene case. On the other hand, Al-MXene has several sheets on top of each other and an agglomerated-like structure. These observations are related to the charge of each cation where it can pull the sheets together stronger, especially when the charge of the cations is higher[54,67].

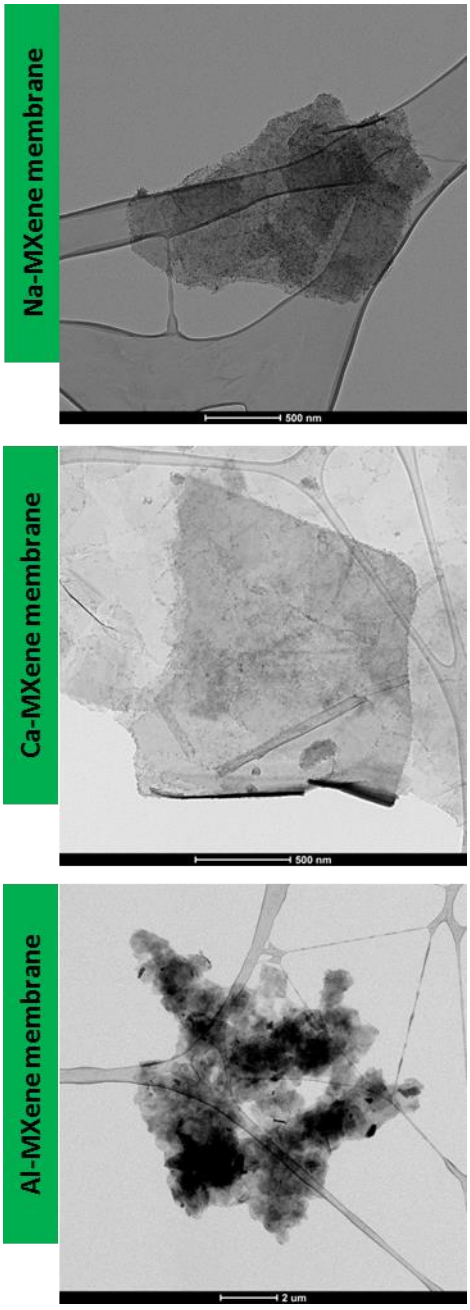

Figure 3-4: TEM images for the intercalated MXene.

XRD was used to understand the effect of the aforementioned intercalated cations on the interlayer spacing of $Ti_3C_2T_x$ membranes. (Figure 3-5) shows the XRD patterns for each intercalated cation membrane where the (002) peaks were shifted to lower 2θ angles for each of these membranes. The results suggest an expansion in the interlayer spacing of $Ti_3C_2T_x$ membranes. The interlayer distance values were to ~4.56, ~4.99, ~5.44, and ~5.84 Å for $Ti_3C_2T_x$, Na- $Ti_3C_2T_x$, Ca- $Ti_3C_2T_x$, and Al- $Ti_3C_2T_x$ membranes, respectively. It was observed that the interlayer spacing increased with increasing the cation size. TEM images were in agreement with XRD data as in the insert image in (Figure 3-5), where 4.56Å, 4.99Å, 5.44Å, and 5.84Å were measured for $Ti_3C_2T_x$, Na-$Ti_3C_2T_x$, Ca- $Ti_3C_2T_x$, and Al- $Ti_3C_2T_x$ as delaminated in solution.

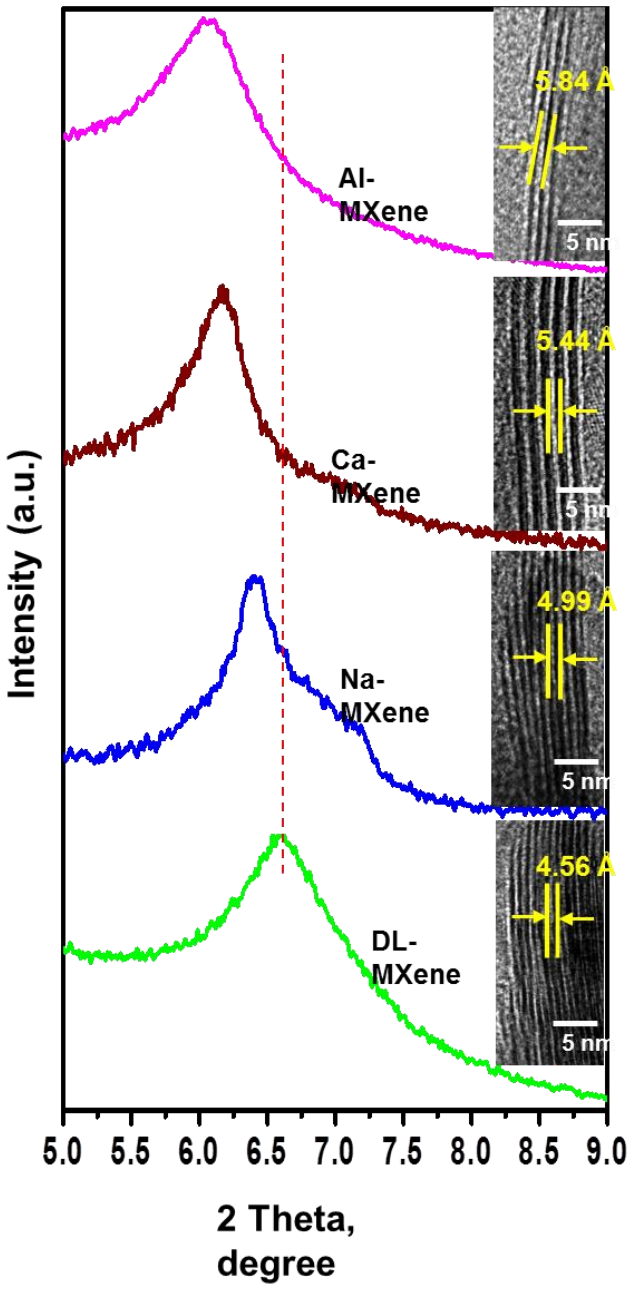

Figure 3-5: XRD patterns combined with TEM images for DL- $Ti_3C_2T_x$ upon intercalation of Na^+, Ca^{2+}, and Al^{3+}.

SEM/EDS were performed to investigate the intercalation of cations inside the MXene sheets that represent Na^{+} intercalated MXene membrane (Na-MXene), Ca^{2+} intercalated MXene (Ca-MXene), and Al^{3+} intercalated MXene membrane (Al-MXene), respectively (Figure 3-6). Moreover, the color coding for each element allows for easy identification of the location of each element. There is a dense color for each element on top of the membrane; this could be related to the ease of adsorption on top of the membrane[26,67].

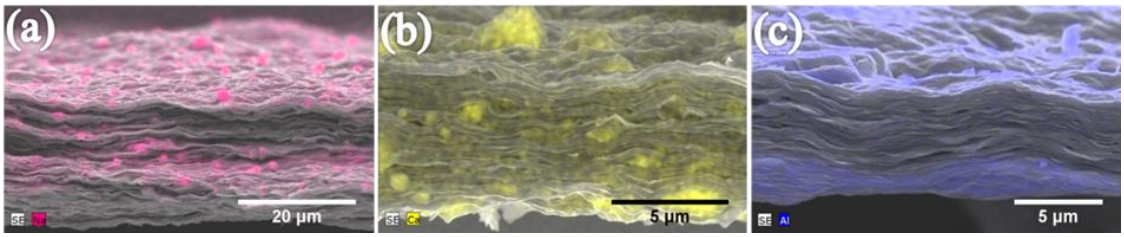

Figure 3-6: EDS mapping for a) Na- $Ti_3C_2T_x$, b) Ca- $Ti_3C_2T_x$, and c) Al- $Ti_3C_2T_x$ superimposed on SEM images with different color coding.

3.3.1XPS Analysis of the fabricated MXene membranes to investigate the distribution of intercalated cations between MXene layers:

XPS analysis was performed to prove the intercalation of different cations in between the MXene membrane and to have a better understanding of the various elemental states for the different MXene membranes.

The XPS spectra of the four different cation intercalated samples were compared in (Figure 3-7), where Ti2p, O1s, C1s, and F1s spectra are listed. Spectra are shifted in intensity to reach the same background level to allow for better comparison without any normalization. As indicated in the left panel, the raw samples before sputtering show considerable variation in the T2p, O1s, and C1s spectra due to the different species of the surface termination groups. It is proved by imposing a sufficient Ar+ etching deep into the samples. The subsequent spectra are observed to be identical in both the components and intensity. This reflects well the high stability in the $Ti_3C_2T_x$ sheets, and the components are not affected by the type of intercalated ion or by different solvents used during the preparation. Thus, we briefly give the deconvolution of the main components inside the MXene sheets without surface termination groups. The results are listed in Table 3-1.

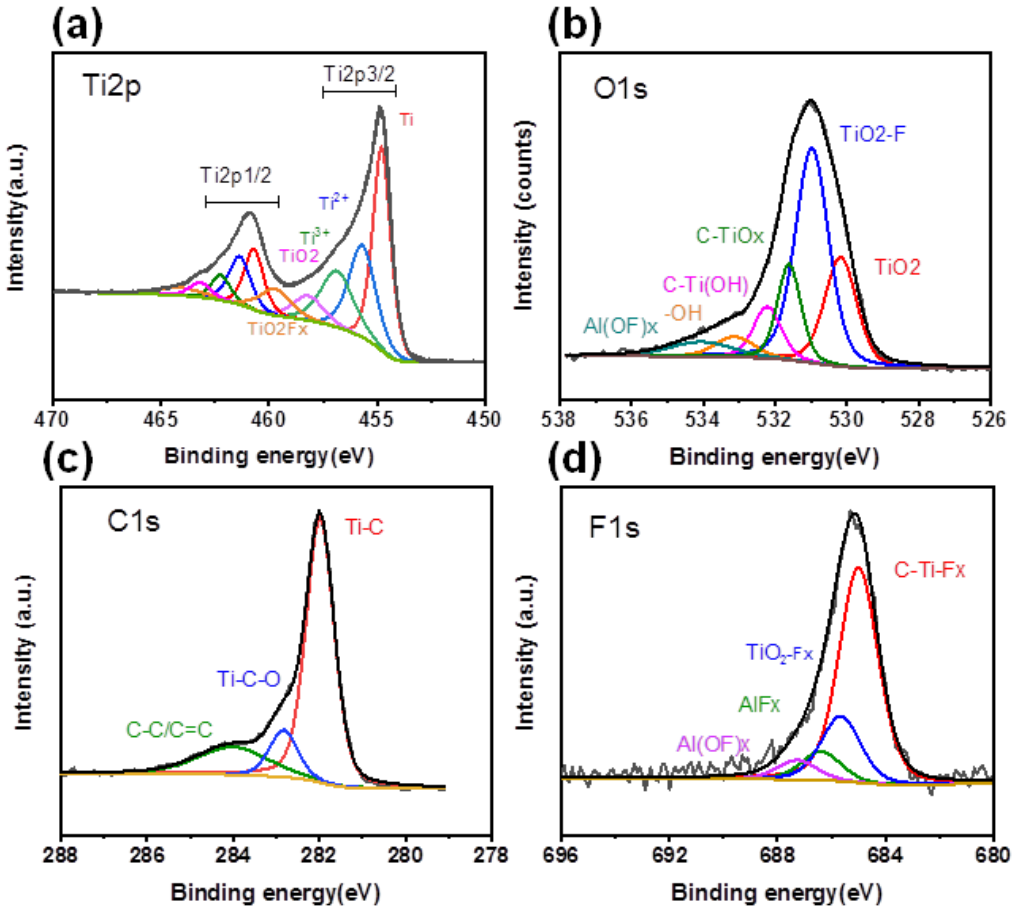

Figure 3-7: The figure shows the fitting of the typical XPS Ti2p, C1s, O1s, and F1s spectra for the Samples after etching until a clean sheet is obtained.

Table 3-1: the fitting parameter for the Ti2p, C1s, O1s, and F1s core levels.

Name	Peak (BE)	Height (CPS)	Height Ratio	Area (CPS.eV)	Area Ratio	FWHM fit parameter (eV)
Ti2p						
Ti2p3/2 Ti	454.71	69376.87	1	72592.34	1	0.87
Ti2p3/2 Ti2+	455.33	46539.66	0.67	71834.62	0.99	1.29
Ti2p3/2 Ti3+	456.4	28421.77	0.41	51482.85	0.71	1.51
Ti2p3/2 TiO2Fx	457.58	14736.84	0.21	26365.7	0.36	1.49
Ti2p3/2 TiO2	458.95	8717.56	0.13	17143.85	0.24	1.64
Ti2p1/2	460.65	22408.32	0.32	37263.25	0.51	1.38
Ti2p1/2	460.99	11287.77	0.16	18583.73	0.26	1.37
Ti2p1/2	462.26	9556.32	0.14	20964.78	0.29	1.83
Ti2p1/2	463.52	3445.42	0.05	9204.25	0.13	2.24
Ti2p1/2	461.51	5939.93	0.09	11865.03	0.16	1.67
O1s						
O1s TiO2	530.17	17441.47	0.51	22011.94	0.49	1.06
O1s TiO2-F	530.97	34212.11	1	44892.15	1	1.1
O1s C-TiOx	531.61	15294.56	0.45	14217.98	0.32	0.77
O1s C-Ti(OH)	532.21	8220.37	0.24	9015.05	0.2	0.91
O1s H2O	533.12	3275.28	0.1	5050.42	0.11	1.29
O1s Al(OF)	534.05	2357.72	0.07	5855.7	0.13	2.1
C1s						
C1s Ti-C	281.98	24523.13	1	22127.92	1	0.78
C1s C-Ti-O	283.98	2693.86	0.11	6377.61	0.29	2.01
C1s C-C/C=C	282.84	4396.39	0.18	3975.63	0.18	0.78
F1s						
F1s TiO2Fx	684.99	10509.75	1	21438.1	1	1.72
F1s C-Ti-Fx	685.65	3181.2	0.3	6524.01	0.3	1.72
F1s AlFx	686.38	1408.19	0.13	2876.84	0.13	1.72
F1s Al(OF)x	687.27	949.66	0.09	1949.87	0.09	1.72

As seen from (Figure 3-7), the Ti2p gives spin split components with Ti2p3/2 and Ti2p1/2 locating at 455eV and 462eV. The Ti2p3/2 can be further de-convoluted into five structures relating to metallic Ti, Ti^{2+}, Ti^{3+} and Ti^{4+}, respectively. A small amount of TiO_2F_x is also given at 457.6eV. Due to the d to f electron interaction in transition metals, the Ti2p1/2 is a bit permutated; in the O1s case, the prominent peak relates to the TiO2-F at 530.9eV, while the TiO_2 and C-TiO_x locates at 530eV and 531.6eV. The C1s shows the main Ti-C structure at 282eV, and the Ti-C-O structure forms the shoulder at a higher binding energy of 284eV. The F1s gives 4 components corresponding to two main attachments of F to TiO2(685eV), Ti-C(685.5eV) and a small quantity of AlFx and Al(OF)x at 686eV and 687eV, respectively.

Binding energy positions of different components have been widely reported, and our results proved to be per their values[67], which suggests 1) Ti2p mainly gives the Ti-C structure with the different Ti^{x+} components, while 19% of the Ti should be assigned to the TiO_2 components; 2) several surface functional groups are attached to the sheet surface including the -OH, the -O- and fluoride (-F) species. Some C=C related species seem to exist as well.

The evaluation of the cation intercalation was done by looking at the corresponding Na1s Ca2p and Al2p core levels; the deconvolution is illustrated in (Figure 3-8) (see also Figure 3-7). The deconvolution of Ti2p, C1s, O1s and F1s and the corresponding parameters are listed in Table 3-2 and Table 3-1. Based on this estimation, the global atomic percentage of the samples are given, and a summary of their atomic concentration is listed in Table 3-3 including both the before and after cases of the Ar^+ etching process. The values for Ca^{2+} and Al^{3+} are obtained by calculating the areas from the high-

resolution spectra of each element after a proper Shirley background subtraction. The Na^+ case is obtained by a proper fitting procedure as the Na1s signal is partially overlapping with the Ti-O_2 and Ti-C LMM Auger features as seen in (Figure 3-8). Quantitatively, a sufficient etching process resulted in cations values of 2.9%, 0.74%, and 0.96%. By looking at the time resolution of the etching process in (Figure 3-9), we should notice the cation signals mainly attenuate during the initial 40s of the etching process and become constant during subsequent cycles. This observation suggests that the number of intercalated cations may be the same between the membrane's sheets. The efficiency of the etching process is confirmed by the observation of the same features of Ti2p, C1s and O1s as described in (Figure 3-10).

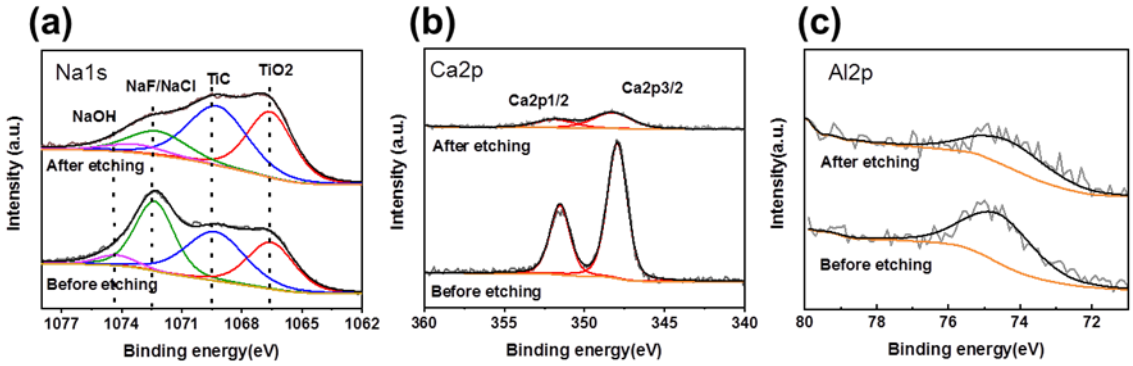

Figure 3-8: Prove of the interaction of the corresponding ions with XPS measurement. Deconvolution of the (a) Na1s, (b) Ca2p and (c) Al2p spectra are given after a proper Shirley background subtraction.

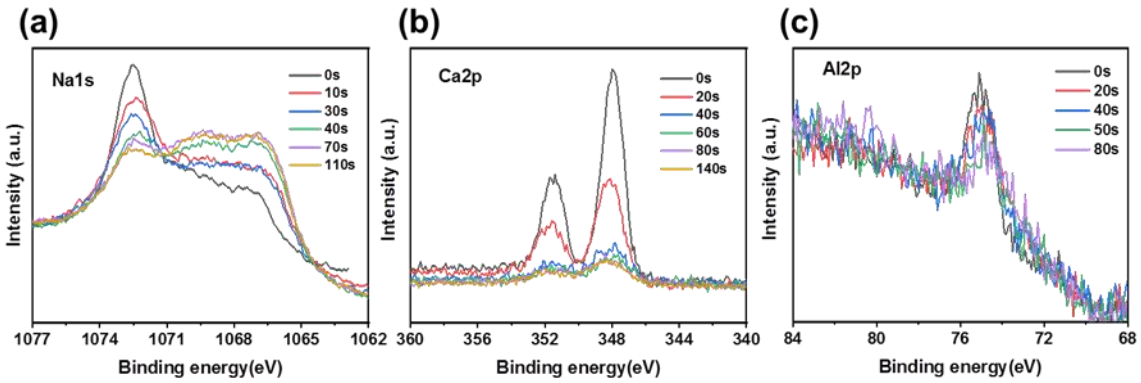

Figure 3-9: The XPS spectra of intercalated ion N1s, Ca2p, and Al2p as function of etching time.

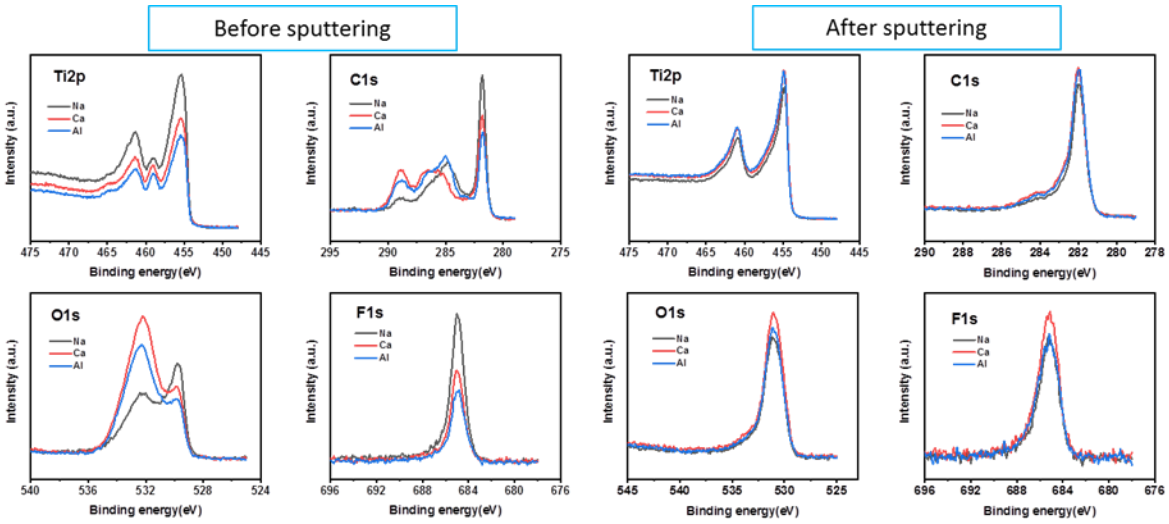

Figure 3-10: comparison of the Ti2p, C1s, O1s and F1s core level XPS spectra for the pre-sputtering samples (left panel) and the after-sputtering samples(right panel). Gray, red and blue line are used to present the Na, Ca and Al intercalation.

Table 3-2: The fitting parameter of Na1s, Ca2p, and Al2p before and after the etching process.

Name	Peak (BE)	Height (CPS)	Height Ratio	Area (CPS.eV)	Area Ratio	FWHM fit param (eV)
Na1s						
Before etching						
TiO2 LMM	1066.25	5895.22	0.39	17449.46	0.56	2.56
TiC LMM	1069.16	7722.76	0.51	31204.76	1	3.5
Na1s NaF/NaCl	1071.63	15211.29	1	31154.83	1	1.73
Na1s NaOH	1073.26	1792.38	0.12	3661.58	0.12	1.73
After etching						
TiO2 LMM	1066.58	12137.22	1	37590.13	0.85	2.67
TiC LMM	1069.22	10949.82	0.9	44244.11	1	3.5
Na1s NaF/NaCl	1072.23	4454.75	0.37	17871.29	0.4	3.48
Na1s NaOH	1073.28	1566.25	0.13	6259.48	0.14	3.48
Ca2p						
Before etching						
Ca2p3/2	347.95	10443.9	1	18131.19	1	1.45
Ca2p1/2	351.52	5362.24	0.51	9312.98	0.51	1.45
After etching						
Ca2p3/2	348.27	1231.86	1	4020.04	1	2.78
Ca2p1/2	351.87	632.48	0.51	2063.49	0.51	2.78
Al2p						
Before etching						
Al2p AlOx/AlOH	74.94	471.68	1	892.24	1	1.59
After etching						
Al2p AlOx/AlOH	74.45	328.17	1	815.13	1	2.1

Table 3-3: Calculation of the atomic percentage based on the high-resolution XPS spectra.

	Ti	C	O	F	Cl	Ca	Na	Li	Al
S1Al before	17.16	39.79	33.16	5.48	1.81	--	--	--	1.37
S1Al after	39.3	23.68	24.83	6.5	1.5	--	--	--	0.96
S3Na before	25.93	34.93	24.07	9.62	2.27	--	3.18	--	--
S3Na after	40.14	23.61	23.42	8.19	1.74	--	2.9	--	--
S4Li before	18.57	30.96	35.64	5.49	0.81	--	--	7.35	--
S4Li after	34.43	14.02	35.53	6.09	0.6	--	--	6.13	--
S5Ca before	17.85	35.57	35.53	5.61	1.72	2.46	--	--	--
S5Ca after	39.38	23.77	25.57	6.31	1.55	0.74	--	--	--

3.3.2Contact angle characterization of fabricated membranes:

Na-MXene has a lower contact angle than Ca-MXene and Al-MXene membranes (Figure 3-11). This phenomenon is related to the hydration enthalpy, and is reinforced by what was seen in the *in-situ* XRD and *in-situ* SEM. Moreover, MXene has a lower contact angle than GO, which makes MXene more hydrophilic than GO membrane (Table 3-4). It can be seen that all the intercalated MXene has a lower contact angle than GO membrane.

Intercalated cations between MXene sheets improve structural homogeneity, which allows a smooth surface of the MXene membranes and water stability between its sheets[54]. This makes the intercalated MXene membrane smoother, which enhances the hydrophilicity of the membrane, unlike GO membrane that has many air gaps (Figure 4-16 b) causing a reduction in the hydrophilicity of the membrane.

As the Al cation has the largest size from Na and Ca, it creates micro air bubbles between the MXene sheets making the membrane less hydrophilic than Na-MXene, Ca-MXene, and MXene membrane itself. This observation means that hydration radius affects the hydrophilicity of the membrane.

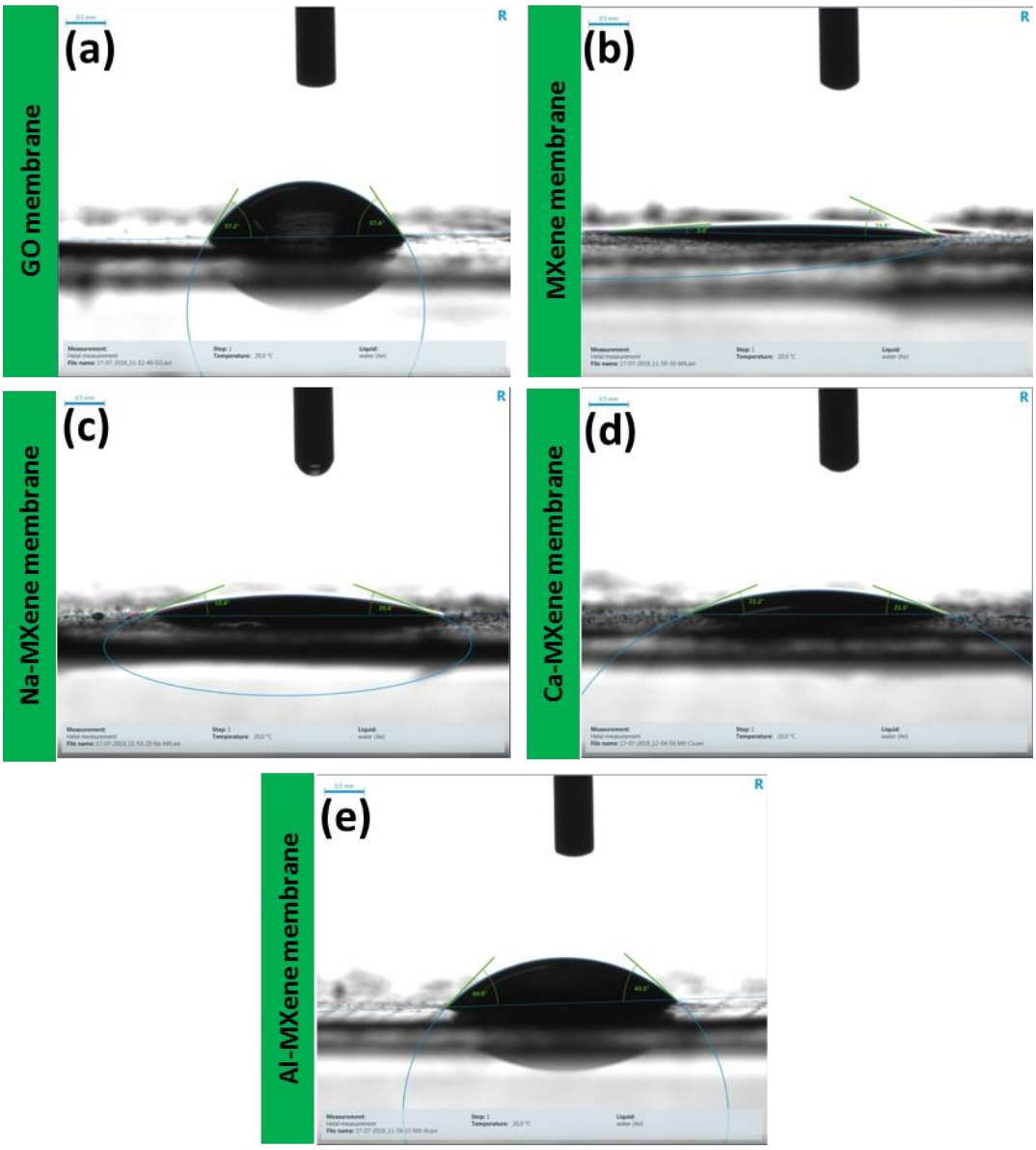

Figure 3-11: contact angle of, a)GO, b)MXene, c)Na-MXene, d)Ca-MXene, e)Al-MXene.

Table 3-4: The table is for the contact angle values for the fabricated membranes.

Membrane name	Contact angle (θ)
GO	57.2
$Ti_3C_2T_x$	5
Na-$Ti_3C_2T_x$	19.8
Ca-$Ti_3C_2T_x$	22.2
Al-$Ti_3C_2T_x$	44

3.4 i*n-situ* investigation of fabricated membranes under different relative humidity and temperatures:

3.4.1 in-situ XRD analysis for the fabricated membranes:

X-Ray Diffraction (XRD) from Bruker with a model name Smartlab, Tokyo, Japan, was used for the XRD analysis in this study (Cu Kα radiation as a source of radiation). All of the samples were scanned at a step size of 0.02 deg with a speed of 3deg/min. The DSC attachment of the previously mentioned XRD was used for in-situ XRD for varying temperatures with no humidity control. The measurement was done at 25, 50, 100, 150, 200, 250, 300 °C with a 1-hour pause on each temperature and 3 deg. C/min ramp rate for stabilization.

As mentioned previously in the literature review, the cations can intercalate the MXene c-lattice due to the electrostatic force between the positive ions and the negatively charged MXene sheets. We intercalate our MXene with three main cations from Na^{+}, Ca^{2+}, and Al^{3+} cations, where they have a distinct hydration energy[82].

(Figure 3-12) shows the in-situ XRD where the temperature has increased from 50 °C to 300°C for MXene, Na-MXene, Ca-MXene, and Al-MXene. (Figure 3-13) presents the different values for the d-space in relation with temperature for the studied membranes of this work.

It is interesting to compare the effect of temperature on the interspace of MXene membrane with another 2D membrane material. GO membrane was chosen to be compared with the MXene membrane in this study. The (002) peak shifts in MXene membrane was from 7.125° to 8.11° 2θ (Table 3-5) from 25° C to 300°C, respectively,

which corresponds to 1.5 Å shift. On the other hand, the (002) peak of GO membrane that started at 10.76° when at room temperature has disappeared at 250°C suggesting a complete collapse of GO membrane (Table 3-5). These results suggest that MXene membranes have a better stability under high temperature than GO membranes.

Cations can affect the interspace of MXene materials when intercalated[34,54,65]. The membranes of the three intercalated cations showed different effects on the d-space of the MXene membrane when the temperature was applied. Al- $Ti_3C_2T_x$ membrane showed the highest d-space decrease of about 2.29Å compared to other cation intercalated membranes. The d-space decrease could be related to the hydration radius and hydration enthalpy differences between these cations (Table 3-6)[53,82]. As a result, more water can be intercalated to surround the Al cations under normal humidities. It can be easily observed from (Figure 3-13) that Al- $Ti_3C_2T_x$ membrane had the highest d-space value at 50°C of a calculated value of 13Å (Table 3-5). These previous values were higher than sodium and calcium intercalated MXene membranes, where Na- $Ti_3C_2T_x$ membrane had ~12.55Å d-space and Ca- $Ti_3C_2T_x$ membranes had a value of ~12.51Å. Trivalent cations or higher may have more effect on the interspace of MXene membranes under high temperatures than lower charged cations.

(Figure 3-12. b) showed that sodium intercalated MXene membrane had a sharp peak compared to the other Ca- $Ti_3C_2T_x$ and Al- $Ti_3C_2T_x$ membranes. This observation means that Na- $Ti_3C_2T_x$ membrane had the most homogenous structure among the other intercalated membranes; the mono-valance cations could increase the homogeneity of MXene membranes when compared to multi-valence cations [19,54,83].

Another observation presented in (Figure 3-13) was that d-space decrease rate between

50 °C and 100 °C was high. This could be related to the release of water to water bonds that are intercalated between the membranes [21,69]. Furthermore, MXene membrane in (Figure 3-12.a) has less d-space decrease when compared with sodium intercalated MXene membranes. This may be related to the intercalated lithium cations from the synthesis process used in this study, where lithium cations have a higher hydration energy than that of sodium cations[82]. In observing the peak intensities when increasing temperature in (Figure 3-12), it was clear that intensity decreases with increased temperature. This may suggest the homogeneity of the membranes is decreased at high temperatures. Furthermore, the peak shifts to the right in the XRD pattern for membranes at a continuous pace, which is in direct agreement with a recent study that observed a heterogeneous hydration process[65]. However, an earlier study suggested otherwise when in-situ XRD with relative humidity was applied [19]. The difference between these results could be attributed to the difference in the synthesis of MXene post-treatment and possibly the uneven distribution of water layers/molecules[65]. Additionally, the temperature may have a different effect when compared to relative humidity on the membranes. For example, the water-water bond breaks easily when increasing the temperature to 100 °C[69], and the water-sheets surface bond breaks at even higher temperatures. An interesting observation noted in (Figure 3-13) is that all of the membranes have about 10.5 Å d-space at 300 °C.

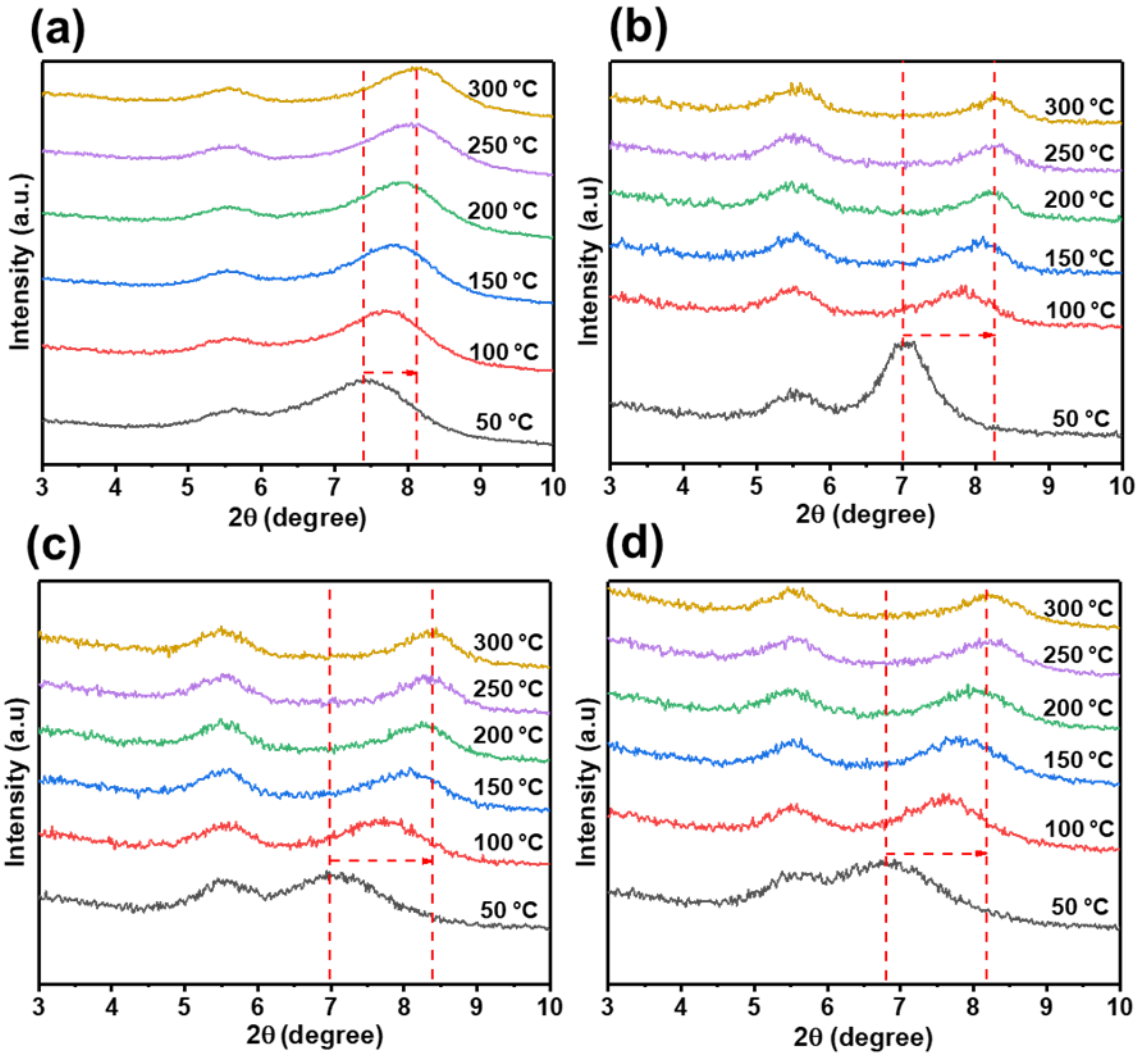

Figure 3-12: XRD patterns of in-situ XRD where temperature has been varied from 50°C till 300°C for as prepared (a) $Ti_3C_2T_x$, (b) Na- $Ti_3C_2T_x$, (c) Ca- $Ti_3C_2T_x$, and (d) Al-$Ti_3C_2T_x$ membranes.

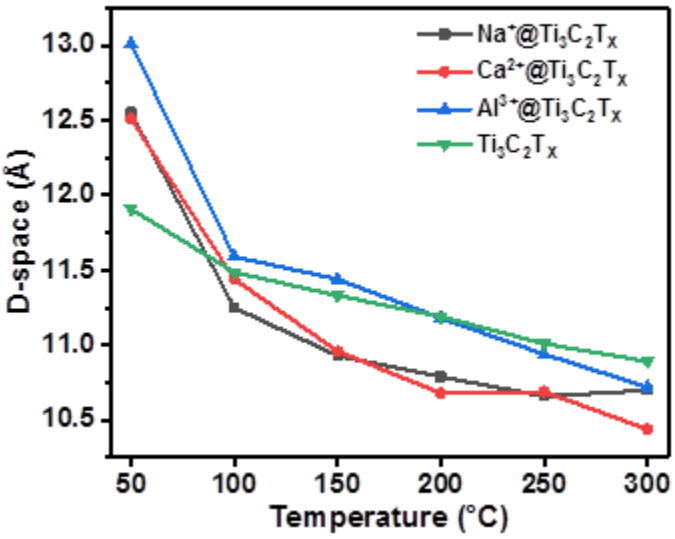

Figure 3-13: D-spacing changes as function of temperature from XRD experiment for different MXene membranes: The water loss is at highest value at 100 °C. The d-spacing values at 300 °C are about 10.7Å. The highest d-spacing decrease was between 50-100 °C.

Table 3-5: The 2θ values and their correspondent calculated d-space at different temperature for the membranes of this study.

Temperature-re (°C)	GO membrane		$Ti_3C_2T_x$ membrane		Na-$Ti_3C_2T_x$membrane		Ca-$Ti_3C_2T_x$membrane		Al-$Ti_3C_2T_x$membrane	
	2Θ value	D-space (Å)	2Θ value	D-space (Å)	2Θ value	D-space (Å)	2Θ value	D-space (Å)	2Θ value	D-space (Å)
25	10.756	8.22	7.126	12.39	6.531	13.52	--	--	--	--
50	11.267	7.85	7.417	11.91	7.038	12.55	7.059	12.51	6.79	13.01
100	13.031	6.79	7.69	11.49	7.85	11.25	7.723	11.44	7.622	11.59
150	13.283	6.66	7.795	11.33	8.083	10.93	8.059	10.96	7.718	11.44
200	14.197	6.23	7.893	11.19	8.187	10.79	8.269	10.68	7.899	11.18
250	--	--	8.023	11.01	8.29	10.66	8.263	10.69	8.072	10.94
300	--	--	8.11	10.89	8.257	10.70	8.458	10.44	8.237	10.72

3.4.2 In-situ SEM measurement of membranes thickness with relative humidity:

In-situ FESEM means that we can do experiments inside the SEM while observing the morphological changes for the sample, such as increasing the relative humidity inside the SEM chamber by introducing water molecules. The experimental method was mentioned earlier in the characterization section of this thesis under SEM characterization. The focus parameter was under fixed conditions as the point or line of measurement on the cross-section of each studied membrane, as shown in the ESEM figures below under different relative humidity. These steps were performed to ensure accurate measurements for the changes in in-situ thickness of the cross-sectional membranes of this study,

The ESEM images in (Figure 3-14) are for the MXene and intercalated MXene membranes under relative humidity of 40% and 90%. The graph in (Figure 3-15) shows the change in membrane thickness in relation to the changes in relative humidity. The same measuring process was utilized for GO membrane as shown in (Figure 3-16). The values of these measurements can be seen in (Table 3-7).

The most common observation for all of these membranes is an increase in thickness when increasing the relative humidity. This increase in thickness can be attributed to the intercalation of water molecules that was introduced by the rise in relative humidity[54,65,84,85].

In calculating the percentage of increase in thickness between 30% and 90% RH of MXene and GO membranes, it was found that MXene had an increase of 10.67%, which is lower than GO membrane with 12.71%. This result means that MXene is more stable than GO under the rise in relative humidity.

Observing (Figure 3-14. a, b) and (Figure 3-16. a, b), it is clear the increase in thickness is in direct relation with the relative humidity for MXene and GO membranes alike. Moreover, the specific percentage of increase in thickness for both membranes is on trend with other studies. For example, the increase in thickness for GO membrane between 30% RH and 90% RH of this study is 12.61%, where other studies have shown 18% and 14.9% on the same range of RH[84,86]. Obviously, there are some differences in percentages, which include different GO flake size used in various studies, function groups, and the multilayer structure differences. Nevertheless, the similarity between our results and other studies indicates the reliability of our ESEM experiment setup.

Changes in the thickness percentage of membranes in (Figure 3-14) were 9.82 %, 13.66%, 8.65%, and 4.12% for $Ti_3C_2T_x$, Na- $Ti_3C_2T_x$, Ca- $Ti_3C_2T_x$, and Al- $Ti_3C_2T_x$ membranes, respectively between 40%RH and 90%RH. Furthermore, sodium intercalated MXene membranes had the highest increase in thickness followed by lithium intercalated MXene, calcium, and finally aluminum intercalated MXene membranes. Upon comparing these results with hydration enthalpies for the cations used in this study (Table 3-6), it was apparent that the variation in thickness is directly related to the hydration enthalpies of the used cations. Other studies have shown that when single-charged cations like Na^+ can intercalate between the interlayer of MXene sheets, there is an increase in the interlayer spacing, which allows the water molecules to intercalate easier between the sheets and free voids existing between the MXene membranes. On the other hand, the higher-charged cations, such as Ca^{2+} and Al^{3+} can have a higher electrostatic force with the negatively charged MXene sheets when intercalating between the MXene membranes due to their high charges. This results in a higher compression

rate leaving less space for water molecules to intercalate while increasing the relative humidity. These observations suggest that monovalent cations intercalated MXenes can be utilized in applications like sensors, while multivalent cations can be used in applications like water desalination membranes [87].

Table 3-6: Hydration enthalpies for all the used cations in this study ref [82].

Cation	**Hydration enthalpy $-H°_{hyd}$ (kJ/mol)**
Li^{+}	519
Na^{+}	409
Ca^{2+}	1577
Al^{3+}	4665

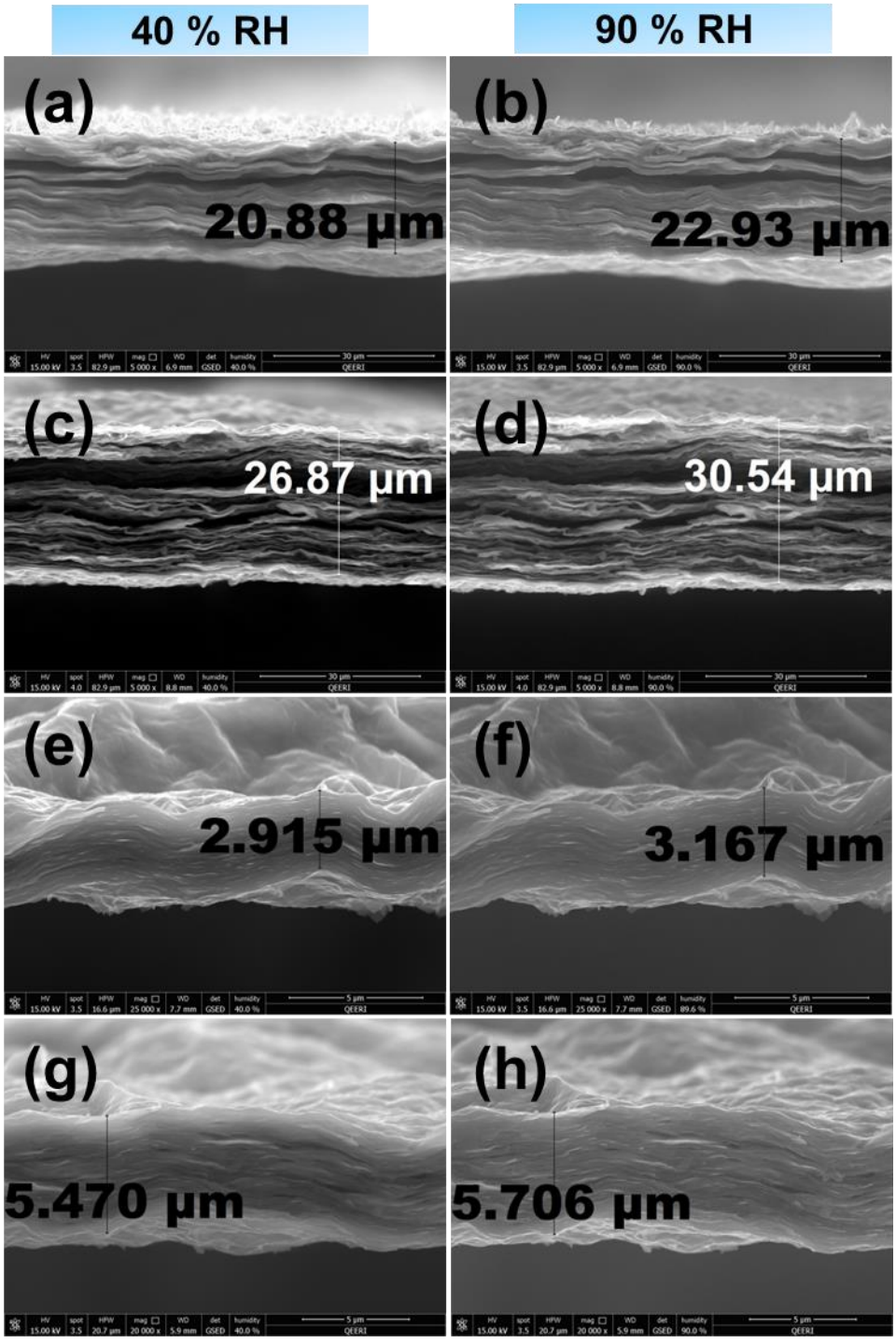
40 % RH
90 % RH
(a)
20.88 µm
(b)
22.93 µm
(c)
26.87 µm
(d)
30.54 µm
(e)
2.915 µm
(f)
3.167 µm
(g)
5.470 µm
(h)
5.706 µm

Figure 3-14: In-situ ESEM for all the MXene membranes of this study under relative humidity of 40% (left panel) to 90% RH (right panel). The thickness values are shown for (a,b) MXene, (c,d) Na-MXene, (e,f) Ca-MXene, and c,d) Al-MXene cross section membranes.

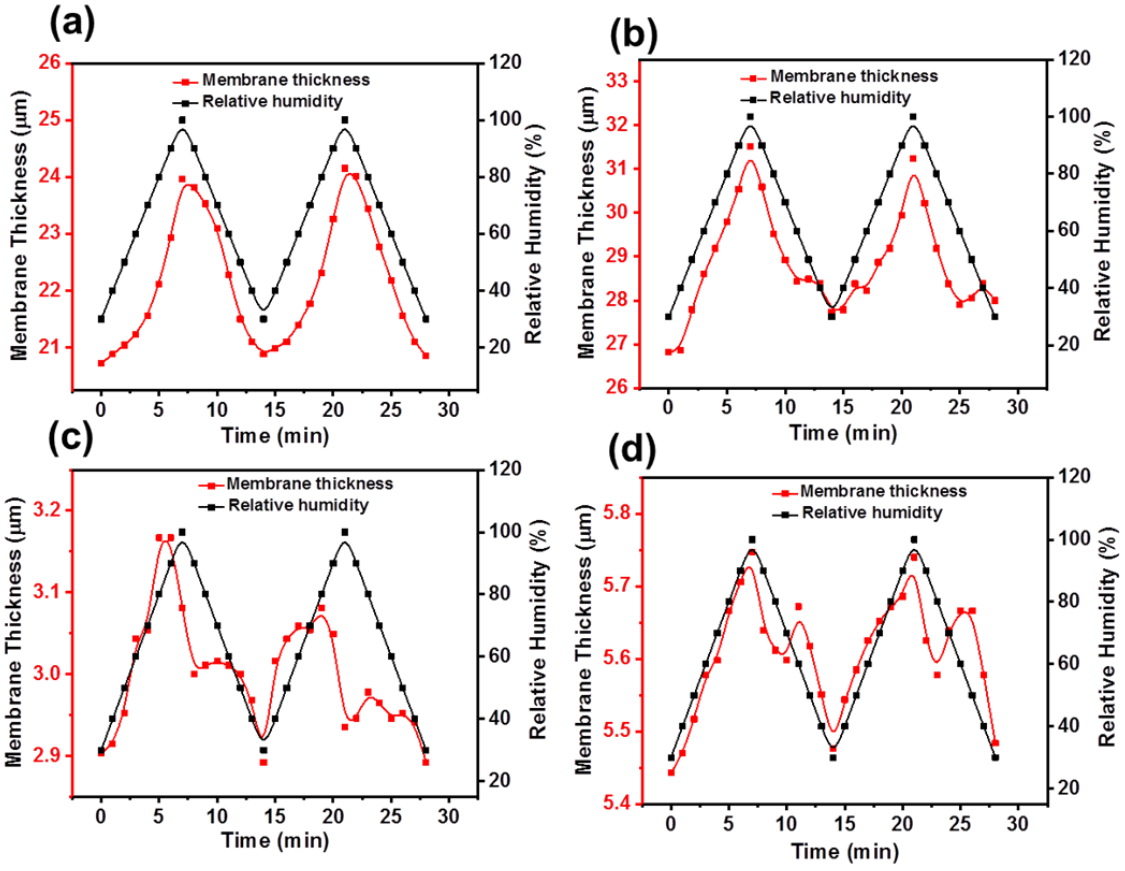

Figure 3-15: The multi-y axis graph shows the membrane thickness variation values under two cycles of relative humidites that starts from 30% and up to 100% for a) MXene, b)Na- $Ti_3C_2T_x$, and c) Ca- $Ti_3C_2T_x$, and d) Al- $Ti_3C_2T_x$.

Table 3-7: *in-situ* ESEM of RH experiment values for all the used membrane on this study between 30% and 90% RH.

	Membrane cross-section thickness (µm)				
	$Ti_3C_2T_x$	**Na-$Ti_3C_2T_x$**	**Al-$Ti_3C_2T_x$**	**Ca-$Ti_3C_2T_x$**	**GO**
40% RH	20.88	26.87	5.47	2.915	11.82
90% RH	22.93	30.54	5.706	3.167	13.3
Increased Percentage	9.82%	13.66%	4.31%	8.64%	12.52%

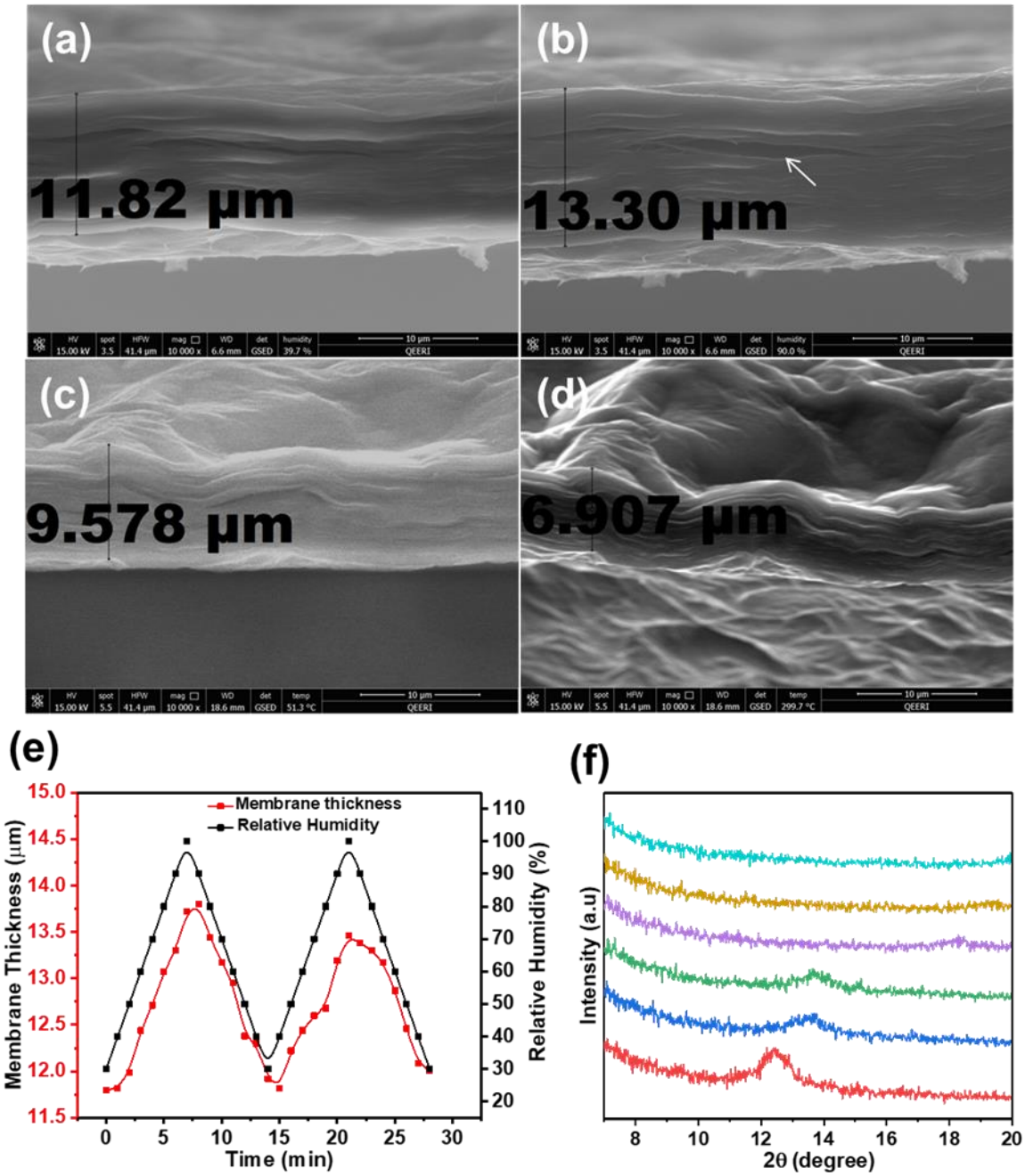

Figure 3-16: The top panel shows the relative humidity effect on the thickness of the graphene oxide cross-section membrane from a) 40% to b) 90% and the effect of in-situ ESEM heating in the bottom panel from c) 30°C to d) 300°C. e) The graph shows the variation of membrane thickness in response to relative humidity of two cycles for GO

membrane. F) the figure shows the in-situ XRD experiment and the effect of temperature from 50°C to 300°C with 50°C increment on the GO membrane.

3.4.3 In-situ SEM measurement of membranes thickness with temperature changes:

A comprehensive study of the thickness variation of the membranes in this thesis requires observing the changes in thickness under higher temperatures. For this reason, an *in-situ* high-temperature ESEM study was performed. The same conditions of accurate measurements used in the *in-situ* RH experiment were applied for high-temperature *in-situ* ESEM experiment. The temperature ranges were from 50 °C to 300 °C with 50 °C step size, while 60 seconds pauses were given for each step to allow the membrane thickness to stabilize. An interesting observation for MXene and GO membranes when high temperatures were applied, is that MXene membrane showed a change from 17.10 µm and 14.35 µm at 50°C, and 300°C, respectively (Figure 3-17.a,b). The GO membrane, on the other hand, showed 9.57 µm and 6.907 µm at the same temperature (Figure 3-16.c,d). These results show that GO membrane had shrunk 27.89% from its original thickness, while MXene only shrunk about 16.08% from its original thickness value. These results suggest that MXene is more stable at high temperatures than GO, which was reinforced by the *in-situ* XRD experiment in this study.

When comparing the results of both *in-situ* ESEM temperature and *in-situ* XRD of this study, a common link was observed when Al- $Ti_3C_2T_x$ membrane had a cross-sectional thickness shrinkage percentage between 50 °C and 300 °C with a value of 17.35%, which is the highest among its counterparts. This was also observed in the *in-situ* XRD as well. It can also be seen in (Figure 3-14) that Ca- $Ti_3C_2T_x$ and Na- $Ti_3C_2T_x$ had a shrinkage percentage of 7.07% and 4.13%, respectively, which is also in agreement with the in-situ XRD experiment in this study, where the d-space of calcium intercalated MXene

membrane had a higher decrease when compared with sodium intercalated MXene membrane. However, lithium intercalated MXene membrane had a higher shrinkage percentage when compared with sodium intercalated membrane despite the *in-situ* XRD experiment showing a smaller decrease in d-space value for Li - $Ti_3C_2T_x$ membranes than that of Na- $Ti_3C_2T_x$ membranes. This observation could be related to variations in the surrounding environment between *in-situ* XRD and *in-situ* ESEM, where the first was done under one atmospheric pressure and the latter under lower pressure with a value of ~200 Pa. The difference in pressure may affect the water release from between the membranes.

Table 3-8 provides the measured values for these membranes.

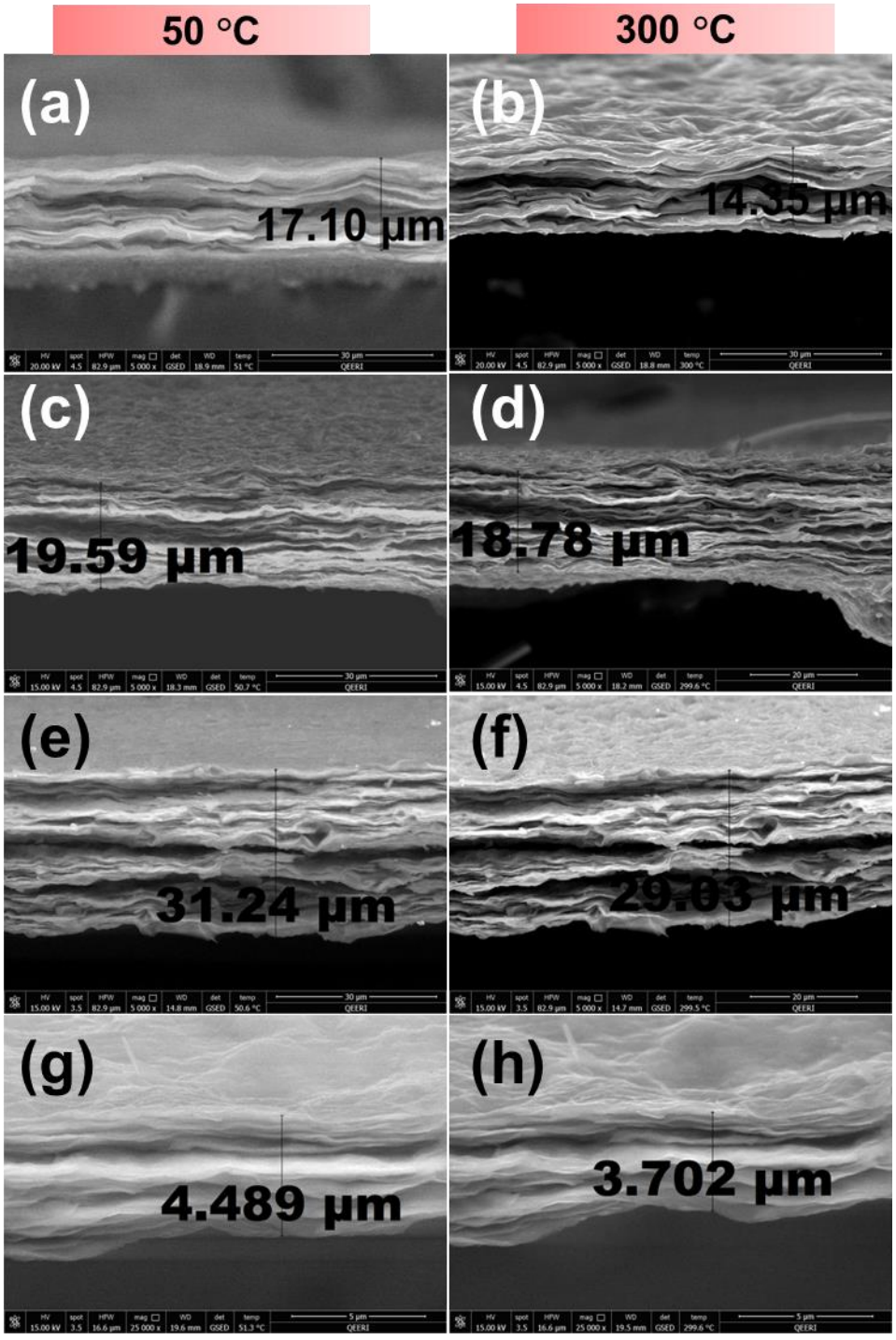

Figure 3-17: *In-situ* SEM for different intercalated MXene membranes under temperatures from 50 till 300 °C. The thickness decrease values are 16.9%, 17.53%, 7.07%, and 4.13% for (a,b) MXene, (c,d) Na-MXene, (e,f) Ca-MXene, and (g,h) Al-

MXene, respectively.

Table 3-8: results table of *in-situ* ESEM temperature values for all the used membrane on this study stepwise from 50°C to 300°C.

Degree °C	**Membrane cross-section thickness (µm)**				
	$Ti_3C_2T_x$	**Na-$Ti_3C_2T_x$**	**Ca-$Ti_3C_2T_x$**	**Al-$Ti_3C_2T_x$**	**GO**
50	17.10	19.59	31.24	4.489	9.578
100	16.19	18.94	30.59	4.392	9.011
150	15.54	18.67	29.89	4.176	8.849
200	14.57	18.46	29.41	3.874	7.716
250	14.19	18.35	29.14	3.82	7.015
300	14.35	18.78	29.03	3.702	6.907
Loss percentage	16.90%	4.13%	7.07%	17.53%	27.89%

Chapter 4 : Conclusion

The 2D conductive material of MXene was successfully synthesized by the etching of the MAX phase in a solution form before being fabricated as MXene membrane by means of the VAF process. Sodium, calcium, and aluminum cations were intercalated between MXene layers to fabricate a free-standing intercalated MXene membrane. These results were validated by powder X-ray diffraction (XRD), conventional scanning electron microscope (SEM), energy dispersive system (EDS), X-ray photoelectron spectroscopy (XPS), contact angle, and transmission electron microscope (TEM).

The hydration radius of the intercalated cations has an effect on the hydrophilicity of the membrane as larger hydrated size cations would decrease the hydrophilicity of the membrane, as shown in the contact angle.

MXene membrane showed higher stability than its counterpart GO membranes under high temperatures. This phenomenon was observed in our *in-situ* XRD experiment when the GO membrane d-space collapsed upon increasing the temperatures, unlike the MXene membrane. Similarly, MXene membrane cross section suffered less changes compared to GO membrane.

Changes in cross-section thickness of membranes is in direct relation with relative humidity variation as per *in-situ* SEM observation. MXene membrane showed fewer changes in cross-section thickness compared to the GO membrane, further validating the higher stability of the MXene membrane under different relative humidity values.

Mono-valence cations can increase the homogeneity of MXene membranes compared to

multi-valence cations, as shown in the in-situ XRD and ESEM investigations. Moreover, trivalent cations intercalated membranes collapse easier under high temperatures than lower valence ones, which could make such membranes interesting for temperature sensor applications. Furthermore, the crystallinity of all membranes in this study reduced significantly with temperature increases due to the heterogeneous loss of intercalated water.

Monovalent intercalated cation between MXene layers with low hydration enthalpy is substantially more sensitive to relative humidity than other multi-valent and higher enthalpy intercalated cations as shown in our *in-situ* SEM study, making them attractive in applications like humidity sensors.

Chapter 5 Appendix

Safety:

This project includes some safety concerns as it requires handling acidic and corrosive reagents, such as hydrochloric acids and hydrofluoric acids. The safe handling of such reagents is of extreme importance; here are some guidelines:

1. Lab safety training is a must prior to any work. This training will include general safety in case of fire and other safety-related concerns.
2. Hcl and HF-containing solutions must be dealt with inside the chemical fume hood at all times.
3. These reagents must be stored in their assigned storage (acid cabinet).
4. Always dispose of these reagents in a proper waste disposal container.
5. Personal protective equipment (PPE) such as special gloves and masks are mandatory when working inside the lab.
6. Do not work alone in the lab as a second person can help you in case of an emergency.
7. In case of skin contact of such reagents, seek help immediately from the nearest person and wash the affected area immediately under running water or under the safety shower for at least 5 minutes. Remove all contaminated clothing while flushing.
8. In case of eye contact of such reagents, wash with copious amounts of water for a minimum of 15 minutes.

9. Contact QF-QEERI safety as soon as possible in case of an emergency so you can get professional help.

In-situ ESEM images for the fabricated membranes under different relative humidity:

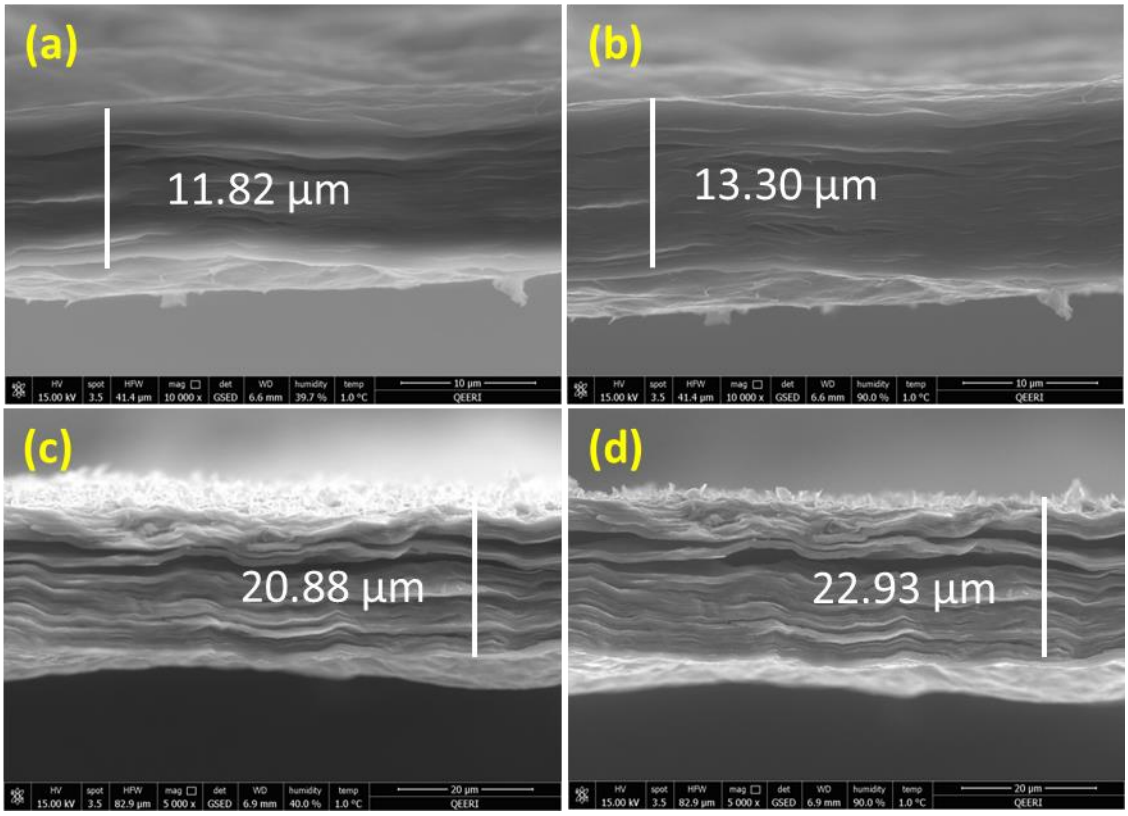

Figure 5-1: Relative humidity increase of GO cross-section from a) 40% to b) 90% and MXene from c) 40%, d) 100% RH in an in-situ SEM experiment.

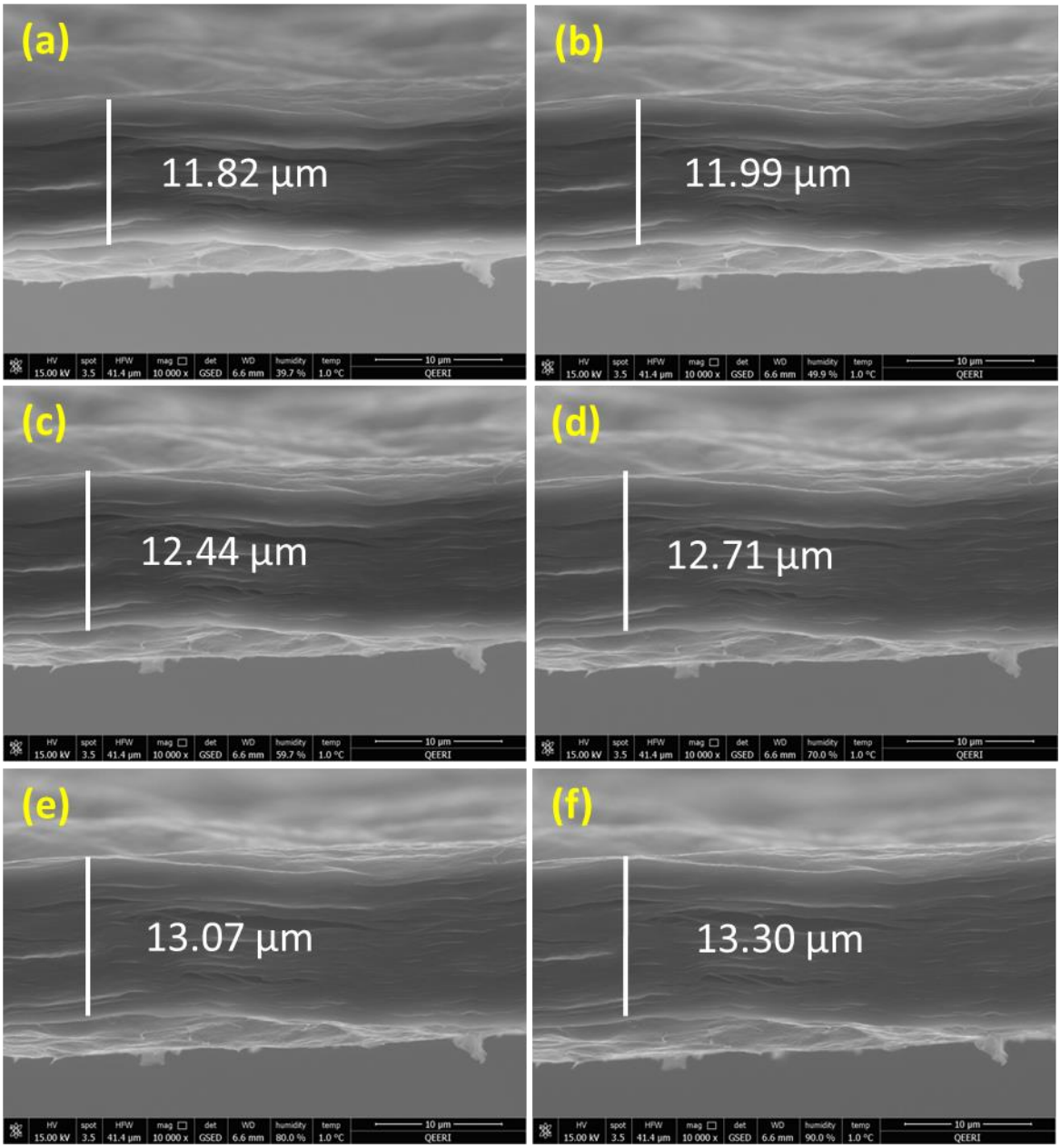

Figure 5-2: Relative humidity increase of GO membrane cross-section from a)40, b)50, c)60, d)70, e)80, and f)90 % RH in an in-situ SEM experiment.

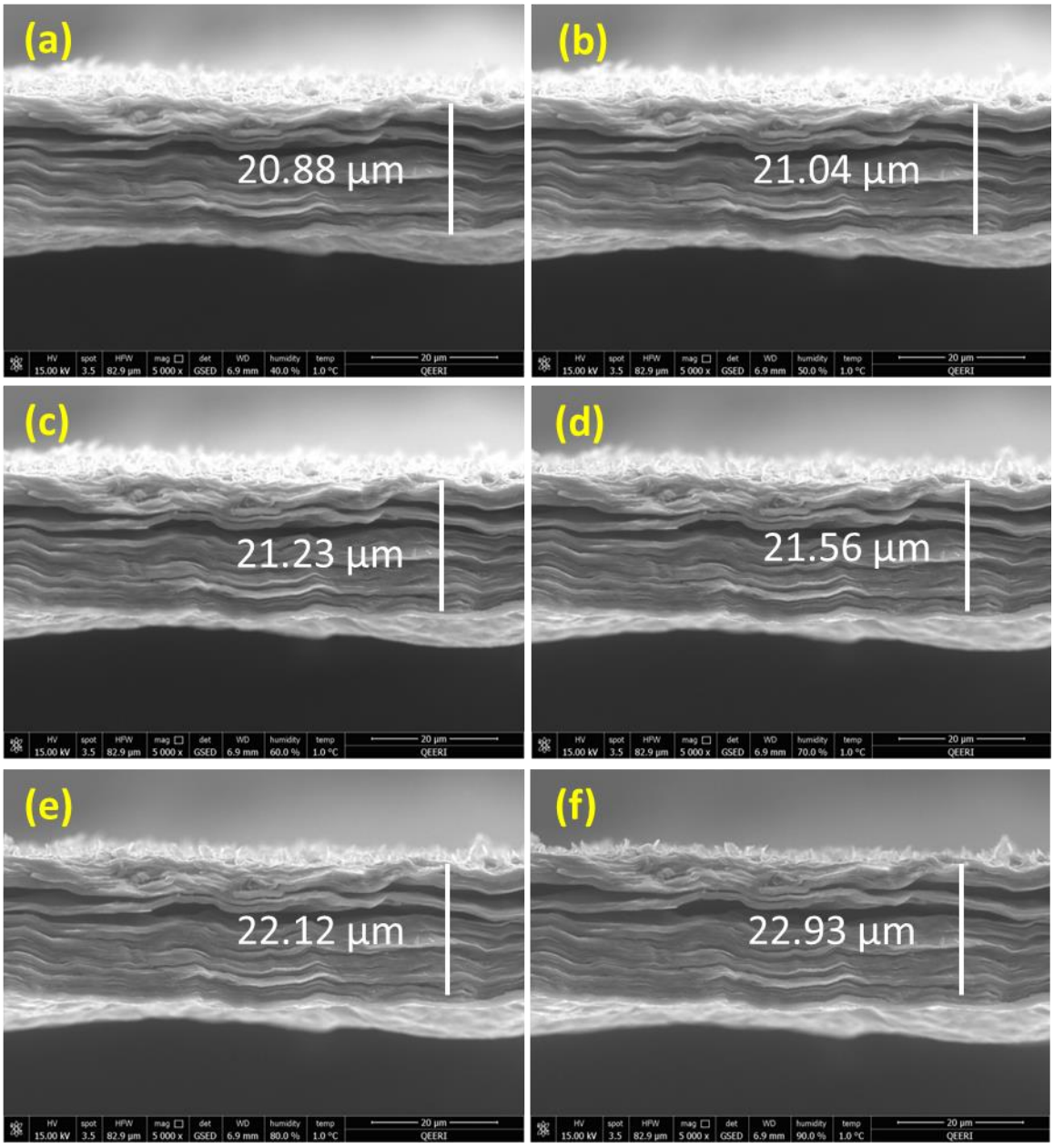

Figure 5-3: Relative humidity increase of MXene membrane cross-section from a)40, b)50, c)60, d)70, e)80, and f)90 % RH in an in-situ SEM experiment.

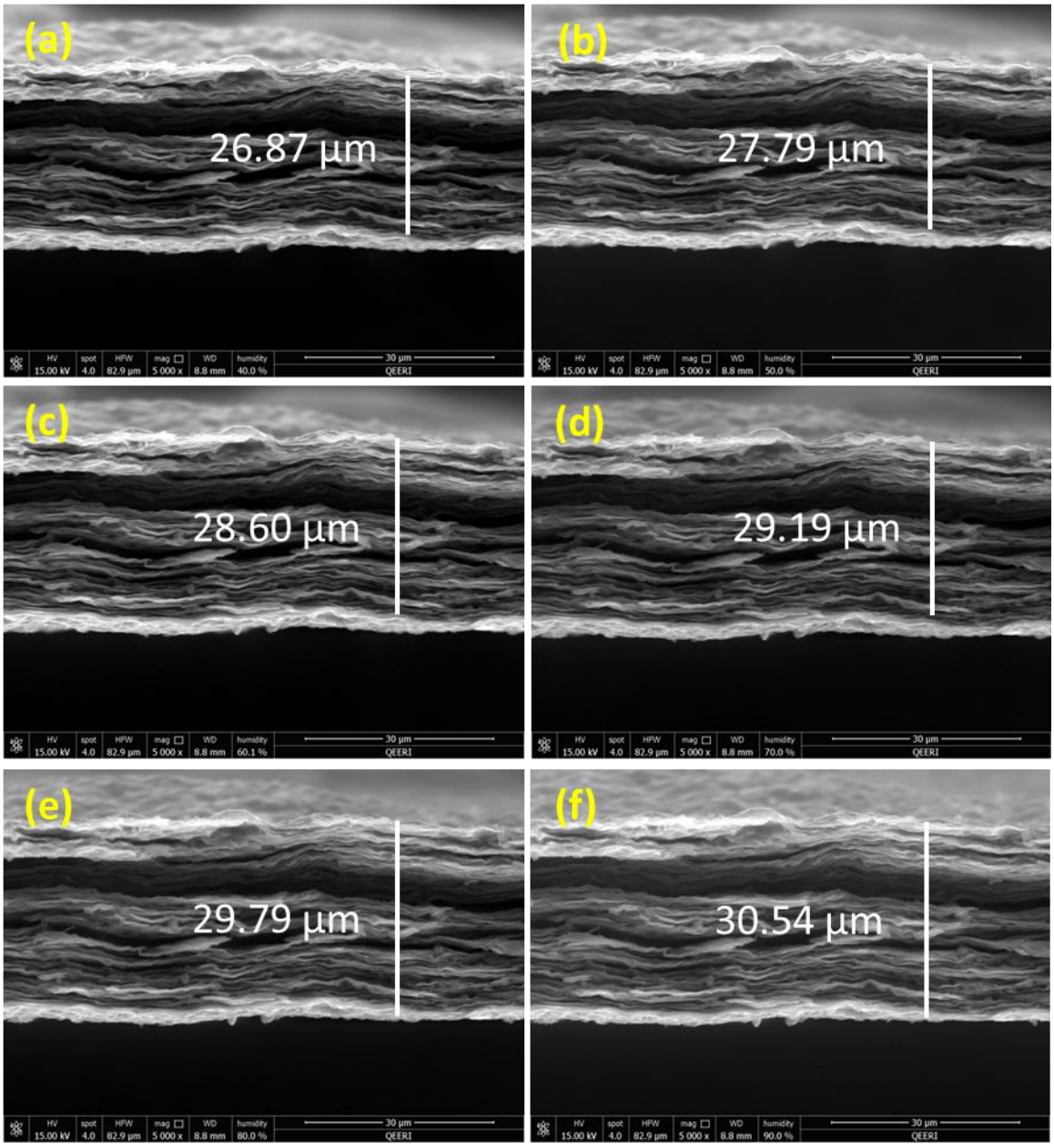

Figure 5-4: Relative humidity increase of Na-MXene membrane cross-section from a)40, b)50, c)60, d)70, e)80, and f)90 % RH in an in-situ SEM experiment.

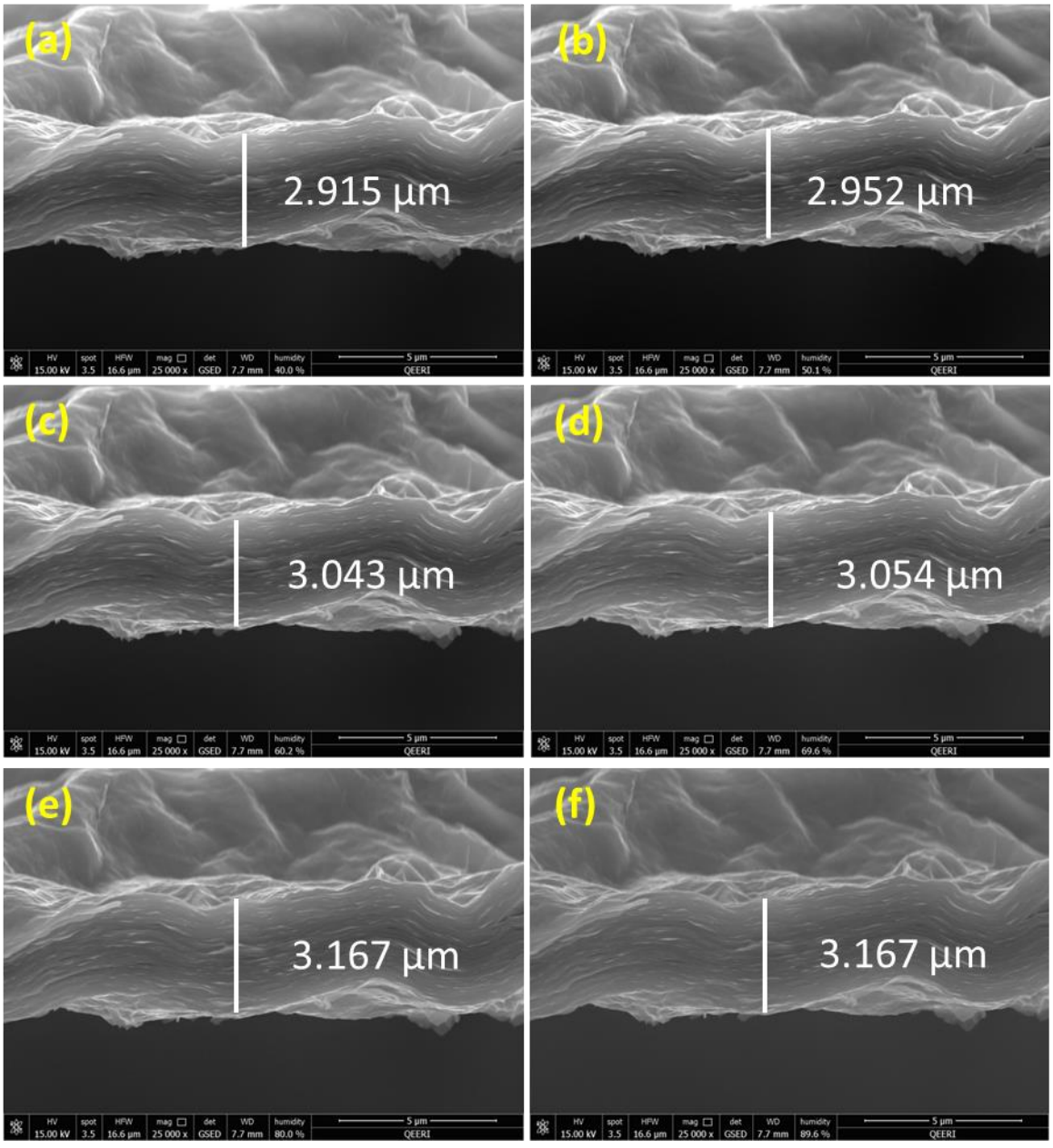

Figure 5-5: Relative humidity increase of Ca-MXene membrane cross-section from a)40, b)50, c)60, d)70, e)80, and f)90 % RH in an in-situ SEM experiment.

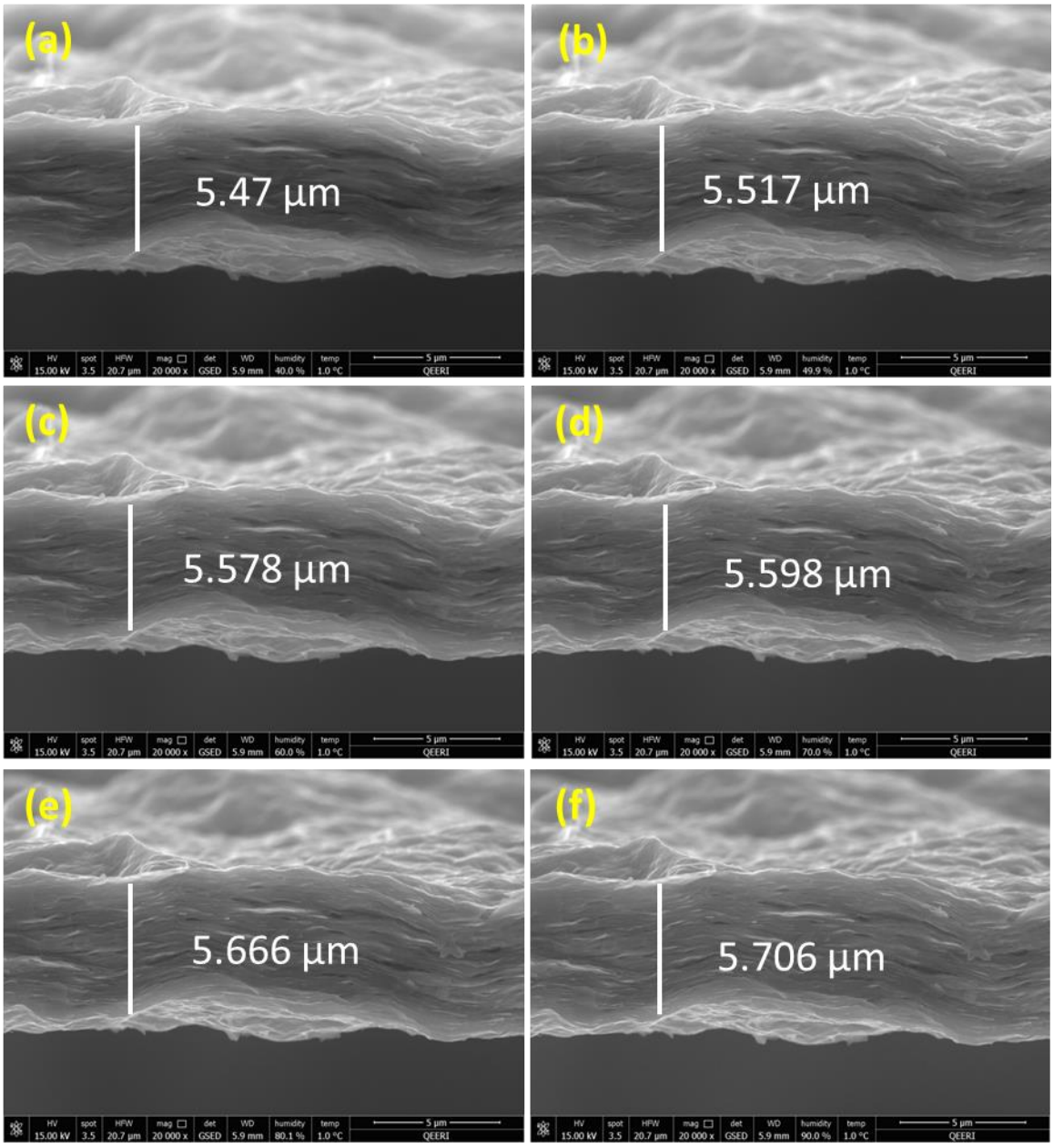

Figure 5-6: Relative humidity increase of Al-MXene membrane cross-section from a)40, b)50, c)60, d)70, e)80, and f)90 % RH in an in-situ SEM experiment.

Chapter 6 Reference:

1. Hoekstra AY, Mekonnen MM, Chapagain AK, Mathews RE, Richter BD. Global monthly water scarcity: Blue water footprints versus blue water availability. *PLoS One*. 2012;7(2). doi:10.1371/journal.pone.0032688
2. Elimelech M, Phillip WA. The Future of Seawater Desalination: Energy, Technology, and the Environment. *Science (80-)*. 2011;333(6043):712-717. doi:10.1126/science.1200488
3. Gehrke I, Geiser A, Somborn-Schulz A. Innovations in nanotechnology for water treatment. *Nanotechnol Sci Appl*. 2015;8:1. doi:10.2147/NSA.S43773
4. Subramani A, Jacangelo JG. Emerging desalination technologies for water treatment: A critical review. *Water Res*. 2015;75:164-187. doi:https://doi.org/10.1016/j.watres.2015.02.032
5. Pendergast MM, Hoek EMV. A review of water treatment membrane nanotechnologies. *Energy Environ Sci*. 2011;4(6):1946. doi:10.1039/c0ee00541j
6. Li R, Zhang L, Wang P. Rational design of nanomaterials for water treatment. *Nanoscale*. 2015;7(41):17167-17194. doi:10.1039/c5nr04870b
7. Peñate B, García-Rodríguez L. Current trends and future prospects in the design of seawater reverse osmosis desalination technology. *Desalination*. 2012;284:1-8. doi:https://doi.org/10.1016/j.desal.2011.09.010
8. Chong TH, Loo S-L, Krantz WB. Energy-efficient reverse osmosis desalination process. *J Memb Sci*. 2015;473:177-188. doi:https://doi.org/10.1016/j.memsci.2014.09.005
9. Stover RL. High recovery, low fouling, and low energy reverse osmosis. *Desalin Water Treat*. 2016;57(55):26501-26506. doi:10.1080/19443994.2016.1168586
10. Ghaffour N, Missimer TM, Amy GL. Technical review and evaluation of the economics of

water desalination: Current and future challenges for better water supply sustainability. *Desalination*. 2013;309:197-207. doi:https://doi.org/10.1016/j.desal.2012.10.015

11. Tul Muntha S, Kausar A, Siddiq M. Advances in Polymeric Nanofiltration Membrane: A Review. *Polym Plast Technol Eng*. 2017;56(8):841-856. doi:10.1080/03602559.2016.1233562

12. Mohammad AW, Teow YH, Ang WL, Chung YT, Oatley-Radcliffe DL, Hilal N. Nanofiltration membranes review: Recent advances and future prospects. *Desalination*. 2015;356:226-254. doi:https://doi.org/10.1016/j.desal.2014.10.043

13. Greenlee LF, Lawler DF, Freeman BD, Marrot B, Moulin P. Reverse osmosis desalination: Water sources, technology, and today's challenges. *Water Res*. 2009;43(9):2317-2348. doi:10.1016/j.watres.2009.03.010

14. Radcliff R, Zarnadze A. Application of Membrane Technology to the Production of Drinking Water. *Water Cond Purif Int*. 2004:23-25. http://wcponline.com/2004/08/14/application-membrane-technology-production-drinking-water/. Accessed February 1, 2020.

15. Ghidiu M, Lukatskaya MR, Zhao MQ, Gogotsi Y, Barsoum MW. Conductive two-dimensional titanium carbide "clay" with high volumetric capacitance. *Nature*. 2015;516(7529):78-81. doi:10.1038/nature13970

16. Naguib M, Mochalin VN, Barsoum MW, Gogotsi Y. 25th anniversary article: MXenes: A new family of two-dimensional materials. *Adv Mater*. 2014;26(7):992-1005. doi:10.1002/adma.201304138

17. Rezania B, Severin N, Talyzin A V., Rabe JP. Hydration of bilayered graphene oxide. *Nano Lett*. 2014;14(7):3993-3998. doi:10.1021/nl5013689

18. Rao CNR, Gopalakrishnan K, Maitra U. Comparative study of potential applications of graphene, MoS<inf>2</inf>, and other two-dimensional materials in energy devices, sensors, and related areas. *ACS Appl Mater Interfaces*. 2015;7(15):7809-7832. doi:10.1021/am509096x

19. Ghidiu M, Halim J, Kota S, Bish D, Gogotsi Y, Barsoum MW. Ion-Exchange and Cation Solvation Reactions in Ti3C2 MXene. *Chem Mater*. 2016;28(10):3507-3514. doi:10.1021/acs.chemmater.6b01275

20. Buchsteiner A, Lerf A, Pieper J. Water dynamics in graphite oxide investigated with neutron scattering. *J Phys Chem B*. 2006;110(45):22328-22338. doi:10.1021/jp0641132

21. Sun P, Zheng F, Zhu M, et al. Selective trans-membrane transport of alkali and alkaline earth cations through graphene oxide membranes based on cation-π interactions. *ACS Nano*. 2014;8(1):850-859. doi:10.1021/nn4055682

22. Sun P, Zhu M, Wang K, et al. Selective ion penetration of graphene oxide membranes. *ACS Nano*. 2013;7(1):428-437. doi:10.1021/nn304471w

23. Huang H, Ying Y, Peng X. Graphene oxide nanosheet: An emerging star material for novel separation membranes. *J Mater Chem A*. 2014;2(34):13772-13782. doi:10.1039/c4ta02359e

24. Cohen-Tanugi D, Grossman JC. Nanoporous graphene as a reverse osmosis membrane: Recent insights from theory and simulation. *Desalination*. 2015;366:59-70. doi:10.1016/j.desal.2014.12.046

25. Joshi RK, Carbone P, Wang FC, et al. Precise and Ultrafast Molecular Sieving Through Graphene Oxide Membranes. *Science (80-)*. 2014;343(6172):752-754. doi:10.1126/science.1245711

26. Alhabeb M, Maleski K, Anasori B, et al. Guidelines for Synthesis and Processing of Two-Dimensional Titanium Carbide (Ti 3 C 2 T x MXene). *Chem Mater*. 2017;29(18):7633-7644. doi:10.1021/acs.chemmater.7b02847

27. Heremans JP, Dresselhaus MS. *Nanomaterials Handbook*. (Gogotsi Y, ed.). CRC Press; 2006. doi:10.1201/9781420004014

28. Anasori B, Lukatskaya MR, Gogotsi Y. 2D metal carbides and nitrides (MXenes) for energy storage. *Nat Rev Mater*. 2017;2:16098. https://doi.org/10.1038/natrevmats.2016.98.

29. Seh ZW, Fredrickson KD, Anasori B, et al. Two-Dimensional Molybdenum Carbide (MXene) as an Efficient Electrocatalyst for Hydrogen Evolution. *ACS Energy Lett*. 2016;1(3):589-594. doi:10.1021/acsenergylett.6b00247

30. Guo J, Peng Q, Fu H, Zou G, Zhang Q. Heavy-Metal Adsorption Behavior of Two-Dimensional Alkalization-Intercalated MXene by First-Principles Calculations. *J Phys Chem C*. 2015;119(36):20923-20930. doi:10.1021/acs.jpcc.5b05426

31. Zhang Q, Liu R, Guo J, et al. Unique Lead Adsorption Behavior of Activated Hydroxyl Group in Two-Dimensional Titanium Carbide. *J Am Chem Soc*. 2014;136(11):4113-4116. doi:10.1021/ja500506k

32. Maleski K, Mochalin VN, Gogotsi Y. Dispersions of Two-Dimensional Titanium Carbide MXene in Organic Solvents. *Chem Mater*. 2017;29(4):1632-1640. doi:10.1021/acs.chemmater.6b04830

33. Naguib M, Kurtoglu M, Presser V, et al. Two-dimensional nanocrystals produced by exfoliation of Ti 3AlC 2. *Adv Mater*. 2011;23(37):4248-4253. doi:10.1002/adma.201102306

34. Mashtalir O, Naguib M, Mochalin VN, et al. Intercalation and delamination of layered

carbides and carbonitrides. *Nat Commun*. 2013;4:1-7. doi:10.1038/ncomms2664

35. Yang S, Zhang P, Wang F, et al. Fluoride-Free Synthesis of Two-Dimensional Titanium Carbide (MXene) Using A Binary Aqueous System. *Angew Chemie Int Ed*. 2018;57(47):15491-15495. doi:10.1002/anie.201809662

36. Feng A, Yu Y, Wang Y, et al. Two-dimensional MXene Ti3C2 produced by exfoliation of Ti3AlC2. *Mater Des*. 2017;114:161-166. doi:10.1016/j.matdes.2016.10.053

37. Halim J, Lukatskaya MR, Cook KM, et al. Transparent Conductive Two-Dimensional Titanium Carbide Epitaxial Thin Films. *Chem Mater*. 2014;26(7):2374-2381. doi:10.1021/cm500641a

38. Pandey RP, Rasool K, Abdul Rasheed P, Mahmoud KA. Reductive Sequestration of Toxic Bromate from Drinking Water using Lamellar Two-Dimensional Ti 3 C 2 T X (MXene). *ACS Sustain Chem Eng*. 2018;6(6):7910-7917. doi:10.1021/acssuschemeng.8b01147

39. Ghidiu M, Kota S, Halim J, et al. Alkylammonium Cation Intercalation into Ti3C2 (MXene): Effects on Properties and Ion-Exchange Capacity Estimation. *Chem Mater*. 2017;29(3):1099-1106. doi:10.1021/acs.chemmater.6b04234

40. Ma R, Sasaki T. Two-Dimensional Oxide and Hydroxide Nanosheets: Controllable High-Quality Exfoliation, Molecular Assembly, and Exploration of Functionality. *Acc Chem Res*. 2015;48(1):136-143. doi:10.1021/ar500311w

41. Ding L, Wei Y, Wang Y, Chen H, Caro J, Wang H. A Two-Dimensional Lamellar Membrane: MXene Nanosheet Stacks. *Angew Chemie Int Ed*. 2017;56(7):1825-1829. doi:10.1002/anie.201609306

42. Wang H, Wu Y, Zhang J, et al. Enhancement of the electrical properties of MXene Ti3C2 nanosheets by post-treatments of alkalization and calcination. *Mater Lett*. 2015;160:537-

540. doi:10.1016/j.matlet.2015.08.046

43. Naguib M, Mashtalir O, Carle J, et al. Two-Dimensional Transition Metal Carbides. *ACS Nano*. 2012;6(2):1322-1331. doi:10.1021/nn204153h

44. Dillon AD, Ghidiu MJ, Krick AL, et al. Highly Conductive Optical Quality Solution-Processed Films of 2D Titanium Carbide. *Adv Funct Mater*. 2016;26(23):4162-4168. doi:10.1002/adfm.201600357

45. Ying G, Dillon AD, Fafarman AT, Barsoum MW. Transparent, conductive solution processed spincast 2D Ti2CTx (MXene) films. *Mater Res Lett*. 2017;5(6):391-398. doi:10.1080/21663831.2017.1296043

46. Mariano M, Mashtalir O, Antonio FQ, et al. Solution-processed titanium carbide MXene films examined as highly transparent conductors. *Nanoscale*. 2016;8(36):16371-16378. doi:10.1039/c6nr03682a

47. Hantanasirisakul K, Zhao MQ, Urbankowski P, et al. Fabrication of Ti3C2Tx MXene Transparent Thin Films with Tunable Optoelectronic Properties. *Adv Electron Mater*. 2016;2(6):1-7. doi:10.1002/aelm.201600050

48. Peng YY, Akuzum B, Kurra N, et al. All-MXene (2D titanium carbide) solid-state microsupercapacitors for on-chip energy storage. *Energy Environ Sci*. 2016;9(9):2847-2854. doi:10.1039/c6ee01717g

49. Gogotsi Y, Barsoum MW, Zhao M-Q, Ghidiu M, Lukatskaya MR. Conductive two-dimensional titanium carbide 'clay' with high volumetric capacitance. *Nature*. 2014:1-9. doi:10.1038/nature13970

50. Kurra N, Ahmed B, Gogotsi Y, Alshareef HN. MXene-on-Paper Coplanar Microsupercapacitors. *Adv Energy Mater*. 2016;6(24):1-8. doi:10.1002/aenm.201601372

51. Shahzad F, Alhabeb M, Hatter CB, et al. Electromagnetic interference shielding with 2D transition metal carbides (MXenes). *Science (80-)*. 2016;353(6304):1137-1140. doi:10.1126/science.aag2421

52. Ling Z, Ren CE, Zhao MQ, et al. Flexible and conductive MXene films and nanocomposites with high capacitance. *Proc Natl Acad Sci U S A*. 2014;111(47):16676-16681. doi:10.1073/pnas.1414215111

53. Ren CE, Hatzell KB, Alhabeb M, Ling Z, Mahmoud KA, Gogotsi Y. Charge- and Size-Selective Ion Sieving Through Ti3C2Tx. *J Phys Chem Lett*. 2015;6:4026-4031. doi:10.1021/acs.jpclett.5b01895

54. Osti NC, Naguib M, Ostadhossein A, et al. Effect of Metal Ion Intercalation on the Structure of MXene and Water Dynamics on its Internal Surfaces. *ACS Appl Mater Interfaces*. 2016;8(14):8859-8863. doi:10.1021/acsami.6b01490

55. Lukatskaya MR, Dall'Agnese Y, Naguib M, et al. Cation Intercalation and High Volumetric Capacitance of Two-Dimensional Titanium Carbide. *Science (80-)*. 2013;341(6153):1502-1505. doi:10.1126/science.1241488

56. Qian Y, Wei H, Jiang Z, et al. Ti3C2Tx MXene/polyaniline (PANI) sandwich intercalation structure composites constructed for microwave absorption. *Compos Sci Technol*. 2018;169(March 2018):52-59. doi:10.1016/j.compscitech.2018.10.016

57. Shpigel N, Levi MD, Sigalov S, Mathis TS, Gogotsi Y, Aurbach D. Direct Assessment of Nanoconfined Water in 2D Ti3C2 Electrode Interspaces by a Surface Acoustic Technique. *J Am Chem Soc*. 2018;140(28):8910-8917. doi:10.1021/jacs.8b04862

58. Hart JL, Hantanasirisakul K, Lang AC, et al. Control of MXenes' electronic properties through termination and intercalation. *Nat Commun*. 2019;10(1). doi:10.1038/s41467-

018-08169-8

59. Li H, Shi W, Han W, et al. Tent-pitching-inspired high-valence period 3-cation pre-intercalation excels for anode of 2D titanium carbide (MXene) with high Li storage capacity. *Energy Storage Mater*. 2018;16:163-168. doi:10.1016/j.ensm.2018.04.029

60. Lin Z, Rozier P, Duployer B, et al. Electrochemical and in-situ X-ray diffraction studies of Ti3C2Tx MXene in ionic liquid electrolyte. *Electrochem commun*. 2016;72:50-53. doi:10.1016/j.elecom.2016.08.023

61. Pandey RP, Rasool K, Madhavan VE, Aïssa B, Gogotsi Y, Mahmoud KA. Ultrahigh-flux and fouling-resistant membranes based on layered silver/MXene (Ti<inf>3</inf>C<inf>2</inf>T<inf>:X</inf>) nanosheets. *J Mater Chem A*. 2018;6(8):3522-3533. doi:10.1039/c7ta10888e

62. Lerf A, He H, Forster M, Klinowski J. Structure of graphite oxide revisited. *J Phys Chem B*. 1998;102(23):4477-4482. doi:10.1021/jp9731821

63. Ding L, Wei Y, Li L, et al. MXene molecular sieving membranes for highly efficient gas separation. *Nat Commun*. 2018;9(1):1-7. doi:10.1038/s41467-017-02529-6

64. Collini P, Kota S, Dillon AD, Barsoum MW, Fafarman AT. Electrophoretic deposition of two-dimensional titanium carbide (MXene) thick films. *J Electrochem Soc*. 2017;164(9):D573-D580. doi:10.1149/2.0211709jes

65. Célérier S, Hurand S, Garnero C, et al. Hydration of Ti 3 C 2 T x MXene: An Interstratification Process with Major Implications on Physical Properties. *Chem Mater*. 2019;31(2):454-461. doi:10.1021/acs.chemmater.8b03976

66. Come J, Black JM, Lukatskaya MR, et al. Controlling the actuation properties of MXene paper electrodes upon cation intercalation. *Nano Energy*. 2015;17:27-35.

doi:https://doi.org/10.1016/j.nanoen.2015.07.028

67. Ghidiu M, Halim J, Kota S, Bish D, Gogotsi Y, Barsoum MW. Ion-Exchange and Cation Solvation Reactions in Ti3C2 MXene. *Chem Mater*. 2016;28(10):3507-3514. doi:10.1021/acs.chemmater.6b01275

68. Voigt CA, Ghidiu M, Natu V, Barsoum MW. Anion Adsorption, Ti3C2T z MXene Multilayers, and Their Effect on Claylike Swelling. *J Phys Chem C*. 2018;122(40):23172-23179. doi:10.1021/acs.jpcc.8b07447

69. Seredych M, Shuck CE, Pinto D, et al. High-Temperature Behavior and Surface Chemistry of Carbide MXenes Studied by Thermal Analysis. *Chem Mater*. 2019;31(9):3324-3332. doi:10.1021/acs.chemmater.9b00397

70. Kishi A, Toraya H. Simultaneous measurements of X-ray diffraction (XRD) and differential scanning calorimetry (DSC) data under controlled humidity condition: Instrumentation and application to studies on hydration, dehydration, and rehydration processes of pharmaceutical co. *Powder Diffr*. 2004;19(1):31-35. doi:10.1154/1.1649321

71. Newbury DE. Imaging deep holes in structures with gaseous secondary electron detection in the environmental scanning electron microscope. *Scanning*. 1996;18(7):474-482. doi:10.1002/sca.1996.4950180702

72. Derbyshire H, Miller ER, Turkulin H. *Investigations into the Photodegradation of Wood Using Microtensile Testing: Part 2: An Investigation of the Changes in Tensile Strength of Different Softwood Species during Natural Weathering*. Vol 54.; 1996. doi:10.1007/s001070050123

73. Danilatos GD. Beam-radiation effects on wool in the ESEM. In: *Beam-Radiation Effects on Wool in the ESEM*. San Francisco: 44th Annual Meeting of the Electron Microscopy

Society of America; 1986:674-675. https://publications.csiro.au/rpr/pub?list=BRO&pid=procite:fae4bc35-7113-40a1-af25-5005e1efebc7. Accessed December 29, 2019.

74. Lewis DB. Scanning Electron Microscopy and X-ray Microanalysis. *Trans IMF*. 1992;70(4):198-202. doi:10.1080/00202967.1992.11870972

75. Talos TEM. Thermo Fisher Scientific. https://www.fei.com/tem/talos/. Published April 17, 2018. Accessed January 27, 2020.

76. Fahlman BD. Materials Characterization. In: Fahlman BD, ed. *Materials Chemistry*. Dordrecht: Springer Netherlands; 2018:643-741. doi:10.1007/978-94-024-1255-0_7

77. Electron Spectroscopy for Surface Analysis 1. Outline Introduction XPS Background XPS Instrument How Does XPS Technology Work? Auger Electron Cylindrical. - ppt download. https://slideplayer.com/slide/9755247/. Accessed January 27, 2020.

78. Sharma G, Naguib M, Feng D, Gogotsi Y, Navrotsky A. Calorimetric Determination of Thermodynamic Stability of MAX and MXene Phases. *J Phys Chem C*. 2016. doi:10.1021/acs.jpcc.6b10241

79. Mai NT, Thuy TT, Mott DM, Maenosono S. Chemical synthesis of blue-emitting metallic zinc nano-hexagons. *CrystEngComm*. 2013;15(33):6606-6610. doi:10.1039/c3ce40801a

80. Liu J, Zhang H Bin, Sun R, et al. Hydrophobic, Flexible, and Lightweight MXene Foams for High-Performance Electromagnetic-Interference Shielding. *Adv Mater*. 2017;29(38). doi:10.1002/adma.201702367

81. Zou G, Zhang Z, Guo J, et al. Synthesis of MXene/Ag Composites for Extraordinary Long Cycle Lifetime Lithium Storage at High Rates. *ACS Appl Mater Interfaces*. 2016;8(34):22280-22286. doi:10.1021/acsami.6b08089

82. Smith DW. Ionic hydration enthalpies. *J Chem Educ*. 1977;54(9):540. doi:10.1021/ed054p540

83. Koh HJ, Kim SJ, Maleski K, et al. Enhanced Selectivity of MXene Gas Sensors through Metal Ion Intercalation: In Situ X-ray Diffraction Study. *ACS Sensors*. 2019;4(5):1365-1372. doi:10.1021/acssensors.9b00310

84. Daio T, Bayer T, Ikuta T, et al. In-Situ ESEM and EELS Observation of Water Uptake and Ice Formation in Multilayer Graphene Oxide. *Sci Rep*. 2015;5(1):1-18. doi:10.1038/srep11807

85. Lerf A, Buchsteiner A, Pieper J, et al. Hydration behavior and dynamics of water molecules in graphite oxide. *J Phys Chem Solids*. 2006;67(5-6):1106-1110. doi:10.1016/j.jpcs.2006.01.031

86. Bayer T, Bishop SR, Nishihara M, Sasaki K, Lyth SM. Characterization of a graphene oxide membrane fuel cell. *J Power Sources*. 2014;272:239-247. doi:10.1016/j.jpowsour.2014.08.071

87. Muckley ES, Naguib M, Wang HW, et al. Multimodality of Structural, Electrical, and Gravimetric Responses of Intercalated MXenes to Water. *ACS Nano*. 2017;11(11):11118-11126. doi:10.1021/acsnano.7b05264